Thermal Lattice Boltzmann Methods for the Simulation of Turbulent Flows with Conjugate Heat Transfer

Application to Refrigerated Vehicles

zur Erlangung des akademischen Grades eines

Doktors der Ingenieurwissenschaften

von der KIT-Fakultät für
Chemieingenieurwesen und Verfahrenstechnik
des Karlsruher Instituts für Technologie (KIT)

genehmigte

Dissertation

von
M. Sc. Maximilian Gaedtke
aus Düsseldorf

Tag der mündlichen Prüfung: 5. November 2020

Referent:	Prof. Dr.-Ing. Hermann Nirschl
1. Korreferentin:	Prof. Dr.-Ing. Bettina Frohnapfel
2. Korreferent:	Dr. rer. nat. Mathias J. Krause

This work is typeset with Source Serif Pro and Source Sans Pro using LaTeX.

Abstract

This thesis presents a thermal lattice Boltzmann method (TLBM) for the unsteady simulation of turbulent flows with natural convection and conjugate heat transfer. Turbulent flows with its chaotic pressure and velocity fluctuations pose a special challenge for numerical simulations, where thermal buoyancy driven turbulent flows represent a particularly difficult task. As shown in this work, TLBM enables large eddy simulations (LES) of such problems on industrial and engineering scale using a Smagorinsky sub grid scale model executed on several thousand processor cores leveraging its intrinsic parallelizability. The suitability of the present method is demonstrated in this thesis on the basis of applications to the simulation of the internal air flow and insulation efficiency of a refrigerated truck, heat transport in the air gap between the rotor and stator in electric motors, the advancement of highly efficient insulation based on vacuum insulation panels (VIP) and latent heat storage as well as their application in refrigerated trucks.

Extensive validation of the method and its implementation within the open source framework OpenLB is conducted. Second order grid convergence is demonstrated against the analytical *porous plate problem*, while stable simulations are achieved even for coarse discretization with high Reynolds and Rayleigh numbers. Very good agreement is shown for *natural convection in a square cavity*, a well-known benchmark case, from laminar to turbulent regime with $10^3 \leq \mathrm{Ra} \leq 10^{10}$ and at resolutions of $y^+ \approx 2$.

In the first part of the results, simulations of an empty cooling body for a refrigerated truck are presented. The flow field and heat transfer within a given refrigerated truck shows very good agreement with measurement results, in particular experimental data for a refrigerated vehicle at $\mathrm{Re} \approx 53\,000$ at four characteristic velocity and 13 temperature positions in the truck. The simu-

lations resolve conjugate heat transfer through the insulation walls. This now allows to precisely predict heat fluxes close to Nusselt correlations for the given setup, but – in contrast to common Nusselt correlations – the heat flux is spatially resolved in the simulation.

In the second part of the results, flow and heat transfer in an annular gap with inner rotating cylinder is investigated. The particular challenge in the simulation of this *Taylor-Couette flow* is the formation of Taylor vortices, which, due to their rotation perpendicular to the main flow direction, significantly increase the corresponding heat transfer. Detailed unsteady simulations are performed over a wide rotational speed range from almost creeping flows to the occurrence of Taylor vortices. Good agreement with the previous results for the flow structure and the improvement of heat transfer by Taylor vortices is found. In particular, the present method is compared against measurements, a correlation and simulations using the shear stress transport (SST) turbulence model. Special attention is paid to the prediction of the critical Taylor number. While direct numerical simulations (DNS) with LBM predict the critical Taylor number from the experiments almost identically, the LBM-LES slightly overestimates it and the SST model further overestimates the occurrence of Taylor vortices, which can be attributed to the overly dissipative nature of the turbulence models for the transition to turbulent flow conditions.

In the third part of the results, innovative concepts for improved, more sustainable refrigerated vehicles are numerically investigated. In order to reduce fuel consumption and related emissions, two approaches are considered promising: (a) the inclusion of vacuum insulation panels (VIP) in the walls of the refrigerated body and (b) the introduction of a latent heat storage (LHS) to exchange fuel-driven air conditioning (AC). Using the present TLBM allows the resolution of turbulent air flow induced by the AC and natural convection, the heat flux inside the insulating walls and the deep frozen cargo in the simulations. This provides new insights into the influence of the concepts on heat transfer in different refrigerated bodies. The simulations show strongly reduced and homogenized incoming heat flow for the combined PUR and VIP insulation material compared to a pure PUR insulation. The insulation of the cooled structure using VIPs therefore halves the required cooling energy. This enables to replace the AC with an LHS mounted near the roof and an additional ventilation system with markedly lower overall capacity. Taking into account the temperature homogeneity of frozen products, a slight flow around the chilled goods is considered necessary. The maximum allowable downtime of the AC is determined in the simulations to be approximately 3.3 min (PUR),

8 min (PUR+VIP) and 11 min (PUR+VIP+LHS), respectively.

In the fourth part of the results, an LBM for the simulation of melting and conjugate heat transfer based on the transport of total enthalpy is presented, which yields precise results for a validation against the analytical solution of the time-dependent *Stefan problem*. The method developed in this work shows low interfacial diffusion for a wide range of relaxation times and Stefan numbers. Furthermore, close agreement for melting of gallium including natural convection in 2D and 3D with measurements and simulations using different approaches is demonstrated. The model is further applied to the melting of paraffin in two complex metal foam geometries. Voxel-based parallel meshing is presented, which allows fast and automated preprocessing of the complex geometry in a few minutes. The simulations successfully capture multi-domain heat transfer in 3D, with the thermal conductivity of the foam being more than 1000 times greater than that of the paraffin. The shape of the melt front and the influence of the specific surface areas of the different metal foams are in close agreement with previous simulations.

Zusammenfassung

In dieser Arbeit wird eine thermische Lattice-Boltzmann-Methode (TLBM) für die instationäre Simulation turbulenter Strömungen mit natürlicher Konvektion und konjugierter Wärmeübertragung vorgestellt. Turbulente Strömungen mit ihren chaotischen Druck- und Geschwindigkeitsschwankungen stellen eine besondere Herausforderung für numerische Simulationen dar, wobei turbulente Strömungen, angetrieben durch thermische Auftriebskräfte, eine besonders schwierige Aufgabe darstellen. Wie in dieser Arbeit gezeigt wird, ermöglicht TLBM Large Eddy Simulationen (LES) solcher Probleme im industriellen und technischen Maßstab unter Verwendung eines Smagorinsky-Feinstruktur-Modells und unter Ausnutzung seiner intrinsischen Parallelisierbarkeit sowie der Möglichkeit, mehrere tausend Prozessorkerne zu verwenden. Die Eignung der vorliegenden Methode wird in dieser Arbeit anhand von Anwendungen zur Simulation der Innenluftströmung und der Isolationseffizienz eines Kühlwagens, des Wärmetransports im Luftspalt zwischen Rotor und Stator bei Elektromotoren, der Weiterentwicklung hocheffizienter Isolation auf der Basis von Vakuumisolationspaneelen (VIP) und Latentwärmespeichern sowie deren Anwendung in Kühlwagen gezeigt.

Eine umfassende Validierung der Methode und ihrer Implementierung im Open-Source-Framework OpenLB wird durchgeführt. Gitterkonvergenz zweiter Ordnung wird gegen das analytische *Porous Plate Problem* demonstriert, während stabile Simulationen auch bei grober Diskretisierung mit hohen Reynolds- und Rayleigh-Zahlen erreicht werden. Eine sehr gute Übereinstimmung wird für *natürliche Konvektion in einem quadratischen Hohlraum*, ein bekannter Benchmark-Fall, vom laminaren zum turbulenten Regime mit $10^3 \leq \mathrm{Ra} \leq 10^{10}$ und bei Auflösungen von $y^+ \approx 2$ gezeigt.

Im ersten Teil der Ergebnisse werden Simulationen eines leeren Kühlauf-

baus für einen Kühllastwagen vorgestellt. Das Strömungsfeld und der Wärmeübergang innerhalb eines gegebenen Kühllastwagens zeigt eine sehr gute Übereinstimmung mit den Messergebnissen, insbesondere den experimentellen Daten für ein Kühlfahrzeug bei $\mathrm{Re} \approx 53\,000$ an vier charakteristischen Geschwindigkeits- und 13 Temperaturpositionen im Lastwagen. Die Wärmeübertragung durch die Wände wird in den Simulationen durch konjugierte Wärmeübertragung aufgelöst. Dies ermöglicht nun die präzise Vorhersage von Wärmeströmen nahe von Nusselt-Korrelationen für den gegebenen Aufbau, aber – im Gegensatz zu gewöhnlichen Nusselt-Korrelationen – wird der Wärmestrom in der Simulation räumlich aufgelöst.

Im zweiten Teil der Ergebnisse wird die Strömung und der Wärmeübergang in einem Ringspalt mit innen rotierendem Zylinder untersucht. Die besondere Herausforderung bei der Simulation dieser *Taylor-Couette-Strömung* ist die Bildung von Taylor-Wirbeln, die durch ihre Rotation senkrecht zur Hauptströmungsrichtung den entsprechenden Wärmeübergang deutlich erhöhen. Detaillierte instationäre Simulationen werden über einen weiten Drehzahlbereich von fast schleichender Strömungen bis hin zum Auftreten von Taylor-Wirbeln durchgeführt. Es wird eine gute Übereinstimmung mit bisherigen Ergebnissen für die Strömungsstrukturen und die Verbesserung des Wärmeübergangs durch Taylor-Wirbel festgestellt. Insbesondere wird die vorliegende Methode mit Messungen, einer Korrelation und Simulationen unter Verwendung des Scherspannungstransport-Turbulenzmodells (SST) verglichen. Besonderes Augenmerk wird auf die Vorhersage der kritischen Taylor-Zahl gelegt. Während direkte numerische Simulationen (DNS) mit LBM die kritische Taylor-Zahl aus den Experimenten nahezu identisch vorhersagen, wird sie von LBM-LES leicht und vom SST-Modell weiter überschätzt, was auf die übermäßig dissipative Natur der Turbulenzmodelle für die Transition zurückzuführen ist.

Im dritten Teil der Ergebnisse werden innovative Konzepte für verbesserte, nachhaltigere Kühlfahrzeuge numerisch untersucht. Um den Kraftstoffverbrauch und die damit verbundenen Emissionen zu reduzieren, werden zwei Ansätze als vielversprechend angesehen: (a) der Einbau von Vakuum-Isolationspaneelen (VIP) in die Wände des Kühlkoffers und (b) die Einführung eines Latentwärmespeichers (LHS) zum Austausch der kraftstoffbetriebenen Klimaanlage (AC). Die Verwendung des vorliegenden TLBM erlaubt in den Simulationen die Auflösung der durch die AC und die natürliche Konvektion induzierten turbulenten Luftströmung, des Wärmeflusses innerhalb der Isolierwände und der tiefgefrorenen Ladung. Dies liefert neue Erkenntnisse über den Einfluss der Konzepte auf die Wärmeübertragung in verschiede-

nen Kühlaufbauten. Die Simulationen zeigen einen stark reduzierten und homogenisierten einströmenden Wärmestrom für das kombinierte PUR- und VIP-Isoliermaterial im Vergleich zu einer reinen PUR-Isolierung. Die Dämmung des Kühlaufbaus mit VIPs halbiert daher die erforderliche Kühlenergie. Dies ermöglicht den Ersatz der AC durch einen LHS in Dachnähe und ein zusätzliches Lüftungssystem mit deutlich geringerer Gesamtleistung. Unter Berücksichtigung der Temperaturhomogenität von Tiefkühlprodukten wird eine leichte Umströmung des Kühlgutes als notwendig erachtet. Die maximal zulässige Ausfallzeit der AC wird in den Simulationen mit jeweils ca. 3,3 min (PUR), 8 min (PUR+VIP) und 11 min (PUR+VIP+LHS) ermittelt.

Im vierten Teil der Ergebnisse wird eine LBM zur Simulation des Schmelzens und des konjugierten Wärmeübergangs auf der Basis des Transports der Gesamtenthalpie vorgestellt, welche bei Validierung gegen die analytische Lösung des zeitabhängigen *Stefan-Problems* präzise Ergebnisse liefert. Die in dieser Arbeit entwickelte Methode zeigt geringe Grenzflächendiffusion für einen weiten Bereich von Relaxationszeiten und Stefan-Zahlen. Weiterhin wird eine enge Übereinstimmung für das Schmelzen von Gallium einschließlich der natürlichen Konvektion in 2D und 3D mit Messungen und Simulationen mit unterschiedlichen Ansätzen gezeigt. Das Modell wird ferner auf das Schmelzen von Paraffin in zwei komplexen Metallschaumgeometrien angewendet. Es wird eine Voxel-basierte parallele Vernetzung vorgestellt, die eine schnelle und automatisierte Verarbeitung der komplexen Geometrie in wenigen Minuten ermöglicht. Die Simulationen erfassen erfolgreich den materialübergreifenden Wärmetransfer in 3D, wobei die Wärmeleitfähigkeit des Schaums mehr als 1000-mal größer als die des Paraffins ist. Die Form der Schmelzfront und der Einfluss der spezifischen Oberfläche der verschiedenen Metallschäume stehen in enger Übereinstimmung mit früheren Simulationen.

Contents

1 Introduction

1.1 Computational Fluid Dynamics for Turbulent Thermal Flows

The calculation speed of computers has substantially increased during the past 30 years – not only for personal computers, but also for mobile devices and especially in high-performance cluster systems, see the TOP500 Project (Meuer 2008, top500.org). Leveraging tens of thousands of processor cores in parallel enables modeling and simulation of more and more complex systems and processing huge amounts of measurement data. High-performance computing (HPC) is increasingly important, especially in scientific computing (Hager and Wellein 2010), where its applications cover almost all areas of science, technology, engineering, and mathematics (STEM) – from meteorology, climatology and astrophysics over biology, genetics and quantum chemistry to medicine and fluid mechanics (Nash 1990; Nagel et al. 2018).

One of the fields with extensive use of HPC is computational fluid dynamics (CFD), where the simulation of turbulent flows pose a particular challenge. Although turbulent flows are observed in everyday situations and in most technical applications, and despite decades of research, their chaotic variations in pressure and velocity are not entirely understood (Pope 2000). The Reynolds-averaged Navier-Stokes equations (RANS) are commonly used to describe turbulent flows in CFD, see e.g. Ferzinger and Perić (2002). A time averaging is

applied on the unsteady Navier-Stokes equations so that a statistically steady state system of equations is derived, where the features of the turbulence are no longer resolved in the simulation, but rather modeled by additional transport equations. This comes with the advantage, that coarser meshes and fast steady state solvers can be used. However, due to the variety of turbulent flows and their complex characteristics, it is not possible to derive a single RANS model with universal validity (Fröhlich 2006).

One specifically complex phenomenon is turbulent natural convection caused by thermal buoyancy forces (Launder 1988). Motion in natural convection is driven by gravity through density variations of the fluid rather than by external devices such as fans or pumps. This phenomenon is seen in all kinds of weather and wind systems, oceanic currents and a large number of engineering tasks, for instance related to passively cooling devices from computer chips to process equipment. Given the complexity, thermal buoyancy driven turbulent flows represent a particularly difficult task for RANS models: "Inherent unsteadiness, energy nonequilibrium, counter-gradient diffusion, strong pressure fluctuations, and lack of universal scaling, all believed to be associated with distinct large-scale coherent eddy structures, are hardly tractable by Reynolds-type averaging." (Hanjalić 2002). See also Hanjalić and Vasić (1993) for a thorough discussion.

Smale et al. (2006) evince, that simulations using RANS methods for the representation of a coupled velocity and temperature distribution in the field of applied cooling between 1974 and 2006 show low accuracy and large deviations from experimental data. Later, Ambaw et al. (2013) summarized studies on the cooling of harvested food, indicating some progress being made between 2006 and 2013 concerning the accuracy of the models. Although, with simulations mainly based on Reynolds-averaging turbulence models such as the k-ϵ or shear stress transport (SST) model (Delele et al. 2009; Moureh et al. 2009a; Moureh et al. 2009b; Defraeye et al. 2010), they concluded that a clear increase in the accuracy of turbulent 3D simulations within complex cooled geometries compared with experimental data is still pending.

In some cases, RANS models are not even able to recover the mean flow characteristics correctly, for example if an unsteady heat transfer coupling is involved. To overcome this drawback, large eddy simulations (LES) are often suggested (e.g. Chandra et al. 2010; Salim and Ong 2013; Romanazzi and Howey 2015). LES offer an alternative approach to RANS, where the large turbulent structures are resolved by the simulation, while small structures are modeled, see e.g. Fröhlich (2006) for an introduction. As opposed to RANS methods, de-

tailed unsteady simulations are achieved with better turbulence representation (Fröhlich and Terzi 2008). However, a much finer grid and an unsteady solver are necessary to assure accurate results, which is usually accompanied by high computational demand and challenging mesh generation. This currently limits its broad application in the industry, which is – with increasing computational capacities and easier access through the cloud – awaited for 2030 (Slotnick et al. 2014).

1.2 Large Eddy Simulations using the Lattice Boltzmann Method

To reduce the computational costs of LES, a lattice Boltzmann method (LBM) is investigated in the scope of this thesis. As opposed to traditional CFD solvers based on the finite volume method (FVM), LBM does not directly solve for the Navier-Stokes equations (NSE), but rather for the discretized Boltzmann equation – also known as lattice Boltzmann equation (LBE), see e.g. Succi (2001a) or Krüger et al. (2017) for an introduction. While the non-linear advection term in the NSE is challenging to deal with algorithmically, the LBE only involves linear advection. Due to a collision term, which is non-linear but computable as a function of cell-local values, and a simple structured mesh, LBM is simple to parallelize. Thus, LBM provides a very fast method for unsteady fluid dynamics, which efficiently uses parallel computers with tens of thousands of CPU cores or several GPUs and allows large computational grids with well over one hundred million cells (Feichtinger et al. 2009; Xian and Takayuki 2011).

With its remarkable scalability on parallel computer hardware, the LBM gained attention in cases of turbulent flow simulations, especially in conjunction with LES in the last years (Aidun and Clausen 2010). A number of studies have investigated the applicability of the LBM for the simulation of turbulence by means of direct numerical simulations (DNS), LES and RANS, see the review article by Jahanshaloo et al. (2013). The application of LBM on LES methodology has shown to provide a significant speedup over traditional FVMs, for example in the works of Jacob et al. (2019) or Barad et al. (2017), where a speedup factor of about twelve is achieved for simulations on similar grids and with similar accuracy. Haussmann et al. (2020) recently found LBM to be on average 32 times faster than FVM comparing wall modeled LES in an internal combustion engine using open source packages OpenLB and OpenFOAM. According to Löhner (2019), LES-LBM might even be the first method in the close future to

enable overnight simulations on an industrial scale in the order of one billion grid cells.

Although a number of LES models have been applied to the LBM – see Hou et al. (1994), Ansumali et al. (2004), Premnath et al. (2009), and Weickert et al. (2010), among others – these approaches are much younger than their counter-parts for the NSE and their application is premature. The first LBM-LES model based on standard Smagorinsky eddy viscosity was proposed by Hou et al. (1994). Teixeira (1998) further discussed incorporation methods for the k-ϵ and RNG turbulence models into the lattice Boltzmann algorithm. Ansumali et al. (2004) applied the filtering directly to the Boltzmann equation and propose a subgrid model based on kinetic theory. Dong et al. (2008) extended Hou's approach to be consistent in the inertial range and later Premnath et al. (2009) complement a dynamic procedure to calculate model constants. Weickert et al. (2010) developed and investigated an LBM scheme for the wall adaptive large eddy model (WALE). Malaspinas and Sagaut (2012) proposed consistent sub grid closures for the filtered Bhatnagar-Gross-Krook (BGK) Boltzmann equation derived from a Hermite series expansion.

Besides LES models based on eddy viscosity approximations, the approximate deconvolution model has been introduced to the LBM (Sagaut 2010; Malaspinas and Sagaut 2011) and extended with adaptive filtering (Nathen et al. 2018). While these studies apply wall resolved LES, near wall models have also been proposed within the framework of LBM by Malaspinas and Sagaut (2014), Haussmann et al. (2019) and Pasquali et al. (2020).

1.3 Thermal Lattice Boltzmann Methods

A variety of approaches for thermal fluid flows in the LBM have been proposed, see He et al. (2019) for a comprehensive overview. One promising candidate for thermal flow dynamics with the LBM is the double distribution function method (DDF) first proposed by Bartoloni et al. (1993), where a second LBE is solved to obtain the temperature distribution. This approach allows for solving problems with a wide range of Prandtl numbers – i.e. the ratio between the fluid's kinematic viscosity and its thermal diffusivity (Schlichting and Gersten 2016) – and a straightforward implementation using existing code and memory structures.

As opposed to Zhou et al. (2004) and Treeck et al. (2006), who used hybrid thermal models for their LBM-based LES, LBM's locality and associated par-

allelizability can be preserved, even when complemented by a thermal LES model, as has been first shown by H. Liu et al. (2006). This model has been widely adopted by e.g. Sajjadi et al. (2011), Wu et al. (2011), and S. Chen (2012), who conducted comparison studies against popular benchmark test cases. Khan et al. (2015) used an LBM and compared it to an FVM-based LES, studying the turbulent air flow and temperature field in a four-bed hospital room. At an urban scale, Obrecht et al. (2015) carried out simulations of a small village and the velocity and temperature distributions between single houses. Tiftikci and Kocar (2016) investigated heat distribution inside a prototype fast breeder reactor by LBM simulations, comparing their findings with experimental data. Yuan et al. (2017) used GPU computations on 250 million grid points to examine the thermal comfort of indoor air flows. Most of the cited authors use the multiple relaxation time (MRT) collision operator for turbulent flows since the BGK collision operator is described unstable for flows with high Reynolds numbers. The MRT scheme, however, is not without controversy as it includes a number of adjustable parameters that were fit in order to obtain a larger stability domain (Lallemand and L. S. Luo 2000).

Many of the above models have so far been applied to basic benchmark cases for simple geometries and for laminar to mid range turbulent cases, e.g. Bartoloni et al. (1993), Eggels and Somers (1995), Shan (1997), Guo et al. (2002a), Shi and Guo (2003), Dixit and Babu (2006), and Guo et al. (2007). Whether these approaches reliably work for a wide range of engineering problems concerning stability, robustness and accuracy, has not been adequately investigated and remains a question to be examined. A comprehensive validation of this approach therefore motivates this work.

Subsequently, the tested method is applied to a critical problem for which an increased interest has emerged in recent years: To limit climate change it is necessary to convert to sustainable transport. Trucks in particular are responsible for a proportionately large amount of greenhouse gas emission (Van der Zwaan et al. 2013). While there are initial approaches for the electrification of trucks (Davis and Figliozzi 2013), sustainable refrigerated transport of, for example, food, medicines, organ or blood donations remains insufficiently addressed. The specific challenges in regard to heat transfer in refrigerated trucks are therefore presented in the following section.

1.4 Application to Heat Transfer in Refrigerated Trucks

Refrigeration of deep-frozen food poses a special challenge since particularly strict guidelines apply, i.e. in the DIN 8959. The temperature of the frozen goods in the refrigerated vehicles must not exceed the prescribed maximum temperature of −18 °C at any time during the transport. To date, the energy required for cooling to maintain this temperature limit is provided by diesel-powered air-conditioning units, which induces CO_2 emissions, among other environmentally harmful substances (Tassou et al. 2009). Thus, two promising concepts to reduce the fuel consumption of refrigerated trucks are considered in this work:

Concept A: Insulation improvements using vacuum insulation panels (VIP),

Concept B: Passivization of the cooling effect by latent heat storages (LHS).

Application of Vacuum Insulation Panels

Efficient insulation of the walls is of crucial importance. Concept A exchanges previously used polyurethane rigid foam insulation (PUR) at all possible locations for vacuum isolation panels (VIP). VIPs consist of a highly porous core – for example made of silica – covered and evacuated, see Baetens et al. (2010b), Bouquerel et al. (2012), and Kalnæs and Jelle (2014) for an overview. These panels are characterized by thermal conductivities five to ten times lower than those of traditional insulation materials (Wegger et al. 2011; Bouquerel et al. 2012). VIPs are widely applied to buildings for thermal insulation of external facades (e.g. Simmler and Brunner 2005) with new areas of application being identified, most notably cooling and hot water technologies (Kalnæs and Jelle 2014). Using VIPs to improve insulation performance of refrigerated trucks, however, has not yet been studied and is thus pursued here using the proposed numerical scheme.

Application of Latent Heat Storages

Transport of refrigerated goods by electric vehicles will reduce emissions and pollution towards sustainability, which, however, is not yet technically feasible considering the limited range of electric vehicles (Al-Alawi and Bradley 2013; Hannan et al. 2017). Hence, concept B is aiming at providing the required refrigeration energy by a passive source, i.e. through thermal energy storages. Thermal energy storages have become an especially important component of

renewable and waste heat energy technologies (Spoletini 2016; Mumtaz et al. 2017). They are particularly advantageous in systems with intermittent and cyclic thermal loading – such as solar radiation on buildings or refrigerated vehicles – where the energy requirement for heating or cooling can be offset by storing the excess heat and releasing it during appropriate demand (Zalba et al. 2003; Baetens et al. 2010a). Thermal energy storage is typically accomplished by systems employing materials with high specific heat capacity or through the process of melting and solidification. Phase change materials (PCM) such as paraffins or salt hydrates have been found to be excellent candidates for such applications due to their high latent heats of fusion, chemical stability, availability over a wide range of temperatures and low cost (Farid et al. 2004; Anisur et al. 2013; Kasaeian et al. 2017; Sarbu 2018). Zalba et al. (2003) show a compilation of various phase change materials including solutions of salts with a suitable temperature range for the transport of refrigerated goods.

Modeling and simulation of thermal behavior as well as initial tests on combinations of VIP and LHS have been carried out by Ahmad et al. (2006) and Verma et al. (2008). M. Liu et al. (2012b), Marques et al. (2013), and Bista et al. (2018) studied the application of PCM for refrigerated systems and found reduction of energy consumption by up to 84 % compared to traditional AC systems. However, the detailed influence and interaction of latent heat storage with chilled goods and insulation with regard to the application inside refrigerated vehicles has not yet been investigated. Nevertheless, this is necessary for effective use and eventually for the complete replacement of the air conditioning system in refrigerated vehicles. Measurements in the vehicle's cooling body pose a particular challenge, since interactions between naturally convecting air, latent heat storage and cargo are difficult to assess. Furthermore, prototypes of refrigerated vehicles are very costly. For these reasons, high-resolution LES with thermal LBM are used in this thesis to numerically evaluate concepts and designs before physical construction.

High Performance Hybrid Phase Changing Materials

The appropriate selection of materials allows the application of PCMs over a range of temperatures. However, advantages such as their high latent heats of fusion are often offset by their poor thermal conductivities limiting their use in applications requiring precise rates of heating or cooling. Examples for such applications are accurate temperature control in process engineering, thermal management of electronics and batteries, as well as refrigerated trans-

port. Hence, several studies have looked into the possibility of controlling the melting or solidification rates using porous media of high thermal conductivity filled with PCM in a composite matrix, see Fan and Khodadadi (2011), L. Liu et al. (2016), and R. Singh et al. (2019) for an overview. PCMs complemented with highly open metal foams (porosity $> 90\,\%$) have substantially greater effective thermal conductivities than pure PCMs, and have been shown to increase the melting or solidification rates by three to 44 times for a fractional increase in size (Thapa et al. 2014; Xiao et al. 2014). Given the wide spectrum of potential substrate candidates – various open-cell foams and fibrous structures can be used sensibly – it is important to fully understand the interstitial thermal and phase-change physics to enable optimal designs of PCM-composites for any application.

Computational simulations on the pore scale, can aid characterizing the melting and solidification processes with isolated variations in governing micro structural properties. Although pore scale simulations of melting inside metal foams are possible today, the creation of high quality meshes is challenging due to the complex geometry (M. Wang and N. Pan 2008; Li et al. 2014a). This is especially true for conjugated heat transfer, which often requires matching grids for the respective material domains. In view of the computational scalability and parallel performance, optimal decomposition and load balancing of multiple meshes pose additional challenges. This usually limits the efficient use of a large number of CPUs for this application causing very long run times. In order to address these difficulties, the present work examines the suitability of an LBM-based solver. LBM has previously been applied to simulations of resolved porous structures and conjugate heat transfer – see e.g. C. Pan et al. (2004), M. Wang and N. Pan (2008), and Ross-Jones et al. (2019) among others – demonstrating its suitability for these applications. Meanwhile, its applicability to resolve melting on the pore scale remains an open question. For this reason, a total enthalpy based LBM algorithm is applied here to the simulation of melting of paraffin including conjugated heat transfer in two metal foam geometries.

1.5 Structure of this Thesis

As stated in Section 1.3, many LBM studies focus on model development, but up to now attention paid to thermal process engineering applications is marginal, while others – such as flow in porous media, immersed moving objects, multi-

phase or multi-component flows – are relatively well covered (Mohamad 2011; Krüger et al. 2017). This work therefore pursues model implementation within the open source LBM framework OpenLB (Krause et al. 2020) and subsequent application with a focus on robustness and validity for thermal engineering problems relating, but not limited to cooling and refrigeration.

This thesis includes publications that were accomplished in the context of my doctorate. This results in the following structure of the thesis:

1. First, the double distribution thermal LBM is extended by a Smagorinsky-type subgrid scale turbulence model and implemented into OpenLB in this work. The corresponding governing equations and the present model are briefly introduced in Chapter 2.

2. Then, a rigorous validation is conducted against analytic solutions, simulation data and against results of measurements in order to assure robustness and accuracy for a wide range of discretization parameters. This validation study is part of the first two publications included in this thesis and will be presented in Chapters 3 and 4.

3. The developed and validated simulation work flow is subsequently used to gain deeper understanding of the heat transfer in a refrigerated truck and improve its thermal management using vacuum insulation panels (VIP) and latent heat storages (LHS). This is part of the third publication included in this thesis and will be presented in Chapter 5.

4. Transport of deep-frozen goods requires a high amount of cooling energy over a brief period of time shortly after a door has been opened. For this reason, LHS need to be designed with specific care for this application. Improving the effective thermal conductivity of such storages using highly porous metal foams is thus considered. Corresponding simulation of melting in resolved porous structures using LBM is part of the fourth publication included in this thesis and will be presented in Chapter 6.

5. Finally, a summary over the present work's achievements complemented by an overall conclusion is given in Chapter 7. This is followed by a detailed outlook and discussion of ideas for future work derived from the findings of the simulation studies performed.

2
Mathematical Model and Numerical Method

2.1 Field Equations for Flows of Newtonian Fluids

The Navier-Stokes equations describe the flow of viscous substances in the continuum regime. In computational fluid dynamics (CFD), the Navier-Stokes equations are understood to be the conservation equations of momentum, mass and energy. The derivation of these conservation equations including utilized assumptions is summarized briefly in the following; for a more detailed derivation the interested reader is referred to White (2003) or Schlichting and Gersten (2016).

The conservation equations can be derived by drawing a balance around a control volume Ω with boundary $\partial\Omega$. For this approach, which is known as the control volume method (Ferzinger and Perić 2002), extensive quantities (such as mass and momentum) are described by intensive quantities (such as density ρ, pressure p and velocity $\boldsymbol{u}$). Intensive quantities have the advantage that they can be balanced independently of the size of the control volume under consideration. If the control volume is doubled, for example, the mass in the system under consideration is also doubled, but not the density or temperature (Stephan et al. 2013). An arbitrary extensive conservation property Φ can be transformed into its corresponding intensive conservation property φ with

$$\Phi = \int_{\Omega_m} \rho\,\varphi \,\mathrm{d}\Omega_m \tag{2.1}$$

by integrating over the volume of the control mass Ω_m.

With Equation 2.1 a universal transformation for conservation equations has been derived as (Ferzinger and Perić 2002)

$$\frac{\mathrm{d}\Phi}{\mathrm{d}t} = \frac{\mathrm{d}}{\mathrm{d}t}\int_{\Omega_m} \rho\varphi \,\mathrm{d}\Omega_m = \frac{\mathrm{d}}{\mathrm{d}t}\int_{\Omega} \rho\varphi \,\mathrm{d}\Omega + \int_{\partial\Omega} \rho\varphi(\boldsymbol{u}-\boldsymbol{u}_\Omega)\cdot\boldsymbol{n}\,\mathrm{d}\partial\Omega, \tag{2.2}$$

where $\boldsymbol{n}$ describes the unit vector perpendicular to the surface $\partial\Omega$ facing outwards, $\boldsymbol{u}$ the fluid velocity and $\boldsymbol{u}_\Omega$ the velocity at which Ω moves. In the following, Ω is assumed to be at rest, hence $\boldsymbol{u}_\Omega = 0$. Hereafter, Equation 2.2 is referred to as the control volume equation.

The mass m of a fluid in a control volume is assumed to remain unchanged over time, i.e. it is neither generated nor destroyed. Thus, we can write a conservation equation as

$$\frac{\mathrm{d}m}{\mathrm{d}t} = 0. \tag{2.3}$$

Replacing the left side of Equation 2.3 with the help of the general control volume equation (Equation 2.2) and using $\Phi = m$ and $\varphi = 1$ to obtain

$$m = \int_{\Omega_m} \rho \,\mathrm{d}\Omega_m. \tag{2.4}$$

The integral form of the continuity equation is given by

$$\frac{\mathrm{d}m}{\mathrm{d}t} = \frac{\partial}{\partial t}\int_{\Omega} \rho \,\mathrm{d}\Omega + \int_{\partial\Omega} \rho\boldsymbol{u}\cdot\boldsymbol{n}\,\mathrm{d}\partial\Omega = 0. \tag{2.5}$$

The Gauss theorem (see e.g. Katz 1979) now allows the surface integral to be transformed into a volume integral. This finally leads to the coordinate-free differential form of the mass conservation equation

$$\frac{\partial\rho}{\partial t} + \boldsymbol{\nabla}\cdot(\rho\boldsymbol{u}) = 0. \tag{2.6}$$

The same procedure can be applied on the conservation of momentum. The general conservation of momentum in the control volume is given by the equation

$$\frac{\mathrm{d}(m\boldsymbol{u})}{\mathrm{d}t} = \boldsymbol{F}, \tag{2.7}$$

where $\boldsymbol{u}$ the velocity and $\boldsymbol{F}$ the sum of forces acting on the control volume. By applying the control volume equation (Equation 2.2), Equation 2.7 can be written as

$$\frac{\partial}{\partial t}\int_{\Omega}\rho\boldsymbol{u}\,\mathrm{d}\Omega+\int_{\partial\Omega}\rho\boldsymbol{u}\boldsymbol{u}\cdot\boldsymbol{n}\,\mathrm{d}\partial\Omega=\int_{\Omega}\rho\boldsymbol{F}\,\mathrm{d}\Omega+\int_{\partial\Omega}\boldsymbol{T}\cdot\boldsymbol{n}\,\mathrm{d}\partial\Omega. \tag{2.8}$$

Assuming a Newtonian fluid, the the stress tensor $\boldsymbol{T}$ is given by (Dellar 2001)

$$\boldsymbol{T}=-p\boldsymbol{I}+2\mu\boldsymbol{S}-\left(\frac{2}{3}\mu-\mu_B\right)(\boldsymbol{\nabla}\cdot\boldsymbol{u})\boldsymbol{I} \tag{2.9}$$

with the unit matrix $\boldsymbol{I}$, the dynamic viscosity $\mu=\rho\nu$, kinematic viscosity ν of the Newtonian fluid and the bulk viscosity μ_B. The rate of strain tensor $\boldsymbol{S}$ is given by the symmetric part of the velocity gradient

$$\boldsymbol{S}=\frac{1}{2}\left(\boldsymbol{\nabla}\boldsymbol{u}+(\boldsymbol{\nabla}\boldsymbol{u})^{\mathrm{T}}\right). \tag{2.10}$$

The Gauss theorem can be used once more to transform the volume integrals. This leads to the conservation equation of momentum in coordinate-free vector form

$$\frac{\partial\rho\boldsymbol{u}}{\partial t}+\boldsymbol{\nabla}\cdot(\rho\boldsymbol{u}\boldsymbol{u})=\boldsymbol{\nabla}\cdot\boldsymbol{T}+\rho\boldsymbol{F}. \tag{2.11}$$

Further simplification of the quantity $\boldsymbol{T}$ assuming $\mu_B=\frac{2}{3}\mu$ leads to the non-conservative, weakly compressible formulation given by

$$\frac{\partial\rho\boldsymbol{u}}{\partial t}+\boldsymbol{\nabla}\cdot(\rho\boldsymbol{u}\boldsymbol{u})=-\boldsymbol{\nabla}p+\boldsymbol{\nabla}\cdot(2\mu\boldsymbol{S})+\rho\boldsymbol{F}. \tag{2.12}$$

In this thesis the transport of heat is also to be simulated. According to the first law of thermodynamics, the internal energy $e=c_p\rho T$ is preserved in a closed system, which does not perform any volume work, where c_p is the specific heat capacity at constant pressure and T is the temperature. Thus, the conservation equation of internal energy is given by

$$\frac{\partial}{\partial t}\int_{\Omega}c_p\rho T\,\mathrm{d}\Omega+\int_{\partial\Omega}c_p\rho T\boldsymbol{u}\cdot\boldsymbol{n}\,\mathrm{d}\partial\Omega=\sum q+Q, \tag{2.13}$$

where $\sum q$ represents all transport mechanisms of the heat, except convection. Sources and sinks can be described by Q (for example dissipation, radiation or

chemical reactions), which are neglected hereafter. Together with Fourier's law of heat conduction

$$\sum q = q^d = \int_{\partial\Omega} (\lambda \boldsymbol{\nabla} T) \cdot \boldsymbol{n} \, \mathrm{d}\partial\Omega, \tag{2.14}$$

where the thermal conductivity is given by λ. Inserting Equation 2.14 into Equation 2.13 yields

$$\frac{\partial}{\partial t} \int_{\Omega} c_p \rho T \, \mathrm{d}\Omega + \int_{\partial\Omega} c_p \rho T \boldsymbol{u} \cdot \boldsymbol{n} \, \mathrm{d}\partial\Omega = \int_{\partial\Omega} (\lambda \boldsymbol{\nabla} T) \cdot \boldsymbol{n} \, \mathrm{d}\partial\Omega. \tag{2.15}$$

Using the Gauss theorem, the coordinate-free differential form of the advection-diffusion equation for the internal energy finally is

$$\frac{\partial c_p \rho T}{\partial t} + \boldsymbol{\nabla} \cdot (c_p \rho T \boldsymbol{u}) = \boldsymbol{\nabla} \cdot (\lambda \boldsymbol{\nabla} T). \tag{2.16}$$

In order to incorporate the effects of natural convection, the well-known Boussinesq approximation is adopted in this work (see e.g. Ferzinger and Perić 2002). Assuming relatively small changes in the temperature the fluid's density is approximated by a linear function of the temperature resulting in a buoyancy force

$$\boldsymbol{F} = -\rho \beta \boldsymbol{g} \, (T - T_0), \tag{2.17}$$

where T_0, β and $\boldsymbol{g}$ denote the reference temperature, the expansion coefficient and the gravitational acceleration, respectively. All other material properties are assumed to be constant.

It should be noted, that the governing equations presented above form a two-way coupled system. This is achieved by using the velocity from Equation 2.11 as the advection velocity in Equation 2.15 in the one way, and through using the temperature-dependent buoyancy force (Equation 2.17) in Equation 2.11 in the other way.

2.2 Turbulence Modeling

Temperature-dependent buoyancy forces can lead to time-dependent, turbulent phenomena. In general, turbulent flows are characterized by their chaotic, three-dimensional and time-dependent vortexes, that occur on a range of scales (compare e.g. Fröhlich 2006). The Reynolds number – respectively the ratio of inertia to viscosity effects – is often used to classify a flow as

either laminar or turbulent. For flows with a high Reynolds number, inertia effects dominate, which lead to three-dimensional velocity variations in the flow field. These fluctuations occur over a wide range on both, time and length scales.

A turbulent flow can further be distinguished between statistically steady and statistically unsteady, where the former describes time-dependent fluctuations around a time-independent mean flow. Contrary, the latter describes time-dependent fluctuations around an also time-dependent mean flow, for which the turbulent Kármán vortex street is a popular example (Oertel 2017). In addition to turbulent flows, there are also time-dependent phenomena, that only appear during a relatively short time span such as the transition from a laminar to turbulent flow or boundary layer. The term *transition* is not be mixed up with the term *transient*, which is used equivalent to *time-dependent* and *unsteady* throughout this thesis.

One approach to the resolution of turbulent flows is to discretize the spatial and temporal domain to detect even the smallest turbulent structure. This method, known as direct numerical simulation (DNS), does not require turbulence modeling, but is extremely expensive in terms of computation. Therefore, other numerical approaches have been developed to approximate the nature of turbulent flows – the Reynolds-averaging method and large eddy simulations (LES). Both methods are briefly described in the following sections.

2.2.1 Reynolds-Averaged Navier-Stokes Equations

Reynolds-averaging begins by expressing a variable ϕ as the sum of the mean value of that variable $\langle\phi\rangle$ over time and the fluctuation of that variable ϕ'' about the mean value,

$$\phi(\boldsymbol{x},t) = \langle\phi\rangle(\boldsymbol{x}) + \phi''(\boldsymbol{x},t). \tag{2.18}$$

For an overview of possible averaging operators, please refer to Fröhlich (2006). By applying this technique to the Navier-Stokes equations – i.e. writing all variables as the sum of the time-averaged value and the fluctuating value – the Reynolds-averaged Navier-Stokes equations (RANS) are obtained in tensor notation (Ferziger and Peric 2008)

$$\boldsymbol{\nabla}\cdot(\rho\langle\boldsymbol{u}\rangle) = 0, \tag{2.19}$$

$$\boldsymbol{\nabla}\cdot(\rho\langle\boldsymbol{u}\rangle\langle\boldsymbol{u}\rangle) + \boldsymbol{\nabla}\cdot(\rho\langle\boldsymbol{u}''\boldsymbol{u}''\rangle) = -\boldsymbol{\nabla}\langle p\rangle + \boldsymbol{\nabla}\cdot(2\mu\langle\boldsymbol{S}\rangle) + \rho\boldsymbol{F}. \tag{2.20}$$

Due to the fluctuations in the velocity field the Reynolds-averaging of the Navier-Stokes equations leads to a new stress term $\rho\langle \boldsymbol{u}''\boldsymbol{u}''\rangle$, which is called the Reynolds stress term.

Finally, the equation for the mean value of internal energy $c_p\rho\langle T\rangle$ can be written as (Ferziger and Peric 2008)

$$\boldsymbol{\nabla}\cdot(c_p\rho\langle T\rangle\langle \boldsymbol{u}\rangle)+\boldsymbol{\nabla}\cdot(c_p\rho\langle T''\boldsymbol{u}''\rangle)=\boldsymbol{\nabla}\cdot(\lambda\boldsymbol{\nabla}\langle T\rangle), \tag{2.21}$$

where the additional term $c_p\rho\langle T''\boldsymbol{u}''\rangle$, known as the turbulent heat flux, appears due to the averaging procedure.

Given the presence of the Reynolds stresses and the turbulent heat flux, the averaged conservation equations contain more unknowns than there are equations. Solving these equations requires the use of approximations, which is often referred to *closing* the set of equations. This is usually achieved by specifying the Reynolds stress tensor and the turbulent heat flux as functions of the averaged quantities and empirical parameters. Numerous such turbulence models have been developed, see for example Rodi (1993) for an overview.

2.2.2 Filtered Navier-Stokes Equations

Despite the advantage of RANS – turbulent structures are not required to be resolved and all unsteady effects are modeled, resulting in a very fast steady-state algorithm – the large scales of turbulent flows are determined by their individual configuration and are therefore difficult to capture by a universally valid model (Fröhlich 2006). The large scale structures also account for the majority of turbulent energy. Consequently, the idea of LES is based on explicitly resolving and calculating the large scales while modeling the small scales. So, only a small part of the kinetic energy needs to be modeled. Furthermore, the universal character of the small scales makes them more accessible for modeling, which is already accomplished by simple eddy viscosity models (Fröhlich 2006) as shown in the following paragraphs.

LES is based on the separation into large and small scales, referred to as grid-scale and subgrid-scale. So, a scalar ϕ is subdivided into the two parts

$$\phi(\boldsymbol{x},t)=\overline{\phi}(\boldsymbol{x},t)+\phi'(\boldsymbol{x},t), \tag{2.22}$$

where $\overline{\phi}$ is the resolved grid-scale part and ϕ' represents the subgrid-scale part. While several approaches for the separation of scales have been developed, the approach based on a spacial filter operation proposed by Leonard (1975) is the

commonly used. With the filter kernel $G_\triangle$, the filtered value $\overline{\phi}$ is given by the one-dimensional convolution integral (Fröhlich 2006)

$$\overline{\phi}(x) = \int G_\triangle(x-y)\phi(y)\,\mathrm{d}y, \tag{2.23}$$

where $x, y \in \Omega$ and $\triangle$ is the filter width. Applying the spatial filter operation to the NSE results in the filtered NSE

$$\frac{\partial \overline{\rho}}{\partial t} + \boldsymbol{\nabla}\cdot(\overline{\rho}\,\overline{\boldsymbol{u}}) = 0, \tag{2.24}$$

$$\frac{\partial \overline{\rho}\,\overline{u}}{\partial t} + \boldsymbol{\nabla}\cdot(\overline{\rho}\,\overline{\boldsymbol{u}}\,\overline{\boldsymbol{u}}) + \boldsymbol{\nabla}\cdot(\overline{\rho}\,\boldsymbol{\Pi}) = -\boldsymbol{\nabla}\overline{p} + \boldsymbol{\nabla}\cdot(2\mu\overline{\boldsymbol{S}}) + \overline{\rho}\boldsymbol{F}, \tag{2.25}$$

where, similar to the RANS equations, $\overline{\rho}\,\boldsymbol{\Pi} = \overline{\rho}\,(\overline{\boldsymbol{u}\boldsymbol{u}} - \overline{\boldsymbol{u}}\,\overline{\boldsymbol{u}})$ represents the non-resolved part of the momentum flux, that occurs due to the filtering operation. Here again, a model is needed to close the set of filtered equations. With such a model – referred to as subgrid-scale models – LES aims to discretize only the grid-scale parts of the solution, which then only requires a coarser lattice than would be required for the DNS. The filtering is thus implicitly introduced by the chosen discretization. Consequently, in most implicit approaches the filter width $\triangle$ is chosen in dependence of the grid width.

A common approach to model the subgrid-scale stress is the eddy viscosity model

$$\boldsymbol{\Pi} \approx \boldsymbol{\Pi}^{mod} = -2\nu_{\text{turb}}\overline{\boldsymbol{S}}. \tag{2.26}$$

Using the mixing-length approximation yields the well-known Smagorinsky model (1963) for the eddy viscosity

$$\nu_{\text{turb}} = (C_S\triangle)^2\sqrt{2\,\overline{\boldsymbol{S}}\,\overline{\boldsymbol{S}}}, \tag{2.27}$$

where C_S is the Smagorinsky constant.

Applying the same filter operation to the advection-diffusion equation for the internal energy, the filtered advection-diffusion equation can be written as

$$\frac{\partial c_p\overline{\rho}\,\overline{T}}{\partial t} + \boldsymbol{\nabla}\cdot(c_p\overline{\rho}\,\overline{T}\,\overline{\boldsymbol{u}}) + \boldsymbol{\nabla}\cdot(c_p\overline{\rho}\boldsymbol{q}) = \boldsymbol{\nabla}\cdot(\lambda\boldsymbol{\nabla}\overline{T}), \tag{2.28}$$

where, analogously to $\overline{\rho}\boldsymbol{\Pi}$ in the filtered NSE, $c_p\overline{\rho}\boldsymbol{q} = c_p\overline{\rho}\,(\overline{T\boldsymbol{u}} - \overline{T}\,\overline{\boldsymbol{u}})$ represents the subgrid-scale heat flux. Commonly, this term is modeled using the eddy diffusivity model (Eidson 1985)

$$\boldsymbol{q} \approx \boldsymbol{q}^{mod} = -\alpha_{\text{turb}}\boldsymbol{\nabla}\overline{T}. \tag{2.29}$$

Following the similarity hypothesis, the turbulent diffusion coefficient α_{turb} is simply expressed as a function of the eddy viscosity with

$$\alpha_{\text{turb}} = \frac{\nu_{\text{turb}}}{\text{Pr}_{\text{turb}}}, \tag{2.30}$$

where the turbulent Prandtl number Pr_{turb} is a model constant.

Due to its simplicity, the Smagorinsky model is very popular. However, in the proximity to walls and for well resolved grid cells under the influence of shear, the subgrid-scale stress should tend to zero, which does not hold for the Smagorinsky model. So, the model is overly dissipative in these cases. Hence, a number of model extensions have been proposed in the literature – some more, others less physical consistent (Silvis et al. 2017). These improvements are accompanied by considerable additional implementation and computational effort, while the gain in accuracy is not significant for many applications (Piomelli 1998). Therefore, the standard Smagorinsky model is used in this thesis. A more elaborate discussion is given in Chapter 7.

The two previous Sections 2.1 and 2.2 are based on the textbooks by Ferzinger and Perić (2002) and Fröhlich (2006). For a more in-depth derivation of the equations and more detailed explanations it is recommended to consult these books and the literature cited therein.

2.3 Lattice Boltzmann Method

2.3.1 Kinetic Theory and the Boltzmann Equation

An alternative approach for the description of fluid flows is provided by kinetic theory of gases, see e.g. Hänel (2004) for an introduction. Here, the fluid is not, as in the control volume approach in the previous section, assumed to be a continuum, but the gas is rather presumed to consist of a very large number of small particles (i.e. atoms or molecules). It is further assumed that the particles move on trajectories as described by Newton's laws of mechanics. After a certain distance, collisions occur, which cause the particles to change momentum and their respective direction of motion.

In practice, however, it is not possible to simulate the flow by means of single particle representation because of the huge number of particles even for very small volumes. There are even about 10^{19} molecules in one liter of gas at standard state. Since the motion of the individual particle is usually not important for applications anyway, but the macroscopic effects of the many

individual motions, the dynamics of the lot of the particles are considered statistically. Thus, quantities such as velocity, density, pressure and temperature can still be determined. For this purpose a distribution function $f(\boldsymbol{x}, \xi, t)$ is introduced, which describes the probability of a gas particle being at a certain place $\boldsymbol{x}$ moving in a certain velocity direction ξ at a certain time t. The temporal and spatial variations of this distribution function are described by the Boltzmann equation (Krüger et al. 2017)

$$\frac{\partial f}{\partial t} + \xi \nabla f + \frac{\boldsymbol{F}}{\rho} \cdot \nabla_{\xi} f = \Omega(f), \tag{2.31}$$

where $\Omega(f)$ is the collision operator, which in its original form (see e.g. Lerner and Trigg 2005) is a double integral over the particle velocity space. To solve this integro-differential equation the collision integral on the right hand side is usually replaced by the model according to Bhatnagar, Gross and Krook (BGK, 1954)

$$\Omega(f) = -\frac{1}{\tau}(f - f^{eq}), \tag{2.32}$$

assuming that the fluid locally relaxes towards the equilibrium distribution f^{eq} over a characteristic relaxation time τ. This relaxation time determines the kinematic viscosity – the greater the kinematic viscosity, the longer it takes for the described system to reach its equilibrium state.

The equilibrium distribution is given by the Maxwell-Boltzmann distribution

$$f^{eq} = \rho \left(\frac{1}{2\pi RT} \right)^{d/2} \exp\left(-\frac{|\xi - \boldsymbol{u}|^2}{2RT} \right), \tag{2.33}$$

which is an analytical solution of the Boltzmann equation for the case of a gas in thermodynamic equilibrium using symmetry properties (Hänel 2004), where R is the gas constant and d is the number of spatial dimensions. Density ρ, velocity $\boldsymbol{u}$ and temperature T are connected to the particle distribution function through respective moments (Krüger et al. 2017)

$$\rho(\boldsymbol{x}, t) = \int f(\boldsymbol{x}, \xi, t) \, \mathrm{d}\xi, \tag{2.34}$$

$$\rho(\boldsymbol{x}, t) \, \boldsymbol{u}(\boldsymbol{x}, t) = \int \xi f(\boldsymbol{x}, \xi, t) \, \mathrm{d}\xi, \tag{2.35}$$

$$\frac{d}{2} R \rho(\boldsymbol{x}, t) \, T(\boldsymbol{x}, t) = \frac{1}{2} \int |\xi - \boldsymbol{u}(\boldsymbol{x}, t)|^2 f(\boldsymbol{x}, \xi, t) \, \mathrm{d}\xi. \tag{2.36}$$

2.3.2 Discretizing the Boltzmann Equation

The Boltzmann equation could be discretized with respect to all seven dimensions of f. However, this is quite costly regarding the computational, memory and programming effort. Instead, the velocity space is discretized first using either the Mach number expansion or the Hermite series expansion (Krüger et al. 2017). Here, the Hermite series expansion is presented for its solid mathematical foundation.

The starting point of the series expansion are Hermite polynomials, which n-th order is given in d spatial dimensions with (Krüger et al. 2017)

$$\boldsymbol{H}^{(n)}(\boldsymbol{x}) = \frac{(-1)^n}{\omega(\boldsymbol{x})} \boldsymbol{\nabla}^{(n)} \omega(\boldsymbol{x}), \tag{2.37}$$

where the weight function is given by

$$\omega(\boldsymbol{x}) = \frac{1}{(2\pi)^{d/2}} \exp\left(\frac{-\boldsymbol{x}^2}{2}\right). \tag{2.38}$$

It should be noted, that both, $\boldsymbol{H}^{(n)}$ and $\boldsymbol{\nabla}^{(n)}$, are tensors of rank n. An extensive overview of the mathematical properties of Hermite polynomials is given by Grad (1949).

This Hermite series expansion is applied to the distribution function f

$$f(\boldsymbol{x}, \xi, t) = \omega(\xi) \sum_{n=0}^{\infty} \frac{1}{n!} \boldsymbol{a}^{(n)}(\boldsymbol{x}, t) \cdot \boldsymbol{H}^{(n)}(\xi), \tag{2.39}$$

where the coefficients $\boldsymbol{a}^{(n)}$ are given by

$$\boldsymbol{a}^{(n)}(\boldsymbol{x}, t) = \int f(\boldsymbol{x}, \xi, t) \boldsymbol{H}^{(n)}(\xi) \, \mathrm{d}\xi \tag{2.40}$$

and the full tensor contraction is understood.

Using the derivative property of Hermite polynomials allows to rewrite the forcing contribution to (Shan et al. 2006)

$$\frac{\boldsymbol{F}(\xi)}{\rho} \cdot \boldsymbol{\nabla}_{\xi} f = -\frac{\boldsymbol{F}(\xi)}{\rho} \cdot \omega(\xi) \sum_{n=0}^{\infty} \frac{1}{n!} n \boldsymbol{a}^{(n-1)} \cdot \boldsymbol{H}^{(n)}(\xi). \tag{2.41}$$

Similarly, the series expansion is applied to the equilibrium distribution function

$$f^{eq}(\rho, \boldsymbol{u}, T, \xi) = \omega(\xi) \sum_{n=0}^{\infty} \frac{1}{n!} \boldsymbol{a}^{(n),eq}(\rho, \boldsymbol{u}, T) \cdot \boldsymbol{H}^{(n)}(\xi), \tag{2.42}$$

with

$$\boldsymbol{a}^{(n),eq}(\rho,\boldsymbol{u},T)=\int f^{eq}(\rho,\boldsymbol{u},T,\xi)\boldsymbol{H}^{(n)}(\xi)\,\mathrm{d}\xi. \tag{2.43}$$

Comparing the Maxwell-Boltzmann equilibrium distribution (Equation 2.33) with the weight function (Equation 2.38) gives

$$f^{eq}(\rho,\boldsymbol{u},T,\xi)=\rho\left(\frac{1}{2\pi RT}\right)^{d/2}\exp\left(-\frac{|\xi-\boldsymbol{u}|^2}{2RT}\right)=\frac{\rho}{T^{d/2}}\omega\left(\frac{\xi-\boldsymbol{u}}{\sqrt{RT}}\right). \tag{2.44}$$

The series coefficients can be calculated through

$$\boldsymbol{a}^{(n),eq}=\frac{\rho}{T^{d/2}}\int\omega\left(\frac{\xi-\boldsymbol{u}}{\sqrt{T}}\right)\boldsymbol{H}^{(n)}(\xi)\,\mathrm{d}\xi. \tag{2.45}$$

So, for example, the first four coefficients are

$$a^{(0),eq}=\rho, \tag{2.46}$$

$$\boldsymbol{a}^{(1),eq}=\rho\boldsymbol{u}_\alpha, \tag{2.47}$$

$$\boldsymbol{a}^{(2),eq}_{\alpha\beta}=\rho(\boldsymbol{u}_\alpha+\boldsymbol{u}_\beta+(T-1)\delta_{\alpha\beta}), \tag{2.48}$$

$$\boldsymbol{a}^{(3),eq}_{\alpha\beta\gamma}=\rho\left(\boldsymbol{u}_\alpha\boldsymbol{u}_\beta\boldsymbol{u}_\gamma+(T-1)(\delta_{\alpha\beta}\boldsymbol{u}_\gamma+\delta_{\beta\gamma}\boldsymbol{u}_\alpha+\delta_{\alpha\gamma}\boldsymbol{u}_\beta)\right). \tag{2.49}$$

The Hermite series expansion has the advantage, that these coefficients are directly related to the conserved moments of the Boltzmann equation given in Equation 2.36 (Krüger et al. 2017). In particular,

$$a^{(0),eq}=\rho=\int f\,\mathrm{d}\xi=a^{(0)}, \tag{2.50}$$

$$\boldsymbol{a}^{(1),eq}_\alpha=\rho\boldsymbol{u}_\alpha=\int f\xi_\alpha\,\mathrm{d}\xi=\boldsymbol{a}^{(1)}_\alpha, \tag{2.51}$$

$$\frac{1}{2}\left(\boldsymbol{a}^{(2),eq}_{\alpha\alpha}+\rho d\right)=\rho E=\int\frac{1}{2}f|\xi-\boldsymbol{u}|^2\,\mathrm{d}\xi=\frac{1}{2}\left(\boldsymbol{a}^{(2)}_{\alpha\alpha}+\rho d\right). \tag{2.52}$$

In order to fulfill the conservation laws needed for fluid flows, the first three terms of the Hermite series expansion are sufficient. Consequently, it is possible to truncate higher orders of the series, while maintaining the exact moments of the distribution. Limiting the series to the order N gives

$$f(\rho,\boldsymbol{u},T,\xi)\approx\omega(\xi)\sum_{n=0}^{N}\frac{1}{n!}a^{(n)}(\rho,\boldsymbol{u},T)\cdot\boldsymbol{H}^{(n)}(\xi), \tag{2.53}$$

$$f^{eq}(\rho,\boldsymbol{u},T,\xi)\approx\omega(\xi)\sum_{n=0}^{N}\frac{1}{n!}a^{(n),eq}(\rho,\boldsymbol{u},T)\cdot\boldsymbol{H}^{(n)}(\xi). \tag{2.54}$$

The velocity discrete Boltzmann equation is now obtained by exchanging the continuous velocity space ξ by a set of q discrete velocities $\{\xi_i\}$. Hence, we obtain

$$\frac{\partial f_i}{\partial t} + \xi_i \nabla f_i + \frac{\boldsymbol{F}}{\rho} \cdot \nabla_{\xi_i} f_i = -\frac{1}{\tau}(f_i - f_i^{eq}), \tag{2.55}$$

where $i = 1, \ldots, q$. These velocity sets are chosen so that q is sufficient in order to allow consistent solutions of the underlining target equation, while keeping the memory footprint and computational effort as small as possible. Usually, the resulting sets are referred to by DdQq, see Wolf-Gladrow (2000) or Krüger et al. (2017) for an overview of the available sets and their respective features. In this thesis the most common sets D2Q9 and D3Q19 are adopted.

Rather than from continuous integrals, the moments are now computed from finite sums

$$\rho(\boldsymbol{x}, t) = \sum_i f_i(\boldsymbol{x}, t), \tag{2.56}$$

$$\rho(\boldsymbol{x}, t)\,\boldsymbol{u}(\boldsymbol{x}, t) = \sum_i \xi_i f_i(\boldsymbol{x}, t). \tag{2.57}$$

The discrete velocity Boltzmann equation is now discretized in space and time. By applying the trapezoidal rule and a shift of variables (Krüger et al. 2017) the lattice Boltzmann equation is obtained

$$f_i(\boldsymbol{x} + \xi_i \Delta t, t + \Delta t) = f_i(\boldsymbol{x}, t) - \frac{\Delta t}{\tau}\left(f_i(\boldsymbol{x}, t) - f_i^{eq}(\rho, \boldsymbol{u})\right) + \boldsymbol{F}_i, \tag{2.58}$$

where Δt and $\xi_i \Delta t = \Delta x$ are the time and space resolutions. $\boldsymbol{F}_i$ represents a discrete forcing term for which the exact form is given by Guo et al. (2002c). The relaxation time is found through a Chapman-Enskog expansion (Krüger et al. 2017)

$$\nu = c_s^2 \left(\tau - \frac{1}{2}\Delta t\right), \tag{2.59}$$

where c_s is the lattice speed of sound. For a straightforward implementation of the method, the iterative solution of Equation 2.58 is split into two steps:

1. the local *collision step*, resulting in intermediate distribution functions

$$f_i^*(\boldsymbol{x}, t) = f_i(\boldsymbol{x}, t) - \frac{\Delta t}{\tau}\left(f_i(\boldsymbol{x}, t) - f_i^{eq}(\rho, \boldsymbol{u})\right) + \boldsymbol{F}_i, \tag{2.60}$$

2. and the *streaming step*,

$$f_i(\boldsymbol{x} + \xi_i \Delta t, t + \Delta t) = f_i^*(\boldsymbol{x}, t), \tag{2.61}$$

where the intermediate distributions are communicated to their discrete neighbor positions $\boldsymbol{x} + \boldsymbol{\xi}_i \Delta t$.

While choosing the truncation of the Hermite series expansion to $N = 2$ leads to the weakly compressible Navier-Stokes equation, a truncation with $N = 1$ gives the advection-diffsion equation (Mohamad 2011). Consequently, a second distribution function g_i is introduced in order to solve for the advection-diffusion equation for the temperature with

$$g_i(\boldsymbol{x} + \boldsymbol{\xi}_i \Delta t, t + \Delta t) = g_i(\boldsymbol{x}, t) - \frac{\Delta t}{\tau_g} \left(g_i(\boldsymbol{x}, t) - g_i^{eq}(T, \boldsymbol{u}) \right), \tag{2.62}$$

where τ_g is the relaxation time regarding the distribution function g_i. Here, the relaxation time is related to the diffusion coefficient of the advection-diffusion equation, which is found through a Chapman-Enskog expansion (Krüger et al. 2017)

$$\alpha = c_s^2 \left(\tau_g - \frac{1}{2} \Delta t \right). \tag{2.63}$$

The temperature is calculated from the zeroth moment of the distribution with

$$T(\boldsymbol{x}, t) = \sum_i g_i(\boldsymbol{x}, t), \tag{2.64}$$

while $\boldsymbol{u}$ entering the equilibrium distribution is given from Equation 2.57.

It should be noted, that the two lattice Boltzmann equations presented above form a two-way coupled system in the same way as the equations in Section 2.1. Here, this is achieved by using the velocity calculated from the distribution function f_i (Equation 2.57) as the advection velocity in Equation 2.62 in the one way, and through using the temperature-dependent buoyancy force (Equation 2.17) in Equation 2.11 in the other way.

2.3.3 Filtered Lattice Boltzmann Equation

In order to perform LES with the LBM, a spacial filter operation is applied to the lattice Boltzmann equation. Following Malaspinas and Sagaut (2012), the filtered Boltzmann equation can be written as

$$\frac{\partial \overline{f}}{\partial t} + \xi \nabla \overline{f} + \frac{\boldsymbol{F}}{\overline{\rho}} \cdot \nabla_{\xi} \overline{f} = \Omega(\overline{f}) + R, \tag{2.65}$$

where $R = \overline{\Omega(f)} - \Omega(\overline{f})$ represents the subgrid contributions of the collision term. Using the BGK collision operator (Equation 2.32) yields

$$R = \frac{1}{\tau}\left(\overline{f^{eq}} - f^{eq}(\overline{f})\right), \tag{2.66}$$

which can be written using Hermite series

$$R = \frac{\omega(\xi)}{\tau}\sum_{n=0}^{\infty}\frac{1}{n!}\boldsymbol{R}^{(n)}\cdot\boldsymbol{H}^{(n)}(\xi), \tag{2.67}$$

where

$$\boldsymbol{R}^{(n)} = \overline{\boldsymbol{a}^{(n),eq}(\rho,\boldsymbol{u},T)} - \boldsymbol{a}^{(n),eq}(\overline{\rho},\overline{\boldsymbol{u}},\overline{T}). \tag{2.68}$$

Equation 2.65 can also be expressed as a modified BGK collision

$$\frac{\partial\overline{f}}{\partial t} + \xi\nabla\overline{f} + \frac{\boldsymbol{F}}{\overline{\rho}}\cdot\nabla_{\xi}\overline{f} = -\frac{1}{\tau}\left(\overline{f} - f^{eq}(\overline{f})\right) + \frac{1}{\tau}\left(\overline{f^{eq}} - f^{eq}(\overline{f})\right), \tag{2.69}$$

$$= -\frac{1}{\tau_{\text{eff}}}\left(\overline{f} - f^{eq}(\overline{f})\right), \tag{2.70}$$

with

$$\tau_{\text{eff}} = \frac{\tau\left(\overline{f} - f^{eq}(\overline{f})\right)}{\left(\overline{f} - f^{eq}(\overline{f})\right) - \sum_{n=0}^{\infty}\frac{1}{n!}\boldsymbol{R}^{(n)}\cdot\boldsymbol{H}^{(n)}(\xi)}. \tag{2.71}$$

Using Equation 2.45, the coefficients $\boldsymbol{R}^{(n)}$ can be calculated, e.g. up to order $N = 3$,

$$R^{(0)} = 0, \tag{2.72}$$

$$\boldsymbol{R}^{(1)}_{\alpha} = 0, \tag{2.73}$$

$$\boldsymbol{R}^{(2)}_{\alpha\beta} = \overline{\rho\boldsymbol{u}_{\alpha}\boldsymbol{u}_{\beta}} - \overline{\rho}\,\overline{\boldsymbol{u}}_{\alpha}\overline{\boldsymbol{u}}_{\beta} + \left(\overline{\rho T} - \overline{\rho}\,\overline{T}\right)\delta_{\alpha\beta}, \tag{2.74}$$

$$\boldsymbol{R}^{(3)}_{\alpha\beta\gamma} = \overline{\rho\boldsymbol{u}_{\alpha}\boldsymbol{u}_{\beta}\boldsymbol{u}_{\gamma}} - \overline{\rho}\,\overline{\boldsymbol{u}}_{\alpha}\overline{\boldsymbol{u}}_{\beta}\overline{\boldsymbol{u}}_{\gamma} + \delta_{\alpha\beta}\boldsymbol{q}_{\gamma} + \delta_{\alpha\gamma}\boldsymbol{q}_{\beta} + \delta_{\beta\gamma}\boldsymbol{q}_{\alpha}. \tag{2.75}$$

Interestingly, the unclosed terms from the filtered Navier-Stokes equation and from the filtered advection-diffusion equation – respectively $\overline{\rho\boldsymbol{u}_{\alpha}\boldsymbol{u}_{\beta}} - \overline{\rho}\,\overline{\boldsymbol{u}}_{\alpha}\overline{\boldsymbol{u}}_{\beta}$ and $\boldsymbol{q}_{\alpha} = \overline{\rho\boldsymbol{u}_{\alpha}T} - \overline{\rho}\,\overline{\boldsymbol{u}}_{\alpha}\overline{T}$ – appear in the filtered lattice Boltzmann equation as well, see Malaspinas and Sagaut (2012) for the derivation.

This motivates to apply classical closure models. For the case of weakly compressible Navier-Stokes with a truncation at order $N = 2$ the eddy viscosity

assumption (Equation 2.26) is used, so that

$$R^{(0)} = 0, \tag{2.76}$$

$$\boldsymbol{R}_{\alpha}^{(1)} = 0, \tag{2.77}$$

$$\boldsymbol{R}_{\alpha\beta}^{(2)} = -2\nu_{\text{turb}}\overline{\boldsymbol{S}}_{\alpha\beta}. \tag{2.78}$$

The eddy viscosity ν_{turb} is calculated with the standard Smagorinsky model (Equation 2.27) throughout this thesis. The filtered strain rate tensor $\overline{\boldsymbol{S}}$ can be computed from the second moment of the distribution function's non-equilibrium part (Krüger et al. 2010)

$$\overline{\boldsymbol{S}} = \frac{-1}{2c_s^2\overline{\rho}\tau_{\text{eff}}}\int \boldsymbol{\xi}^2\left(\overline{f} - f^{eq}(\overline{f})\right)\mathrm{d}\boldsymbol{\xi}, \tag{2.79}$$

where the effective relaxation time τ_{eff} is given by

$$\nu_{\text{eff}} = \nu + \nu_{\text{turb}} = \left(\tau_{\text{eff}} - \frac{1}{2}\right)c_s^2\Delta t. \tag{2.80}$$

In the case of the advection-diffusion equation with a truncation at order $N = 1$ a modified BGK collision is introduced analogously for the distribution function g resulting in

$$\frac{\partial\overline{g}}{\partial t} + \boldsymbol{\xi}\boldsymbol{\nabla}\overline{g} = -\frac{1}{\tau_{g,\text{eff}}}\left(\overline{g} - g^{eq}(\overline{g})\right) \tag{2.81}$$

with the effective relaxation time $\tau_{g,\text{eff}}$. Here, the eddy diffusivity assumption (Equation 2.29) is used

$$R^{(0)} = 0, \tag{2.82}$$

$$\boldsymbol{R}_{\alpha}^{(1)} = -\boldsymbol{\nabla}\cdot(\alpha_{\text{turb}}\boldsymbol{\nabla}\overline{\phi}), \tag{2.83}$$

where α_{turb} is calculated using Equation 2.30. The scalar gradient can be computed locally from the first moment of the distribution's non-equilibrium part (Chai and T. S. Zhao 2013)

$$\boldsymbol{\nabla}\overline{\phi} = \frac{-1}{c_s^2\overline{\rho}\tau_{g,\text{eff}}}\int \boldsymbol{\xi}\left(\overline{g} - g^{eq}(\overline{g})\right)\mathrm{d}\boldsymbol{\xi}, \tag{2.84}$$

where $\tau_{g,\text{eff}}$ is given by

$$\alpha_{\text{eff}} = \alpha + \alpha_{\text{turb}} = \left(\tau_{g,\text{eff}} - \frac{1}{2}\right)c_s^2\Delta t. \tag{2.85}$$

Since no neighboring cells are accessed, an implementation of the filtered LBM with purely local collision step is enabled. This feature is ideal for high performance parallel implementation of the algorithm which will be demonstrated in the following chapters.

This Section 2.3 is based on the textbooks by Hänel (2004) and Krüger et al. (2017) and on the paper of Malaspinas and Sagaut (2012). For a more in-depth derivation of the equations and more detailed explanations it is recommended to consult these books and the references therein.

3

Application of a Lattice Boltzmann Method combined with a Smagorinsky Turbulence Model to Spatially Resolved Heat Flux inside a Refrigerated Vehicle

In this work the simulation of velocity and temperature distributions inside a refrigerated vehicle is evaluated. For this purpose a 3D double distribution lattice Boltzmann method (LBM) with the Bhatnagar–Gross–Krook (BGK) collision operator is coupled by the buoyancy force calculated with the Boussinesq approximation. This LBM is extended by a Smagorinsky subgrid method, which numerically stabilizes the BGK scheme for low resolutions and high Reynolds and Rayleigh numbers. Besides validation against the two benchmark cases *porous plate* and *natural convection in a square cavity* evaluated at resolutions of $y^+ \approx 2$ for Ra numbers between 10^3 and 10^{10}, the method and its implementation is tested via comparison with experimental data for a refrigerated vehicle at $Re \approx 53\,000$.

The aim of the investigation is to provide a deeper understanding of the refrigerated vehicle's insulation processes including its thermal performance under turbulent flow conditions. Therefore, we extend this method by the half lattice division scheme for conjugate heat transfer to simulate in the geometry of a refrigerated vehicle including its insulation walls. This newly developed

method combination enables us to accurately predict velocity and temperature distributions inside the cooled loading area, while spatially resolving the heat flux through the insulation walls. We simulate the time dependent heating process of the open door test and validate against measurements at four characteristic velocity and 13 temperature positions in the truck.

This chapter corresponds to the work of the same title published in the journal *Computers & Mathematics with Applications* (Gaedtke et al. 2018c). Following the contributor roles taxonomy (Brand et al. 2015), my contribution to this publication includes conceptualization, methodology, software, validation, formal analysis, investigation, data curation, writing – original draft, visualization and project administration.

3.1 Introduction

Global efforts to reduce carbon dioxide emissions as well as prospectively rising prices of fossil fuels lead to continuous development and efficiency improvements of insulation methods. In residential construction, heating energy requirements are progressively minimized by improving building insulation since 1977 (Willems and Skottke 2008). In the sector of refrigerated transports, which usually derive their cooling performance from gas powered refrigeration units in order to maintain the cooling chain of the hauled product, only little attention has been directed to improve efficiency by enhanced insulation. Reasons for this are complex material requirements which, in addition to the insulation, include static stability, load securing as well as resistance against vibrational stress.

According to Smale et al. (2006) most simulations and models for the representation of a velocity and temperature distribution in the field of applied cooling of geometries between 1974 and 2006 have shown low accuracy and large deviations from experimental data. Tapsoba et al. (2007) studied the influence of the k-ϵ turbulence model against the Reynolds stress model, where they indicated the k-ϵ model to fail at the prediction of certain flow characteristics in ventilated enclosures. Ambaw et al. (2013) summarized studies on the cooling of harvested food, indicating some progress being made between 2006 and 2013 with the accuracy of the models. With simulations mainly based on Reynolds averaging turbulence models as the k-ϵ or shear stress transport (SST) model (Delele et al. 2009; Moureh et al. 2009a; Moureh et al. 2009b; Defraeye et al. 2010), he also came to the conclusion, that a clear increase in the accuracy

of turbulent 3D simulations within complex cooled geometries compared with experimental data has still to come.

According to James et al. (2006) first simulations of the open door tests have been carried out by Tso et al. (2002). Tso's simulated temperatures deviate from experimental recordings by up to 4 K at a temperature difference of about 26 K. Ho et al. (2010) showed an approximation to the validation data up to 1.13 K in the simulation of the velocity and temperature distribution in the interior of a filled warehouse, while a very slow velocity and a temperature difference of just 7 K was chosen. Hao and Ju (2011) implemented a constant heat flow over the walls in a cooled container, but no experimental data was analyzed for verification. Akdemir (2015) simulated a cold store and reached a relative error of the temperature of 13 % against the validation data while neglecting heat transfer through the walls.

By considering heat transfer through the walls by particular boundary conditions, Hoang et al. (2015) showed good agreement in the temperature distribution in the simulation of a filled cooling room, but found averaged relative errors for the velocity distribution of partly compassing 50 %. Cardinale et al. (2016) simulated a transport container with a similar method, assuming a constant heat conduction coefficient for the walls and a constant outside temperature of 20 °C, revealing deviations in the temperature distribution of at least 3 K against measurements at temperature differences of about 43 K. A mean relative error of 26 % and 18 % in the prediction of the velocity and temperature fields, respectively, was achieved in the simulation of a cooled shipping container according to Getahun et al. (2017).

In conclusion, this strongly suggests two strategies to increase the accuracy of cooled geometry simulations:

(a) replacement of the Reynolds averaging turbulence model with a large eddy turbulence model and

(b) integration of heat transport through the insulation walls.

Although large eddy simulations (LES) predict flow and temperature fields with higher accuracy, they have not been applied to cooled geometry simulations, yet. This is a consequence of fine computational grids needed for LES, leading to high computational effort and challenging mesh generation. To reduce the increased computational cost of the LES, an efficient and scalable Lattice Boltzmann method is used in this study. In addition, LBM utilizes cartesian grids, which greatly simplifies the mesh generation (Fietz et al. 2012; Henn et

al. 2016). Although (a) might not be absolutely necessary for the geometry and operation setup used in this study, it will be in upcoming studies, where more complex geometries with resolved cargo and spatially different insulation materials are considered. Up to now, modeling of the wall's heat transfer was restricted to spatially constant heat flux boundary conditions. Regarding (b) we show, that resolving the flow field, the refrigerated vehicle's walls and their conjugate heat transfer arrives at much closer accordance to measured data from the open door test.

With its remarkable scalability on parallel computer hardware, the LBM gained attention for turbulent flow simulations, especially in conjunction with LES in the last years (Aidun and Clausen 2010). The first LBM-LES model based on standard Smagorinsky eddy viscosity was proposed by Hou et al. (1994). Teixeira (1998) further discussed incorporation methods for the k-ϵ and RNG turbulence models into the lattice Boltzmann algorithm. Dong et al. (2008) extended Hou's approach by to be inertial range-consistent and later Malaspinas and Sagaut (2012) proposed consistent sub grid closures for the BGK Boltzmann equation.

Studies using Thermal Lattice Boltzmann Method (TLBM) have been carried out on the natural convection in square or cubic enclosures, but only few researchers used applications to show the possibilities in a turbulent regime. Khan et al. (2015) used the lattice Boltzmann method (LBM) and compared it to a CFD-based large eddy simulation, studying the turbulent air flow and temperature field in a four-bed hospital room. At an urban scale, Obrecht et al. (2015) carried out simulations of a small village and the velocity and temperature distributions between single houses. Tiftikci and Kocar (2016) investigated heat distribution inside a 7-pin Indian Prototype Fast Breeder Reactor by LBM simulations, comparing their findings with experimental data. Yuan et al. (2017) used GPU computations on 250 million grid points to examine the thermal comfort of indoor air flows. Most of these authors use the multiple relaxation time (MRT) collision operator for turbulent flows as the BGK collision operator is described as unstable in this flow regime.

In this work, we investigate the employability of the double distribution TLBM to the simulation of a refrigerated vehicle's insulation. For this purpose we examine the BGK-type collision and its extension of a Smagorinsky-type sub grid scale model on up to 2,000 CPU cores. For the first time, we show its proper stability and accuracy in the benchmark case *natural convection in a square cavity* for relaxation times as low as $\tau = 0.5001$ with Ra numbers up to 10^{10}.

This paper is organized in eight sub-sections. The first four present the

governing equations, the turbulence model, applied boundary conditions and the conjugate heat flux method. The following section presents and discusses results of two benchmark cases and shows the model's application to cooling vehicle simulation. A conclusion is given in the final section.

3.2 Mathematical Modeling and Numerical Method

In order to simulate the incompressible air flow within the Boussinesq approximation we apply a double distribution BGK-LBM as described by Krüger et al. (2017). Two different distribution functions – f for momentum and g for temperature – are solved.

3.2.1 Lattice Boltzmann Equations

The Lattice Boltzmann Equation (LBE) including a force term $F_i(x,t)$ is given by

$$f_i(x + c_i\Delta t, t + \Delta t) - f_i(x,t) = \Delta t\left(\Omega_{f,i}(x,t) + F_i(x,t)\right), \tag{3.1}$$

where f_i denotes the discrete probability function and x denotes the space coordinate, t the time coordinate, i the discrete direction and c_i the discrete velocity in direction i. The collision operator $\Omega_i(x,t)$ is given by the Batagnar-Gross-Krook (BGK) operator (Krüger et al. 2017), which is also known as a Single Relaxation Time operator (SRT),

$$\Omega_{f,i}(x,t) = -\frac{1}{\tau_f}\left(f_i(x,t) - f_i^{eq}(x,t)\right). \tag{3.2}$$

In this equation, τ_f represents the relaxation time and f^{eq} the equilibrium distribution given by

$$f_i^{eq}(\rho,u) = w_i\rho\left(1 + \frac{u\cdot c_i}{c_s^2} + \frac{(u\cdot c_i)^2}{2c_s^4} - \frac{u\cdot u}{2c_s^2}\right). \tag{3.3}$$

With w_i denoting the weights of the discrete directions and c_s denoting the speed of sound. The macroscopic density ρ and velocity u are obtained from the distribution function's moments

$$\rho(x,t) = \sum_i f_i(x,t) \text{ and } u = \frac{1}{\rho}\sum_i c_i f_i(x,t) \tag{3.4}$$

Through the Chapman-Enskog analysis, as described e.g. by Krüger et al. (2017), a relationship between viscosity and relaxation time is obtained as

$$\tau_f = \frac{\nu}{c_s^2} + \frac{1}{2}. \tag{3.5}$$

Since in this paper not only the previously described LBE is used for the computation of the isothermal and incompressible fluid properties pressure and velocity, but also for different temperatures, the convection-diffusion-equation is solved as well. Analogous to the LBM for fluid properties, the discrete representation of the convection-diffusion equation in the means of LBM is given as (see e.g. Mohamad 2011)

$$g_i(x + c_i\Delta t, t + \Delta t) - g_i(x,t) = \Delta t \Omega_{g,i}(x,t), \tag{3.6}$$

Equation (3.7) shows the collision operator for the Convection Diffusion Equation (CDE), using the relaxation time τ_g for thermal consideration.

$$\Omega_{g,i}(x,t) = -\frac{1}{\tau_g}\left(g_i(x,t) - g_i^{eq}(x,t)\right) \tag{3.7}$$

The equilibrium distribution is given by

$$g_i^{eq}(x,t) = \frac{\omega_i T}{4}\left(1 + 2\frac{u \cdot c_i}{c_s^2}\right), \tag{3.8}$$

where the macroscopic velocities are obtained from (3.4) and macroscopic temperature T and heat flux q are given by the zeroth and first moment, respectively:

$$T(x,t) = \sum_i g_i(x,t) \text{ and } q(x,t) = \frac{\tau_g - \frac{1}{2}}{\tau_g} \sum_i c_i g_i(x,t) \tag{3.9}$$

A Chapman-Enskog analysis according to Mohamad (2011) again leads to a relation between the relaxation time of the temperature distribution and the fluid's thermal conductivity κ given by

$$\tau_g = \frac{\kappa}{c_s^2} + \frac{1}{2}. \tag{3.10}$$

Discrete velocity directions are used in the LBM. These directions are usually denoted by DdQq, d denoting the velocity space's dimensions and q the discrete directions. Figure 3.1 shows the schematic representation of the D3Q19

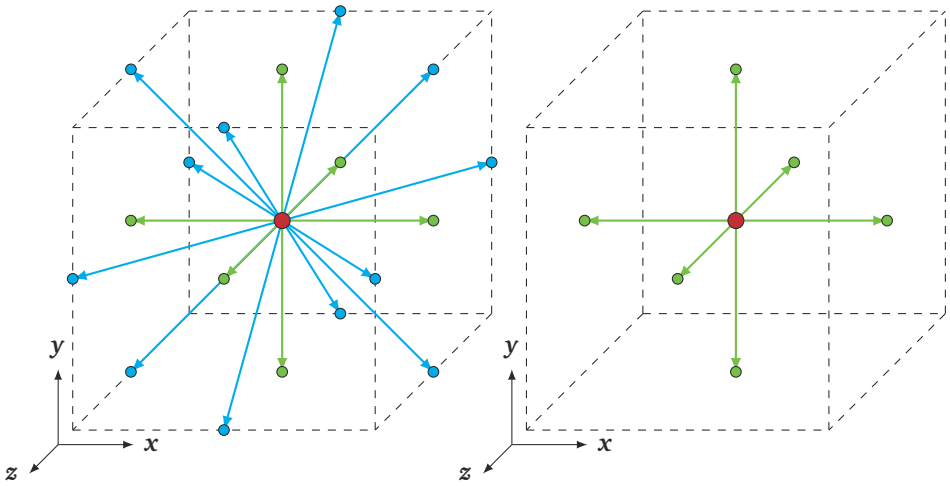

Figure 3.1: *Schematic representation of speed directions according to D3Q19 and D3Q7*

and D3Q7 discrete velocity combinations used for the purpose of this paper. Depending on the direction of motion, predefined weighting factors w_i – distinguished by different colors in Figure 3.1 – is expressed in (3.11) for D3Q19 and in (3.12) for D3Q7. Note that the speed of sound in lattice units is $c_s = \sqrt{\frac{1}{3}}$ in the D3Q19 lattice and $c_s = \sqrt{\frac{1}{4}}$ in the D3Q7 lattice.

$$\text{D3Q19:} \quad w_i = \begin{cases} \frac{12}{36}, & \text{red direction} \\ \frac{2}{36}, & \text{green direction} \\ \frac{1}{36}, & \text{blue direction} \end{cases} \tag{3.11}$$

$$\text{D3Q7:} \quad w_i = \begin{cases} \frac{2}{8}, & \text{red direction} \\ \frac{1}{8}, & \text{green direction} \end{cases} \tag{3.12}$$

To couple the two fields, the force term according to (3.1) is used. The Boussinesq buoyancy force is given by

$$F(x,t) = -\rho_0 \beta g \left(T(x,t) - T_0\right), \tag{3.13}$$

where β denotes the expansion coefficient of the fluid and g the gravitational acceleration. We use the forcing method described by Guo et al. (2002c), where from we obtain the lattice forcing term F_i from F.

Our algorithm combines these two discretized equations for velocity and temperature distributions with coupling via the Boussinesq approximation. This essentially combines a collision step and a streaming step. We

- conduct the stream and collide step in the momentum lattice f with the last time step's force term,
- then collide and stream in the temperature lattice g with the last time step's velocity values.
- Subsequently, we execute the coupling process by updating the momentum lattice's forcing term and
- communicating the macroscopic velocity to the temperature lattice.

So, values from the last time step are used, instead of communicating newly calculated values between the two lattices. Only locally available cell data is accessed during the collision step. This proves to be computationally more efficient.

3.2.2 Smagorinsky Subgrid Scale Model

To efficiently simulate the flow field in the turbulent regime and the flow field's characteristics, we use the Smagorinsky subgrid-scale model (Hou et al. 1994). In this method the effective viscosity ν_{eff} is treated as the sum of molecular ν_0 and eddy viscosity ν_t as

$$\nu_{\text{eff}} = \nu_0 + \nu_t = \nu_0 + (C_S\Delta)^2\sqrt{2\sum_{\alpha,\beta} S_{\alpha\beta}S_{\alpha\beta}}, \tag{3.14}$$

where the strain rate $S_{\alpha\beta}$ is locally computed using the non-equilibrium stress tensor $\Pi^{(neq)}_{\alpha,\beta}$ by

$$S_{\alpha\beta} = -\frac{1}{2\rho\tau^* c_s^2}\Pi^{(neq)}_{\alpha,\beta} = -\frac{1}{2\rho\tau^* c_s^2}\sum_q e_{i,\alpha}e_{i,\beta}(f_i - f_i^{(eq)}). \tag{3.15}$$

With $\tau^* = \frac{\nu_{\text{eff}}}{c_s^2} + \frac{1}{2}$ is denoting the modified relaxation time as a function of ν_{eff}.

Analogous to the calculation of ν_{eff}, the effective thermal diffusivity is calculated by

$$\alpha_{\text{eff}} = \alpha_0 + \alpha_t = \alpha_0 + \frac{\nu_t}{Pr_t}, \tag{3.16}$$

where the turbulent thermal diffusivity α_t is calculated by the turbulent Prandtl number

$$Pr_t = \frac{\nu_t}{\alpha_t}. \tag{3.17}$$

Although this approach is broadly used in simulations and described in the literature (Fröhlich 2006), there is up to now no consent on how to chose Pr_t correctly, as values vary from 0.3 in experiments to 0.86 derived theoretically up to 1.0 and even larger in some regions close to the wall in DNS simulations (Schlichting et al. 1955; Treeck et al. 2006; Dharmarathne et al. 2016). We state the applicability of this approach and accuracy in combination with our SRT-LBM and with a fixed $Pr_t = 0.86$ in Section 3.3.1.2 by comparing results from the well known benchmark case for natural convection in a square cavity against values from the literature.

3.2.3 Boundary Conditions

For pressure and velocity boundary conditions, we use the regularized boundary approach as described by Latt et al. (2008). The Dirichlet-type temperature boundary condition is implemented as described by Krüger et al. (2017) and the Neumann-type boundary for temperature is used as recommended by Junk and Z. Yang (2008). Simple bounce back (Succi 2001b) is used for no-slip and adiabatic boundaries.

3.2.4 Conjugate Heat Transfer

To simulate heat transfer between a solid material and a fluid streaming around it, we use the half lattice division scheme described by J. Wang et al. (2007). The diffusion equation for the solid's temperature distribution and the convection-diffusion-equation for the fluid's temperature distribution are solved on a single mesh. Different temperature conductivities are taken into account through space variant relaxation times $\tau_{g,solid}$ and $\tau_{g,fluid}$. This approach is valid in a strictly sense only for steady state problems and $\rho_{solid} c_{p,solid} = \rho_{fluid} c_{p,fluid}$, where ρ denotes the density and c_p denotes the specific heat capacity. By choosing the lattice units as $\rho^*_{fluid} = 1$ and $\rho^*_{solid} = \rho^*_{fluid} \frac{c_{p,fluid}}{c_{p,solid}}$ the latter condition is fulfilled.

3.3 Results and Discussion

In this section we show results for two benchmark cases, where we compare results from our present model to analytic solution and literature results, respectively. Subsequently, the model is applied to the simulation of a refrigerated vehicle. All simulations are conducted in the open source software pack-

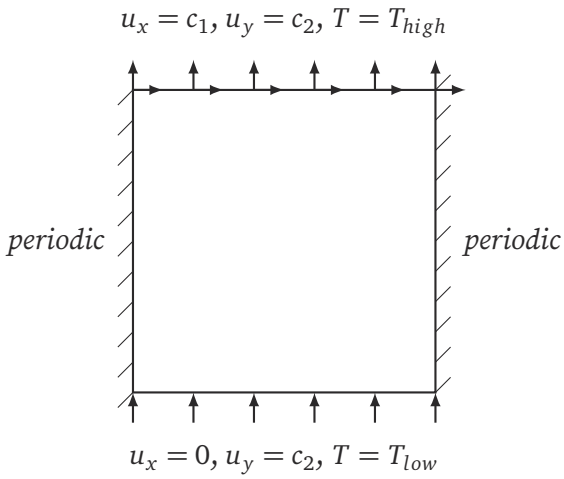

Figure 3.2: *Schematic representation of the simulation setup of the porous plate problem including it's boundary conditions*

age OpenLB (Heuveline and Krause 2011, openlb.net). The LBM for the flow field including the Smagorinsky sub grid model and the LBM for the temperature field are implemented and extend by the Smagorinsky sub grid model for the temperature. Due to its generic approach based on C++ templates, OpenLB has been used for several applications in math, engineering and medicine (see for example Krause et al. 2011; Krause et al. 2013; Henn et al. 2016; Mink et al. 2016; Trunk et al. 2016).

3.3.1 Benchmarks

3.3.1.1 Porous Plate Problem

To verify the present model's grid convergence for different lattice relaxation times τ_f and τ_g, we conduct simulations of the porous plate problem (Guo et al. 2002a; Peng et al. 2003), which – to the knowledge of the authors – has not been done before with a 3D LBM. The porous plate problem describes a channel flow, where the upper cool plate moves with a constant velocity and through the bottom warm plate a constant normal flow is injected and withdrawn at the same rate at the upper plate. At the left and right hand side as well as at the front and the back of the domain, periodic boundary conditions are applied. Constant velocity and temperature boundary conditions are applied to the top and bottom plates according to Figure 3.2.

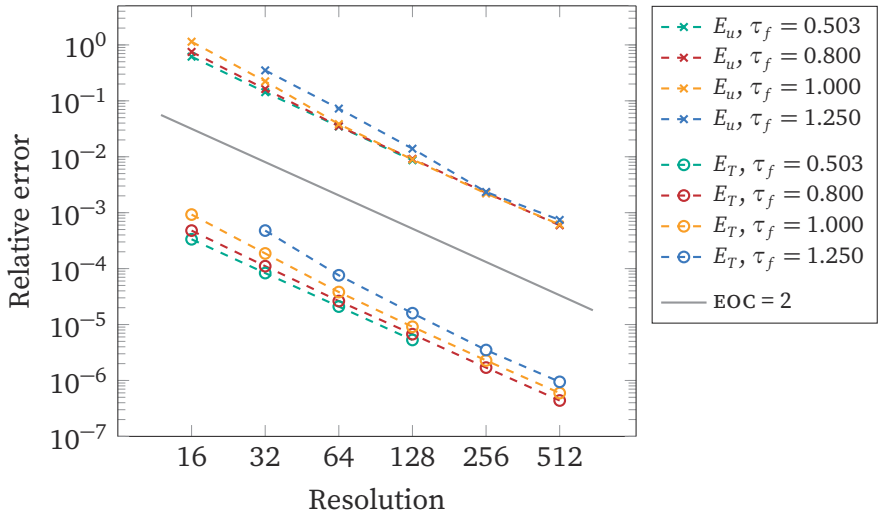

Figure 3.3: *Relative error for velocity E_u and temperature E_T plotted logarithmically over the resolution: Negative slope of about two shows the method's second order accuracy.*

An analytic solution for this steady state problem is given for the velocity and temperature distributions by Guo et al. (2002a):

$$u_x(y) = u_{x,0}\left(\frac{e^{Re\cdot y/L} - 1}{e^{Re} - 1}\right) \tag{3.18}$$

$$T(y) = T_0 + \Delta T = \left(\frac{e^{Pr\cdot Re\cdot y/L} - 1}{e^{Pr\cdot Re} - 1}\right) \tag{3.19}$$

Where $u_{x,0}$ denotes the upper plate's velocity, $Re = \frac{u_{y,0}L}{\nu}$ the Reynolds number depending on the injected velocity $u_{y,0}$, the fluid's viscosity ν and the channel length L and $Pr = \frac{\nu}{\alpha}$ the Prandtl number. The temperature difference between the hot and cold plate is given by $\Delta T = T_h - T_c$. For the grid independence study, we choose $Re = 5$, $Pr = 0.71$ and Rayleigh number $Ra = \frac{g\beta}{\nu\alpha}\Delta T L^3 = 100$. The relaxation time is varied as $\tau = 1.2$, 1.0, 0.8 and 0.503 and resolution is varied as the number of grid cells in x and y direction $N = 16$, 32, 64, 128 and 256.

Relative global errors in temperature and velocity fields are shown logarithmically in Figure 3.3 with the relative global error defined by

$$E_\phi = \frac{\sqrt{\Delta x^3 \sum_x |\phi(x) - \phi_a(x)|^2}}{\sqrt{\Delta x^3 \sum |\phi_a(x)|^2}}, \tag{3.20}$$

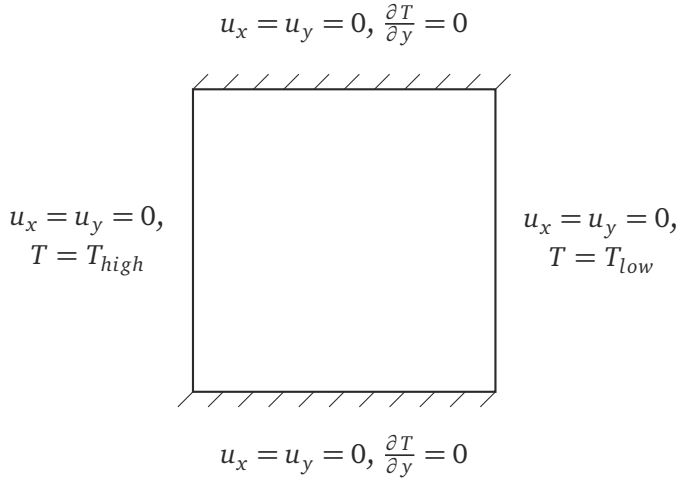

Figure 3.4: *Schematic representation of the simulation domain for the natural convection in a square cavity including it's boundary conditions.*

where summation goes over the entire flow domain, ϕ denotes the quantity of interest, either the velocity or the temperature, and ϕ_a is the analytic solution given by (3.18) and (3.19).

Figure 3.3 shows clearly that this three dimensional model and it's present implementation is of second order in space for both velocity and temperature. It is shown, that the double distribution BGK scheme is accurate for several values of τ_f and is stable for values as low as $\tau_f = 0.503$.

3.3.1.2 Natural Convection in a Square Cavity

To obtain evidence for the turbulence modeling approach and implementation the principle of static buoyancy is used within a square cavity, which has been numerically studied by many authors (De Vahl Davis 1983; Markatos 1983; Dixit and Babu 2006). In this case, air in a three-dimensional cavity with different, but constant temperatures on the vertical walls is simulated. The horizontal walls of the geometry are considered adiabatic as shown in Figure 3.4. In z direction the domain is three grid points deep and considered periodic.

Since the walls of the cavity are considered to be fluid-impermeable regions, the illustrated edges obtain the no-slip condition. The initial velocity in the entire cavity is set to $u = 0$. The parameters of air were obtained from Hortmann et al. (1990) and are shown in Table 3.1.

Table 3.1: *Properties of air from Hortmann et al. (1990) used for the validation of the natural convection in a cavity.*

Properties of air	
λ	$2.5684 \times 10^{-2}\,\mathrm{W/(m\,K)}$
ν	$1.5126 \times 10^{-5}\,\mathrm{m^2/s}$
ρ	$1.19\,\mathrm{kg/m^3}$
β	$3.41 \times 10^{-3}\,\mathrm{1/K}$
c_p	$1.013\,09 \times 10^{3}\,\mathrm{J/(kg\,K)}$

The natural convection developing within the cavity is analyzed for different Rayleigh numbers of $Ra = 10^3$, 10^4, 10^5 and 10^6 for the laminar regime and $Ra = 10^7$, 10^8, 10^9 and 10^{10} for the turbulent regime by means of the following quantities:

- the maximum vertical velocity $u_{x,max}$ on the horizontal mid-plane of the cavity and its position y_{max},
- the maximum horizontal velocity $u_{y,max}$ on the vertical mid-plane of the cavity and its position x_{max},
- the average Nusselt number $\overline{\mathrm{Nu}}_0$ on the boundary of the cavity at $x = 0$.

For the laminar cases up to $Ra = 10^6$ we chose the lattice Mach number as $Ma = \frac{u_{max}}{c_s} = 0.1$, where u_{max} is the expected maximum velocity from the literature results and we chose the respective resolutions as shown in Table 3.2. Convergence is assumed, when the relative standard deviation of five following Ra numbers calculated each 1000 time steps is below $\epsilon = 10^{-5}$. Table 3.2 shows the results of the present scheme as well as the relative errors against the values of De Vahl Davis (1983), which have already been considered by various authors as a comparative solution using different numerical methods.

To visualize the flow inside the cavity and the resulting differences for the simulated Rayleigh numbers, streamlines and isotherms are shown in Figures 3.5 and 3.6. The vortex at the middle, which develops with a Rayleigh number of $Ra = 10^3$, can be seen clearly and is based on buoyancy of heated and sinking of cold air. On account of the temperature differences of the two walls, a Rayleigh number of $Ra = 10^3$ results in the displacement of the mean vertical isotherms, where the temperature gradients are approaching further into the direction of the vertical walls. As the Rayleigh number increases, the vortex at the middle

Table 3.2: *Obtained values by simulating the natural convection in a square cavity geometry for different Rayleigh numbers and the results of De Vahl Davis (1983).*

Ra Grid used		10^3 (64x64x3)	10^4 (128x128x3)	10^5 (256x256x3)	10^6 (512x512x3)
y_{max}	De Vahl Davis 1983	0.813	0.823	0.855	0.850
	Present	0.828	0.828	0.859	0.852
$u_{x,max}$	De Vahl Davis 1983	3.649	16.178	34.730	64.630
	Present	3.500	16.210	34.792	64.957
x_{max}	De Vahl Davis 1983	0.178	0.119	0.066	0.038
	Present	0.172	0.125	0.063	0.039
$u_{y,max}$	De Vahl Davis 1983	3.697	19.617	68.590	219.360
	Present	3.760	19.438	68.413	219.537
$\overline{\mathrm{Nu}_0}$	De Vahl Davis 1983	1.117	2.238	4.509	8.817
	Present	1.116	2.216	4.503	8.772

changes into an ellipse shape and from a Rayleigh number of $Ra = 10^5$ finally divides into two partial vortices, which drift horizontally in the direction of the adiabatic walls.

Beginning with a Rayleigh number of $Ra = 10^5$, the isotherms are found to be approximately horizontal to the cavity geometry, limiting fluid movement in the vertical direction. The main heat exchange is now effected only by convection in the region of the edges, with high temperature gradients and subsequently high acceleration in the fluid. At a Rayleigh number of $Ra = 10^6$, the displacement of the partial vortices occurs in the corners of the cavity, whereupon a third vortex is formed in the middle, which also rotates clockwise. The velocity and temperature fields compare very well with the illustrations in the literature by De Vahl Davis (1983), Guo et al. (2002a), and Peng et al. (2003).

For the turbulent cases from $Ra = 10^7$ to 10^{10} we use the Double Smagorinsky Subgrid Scaling Method (DSSSM) as described in Section 3.2.2. Again, we choose the lattice Mach number to be $Ma = 0.1$ for all cases and a convergence residuum of $\epsilon = 10^{-3}$. To further assure a reasonable fine mesh for the large and medium large eddies to be resolved, we introduce a dimensionless wall spacing y^+ (White 2003) with

$$y^+ = \frac{\Delta x u_\tau}{\nu}, \tag{3.21}$$

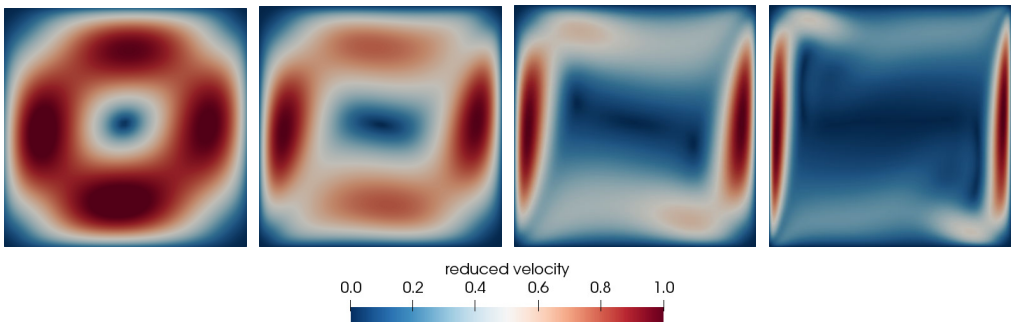

Figure 3.5: *Converged velocity distributions for the natural convection in a square cavity with Rayleigh numbers $Ra = 10^3$, 10^4, 10^5 and 10^6 (left to right) colored analogous to the dimensionless velocity magnitude: red indicates high, blue indicates low*

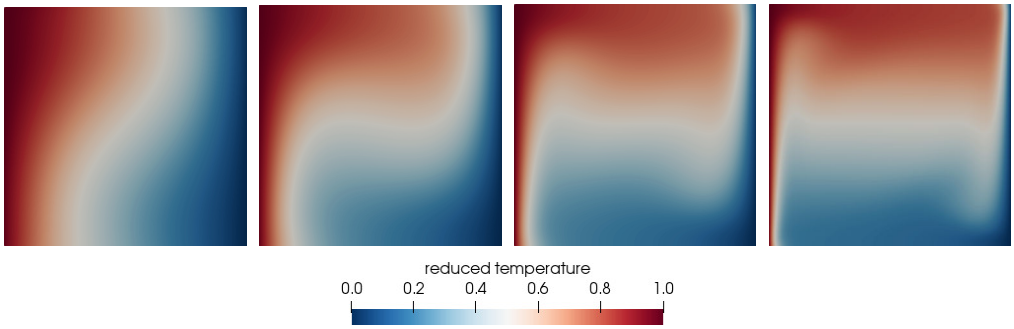

Figure 3.6: *Converged temperature distributions for the natural convection in a square cavity with Rayleigh numbers $Ra = 10^3$, 10^4, 10^5 and 10^6 (left to right) colored analogous to the dimensionless temperature: red indicates high, blue indicates low*

Table 3.3: *Simulated values of turbulent cases of natural convection in a square cavity geometry for different Rayleigh numbers and the results of Markatos (1983), Le Quéré (1991), and Dixit and Babu (2006).*

Ra Grid used		10^7 (47x47x3)	10^8 (139x139x3)	10^9 (392x392x3)	10^{10} (1138x1138x3)
y_{max}	Markatos 1983	-	0.941	-	0.9625
	Le Quéré 1991	0.879	0.928	-	-
	Dixit and Babu 2006	0.851	0.937	0.966	0.9402
	Present	0.905	0.945	0.950	0.907
$u_{x,max}$	Markatos 1983	-	514.3	-	2323
	Le Quéré 1991	148.58	321.9	-	-
	Dixit and Babu 2006	164.236	389.877	503.24	2323
	Present	130.221	280.674	2277.140	2967.5
x_{max}	Markatos 1983	-	0.0135	-	0.0055
	Le Quéré 1991	0.021	0.012	-	-
	Dixit and Babu 2006	0.020	0.0112	0.0064	0.4907
	Present	0.042	0.014	0.008	0.004
$u_{y,max}$	Markatos 1983	-	1812	-	21463
	Le Quéré 1991	699.236	2222.39	-	-
	Dixit and Babu 2006	701.922	2241.374	6820.07	21463
	Present	467.976	1860.270	6124.420	20533
$\overline{\mathrm{Nu}_0}$	Markatos 1983	-	32.045	-	156.85
	Le Quéré 1991	16.523	30.225	-	-
	Dixit and Babu 2006	16.79	30.506	57.350	103.663
	Present	16.987	32.076	52.260	102.034

where

$$u_\tau = u_{max}\sqrt{\frac{0.026}{2}\left(\frac{\nu}{u_{max}d_{wall}}\right)} \tag{3.22}$$

denotes the friction velocity. Here, d_{wall} is the distance from the position of the maximum velocity to the wall. Table 3.3 compares the results of the present model against values from Markatos (1983), Le Quéré (1991), and Dixit and Babu (2006) for $y^+ = 2$.

As turbulence is a chaotic state, the calculated values are time dependent and relative deviation is not necessarily a miscalculation itself. Within this constraint, the present model obtains values very close to those from comparative

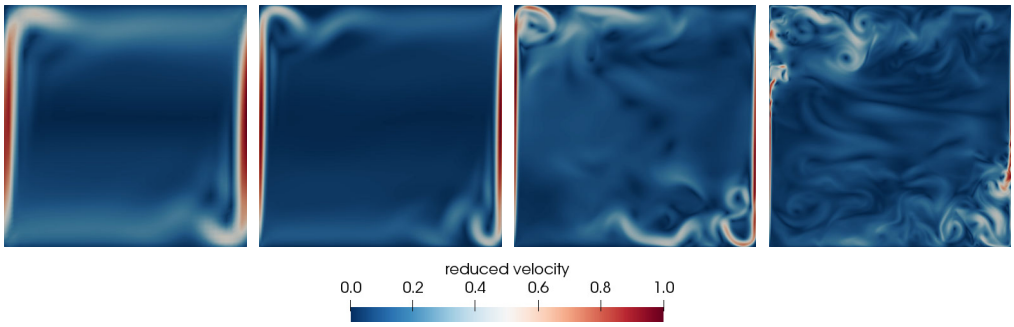

Figure 3.7: *Instantaneous velocity distributions for the natural convection in a square cavity with Rayleigh numbers $Ra = 10^7$, 10^8, 10^9 and 10^{10} (left to right) colored analogous to the dimensionless velocity magnitude: red indicates high, blue indicates low*

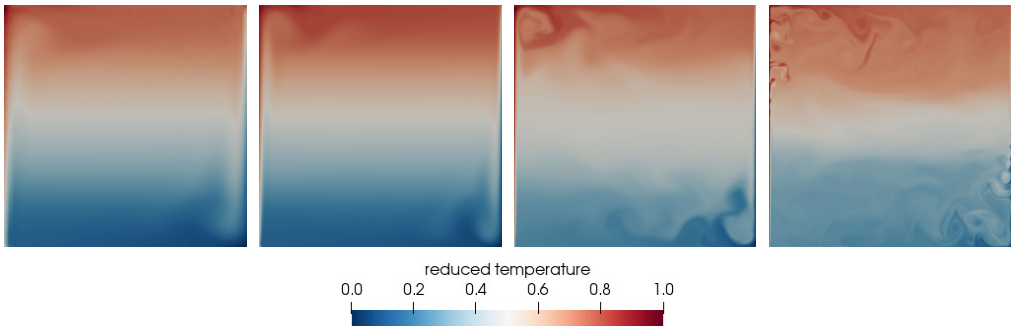

Figure 3.8: *Instantaneous temperature distributions for the natural convection in a square cavity with Rayleigh numbers $Ra = 10^7$, 10^8, 10^9 and 10^{10} (left to right) colored analogous to the dimensionless temperature: red indicates high, blue indicates low*

studies, especially for the relatively small resolutions used here. Maximum velocities' deviations are occurring close to the cavities' walls. Implementing a turbulent wall boundary condition could surely achieve closer results. Such a boundary condition for the turbulent temperature boundary layer is not yet incorporated in the LBM and is subject to the author's subsequent publication. The instantaneous velocity and temperature fields in Figures 3.7 and 3.8 compare very well against the illustrations in the literature by Dixit and Babu (2006), although he used time averaged values for his visualizations.

3.3.2 Application to Refrigerated Vehicles

The validation of a realistic mapping of flow and the temperature distributions in the interior of a refrigerated transport structure is of crucial importance for simulations of various wall structures and loading cases. Hence, high priority is attributed to the validation of the cooling construction and an experimental measurement is carried out for a verification of the results of the simulation. Section 3.3.2.1 shows the design of the geometry of the structure for measurements of air speed and temperature values, as well as the transferred and implemented geometry within which the simulation is to take place. The comparison between experimental data and the corresponding simulation of the speed and temperature fields is given in Section 3.3.2.2.

3.3.2.1 Simulation and Measurement Set-up

The geometry models a CoolerBox 2.0 TK 3500 HS refrigerated transporter of the company *Kress Fahrzeug GmbH* with a two-winged door. This transporter uses a Carrier Xarios 500T cooling unit, which can be used for both heating and cooling purposes. The energy supply of the transport cooling system can be provided either by means of the diesel engine of the vehicle during journeys, or by 400 V three-phase current during longer periods of rest. The manufacturer's specifications for the cooling system state a full-load volume flow of $\dot{V} = 990\,\mathrm{m}^3/\mathrm{h}$ and a heating and cooling capacity of $\dot{Q} = 950\,\mathrm{W}$. This full-load volume flow results in a maximum inlet velocity of $u_{\mathrm{inlet}} = 5.587\,\mathrm{m/s}$ and a corresponding Reynolds number of $Re = \frac{u_{\mathrm{inlet}} d_h}{\nu} = 52\,959$ with the hydraulic diameter $d_h = 0.1115\,\mathrm{m}$. Dimensions of the overall structure and the air conditioner with air inflow and outflow are given in Figure 3.9.

To simulate in this geometry, we choose a resolution of 253.8 millions cells and a maximum lattice velocity $u^* = 0.1$. We use OpenLB's OpenMPI-based domain decomposition method (Fietz et al. 2012) to efficiently parallelize to a total number of 2000 CPU cores achieving approximately 3200 mega lattice updates per second (MLUPs) for the present coupled model.

To determine the temporal temperature distribution, 13 temperature measuring devices were installed in the cooler construction according to Figure 3.9 plus one temperature measuring device underneath the cooling transporter to determine the ambient temperature. The velocity distribution of the air flow was recorded at four characteristic measuring points using a hand held anemometer with the vehicle's built-in air conditioner working at full power.

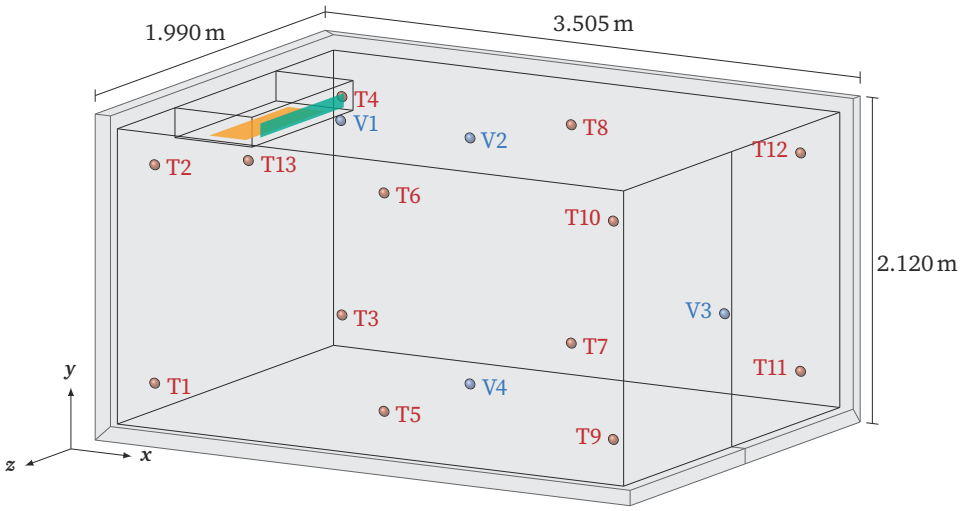

Figure 3.9: *Schematic representation of the cooling system and the built-in air conditioning system with registered speed (blue) and temperature measuring points (red), as well as their numbering. The air conditioning's outlet and suction side are shown in green and orange, respectively.*

In the simulation, these velocity and temperature measuring points were realized, analogously to Figure 3.9, through spheres with a diameter of $d_{mp} = 0.05\,\text{m}$, within which the simulated quantities were spatially averaged.

All parameters used for the description of flowing air as well as insulation used are listed in Table 3.4. It should be noted that the insulation is a three-layer structure consisting of two layers of glass-fiber-reinforced plastic sheets and a polyurethane hard foam layer with glass fibre admixture. The corresponding mean values of the simulated wall structure are shown in Table 3.4, as well.

Since only parameters relating to the cooling capacity and the volume flows at full load can readily be taken from the parameters of the air-conditioning system, a door test, whose experimental sequence is explained in more detail in the following section, is used as a validation case for the cooling construction.

3.3.2.2 Comparison with Open Door Test Measurements

In a door test, the rear door of the cooling compartment is opened for two minutes in order to effect an air exchange with the surroundings, following the closing of the door and the start of the air conditioning system. This is a frequent application when delivering refrigerated goods or when loading and

Table 3.4: *Used properties for air from the literature according to* VDI-*Wärmeatlas, as well as the data of the insulation, geometry and required numerical parameters*

Properties of air		Properties of insulation	
λ	$2.262 \times 10^{-2}\,\mathrm{W/(m\,K)}$	λ	$2.3 \times 10^{-2}\,\mathrm{W/(m\,K)}$
ρ	$1.3782\,\mathrm{kg/m^3}$	ρ	$3.950 \times 10^{1}\,\mathrm{kg/m^3}$
c_p	$1.0068 \times 10^{3}\,\mathrm{J/(kg\,K)}$	c_p	$1.400 \times 10^{3}\,\mathrm{J\,K/kg}$
β	$3.974 \times 10^{-3}\,1/\mathrm{K}$		
ν	$1.1766 \times 10^{-5}\,\mathrm{m^2/s}$		

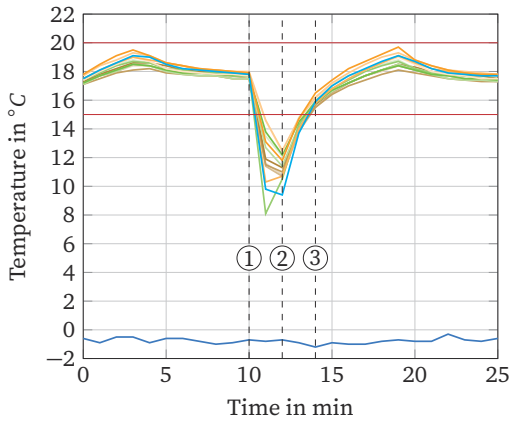

Figure 3.10: *Measurements of the refrigerated vehicle's temperatures during the heating operation with winter outside conditions. The door test with its individual phases and 13 temperature measuring points is shown. Higher and lower acceptance limits are displayed in red and the outside temperature is displayed in blue.*

unloading a refrigerated transporter. Figure 3.10 shows the temperature time measurements of the aforementioned thermocouples during a door test with the opening of the door at position 1, the closing of the door and the start of the air conditioning system at position 2. Since the air conditioner determines a temperature below the chosen acceptance limit by means of a sensor, it starts the heating of the indoor space under full power. After 2 minutes, at position 3, a temperature above the acceptance limit is reached and the air conditioning changes back to the cyclical mode.

The described sequence starting at position 2 for a time of one minute is simulated using the previously presented geometry and is used as a validation case. For this purpose, a polynomial approach profile to the maximum speed

and a plug-flow profile in the outlet, due to an upstream lattice in the real device, is implemented. The heating output is coupled into the system via an energy balance, whereby the volumetric flow into the device, its density and temperature are determined from the moments (3.4) and (3.9), and the new outlet temperature is calculated from these values with the values of the outlet volume flow, the density and the predetermined heating output. The specific heat capacity of air is assumed to be constant due to the low temperature dependence in the required range.

After one simulated minute, the results of the simulation are output from the individual implemented measuring spheres for speed and temperature and compared with the results of the experimental measurements. Figure 3.11 shows streamline representations of the flow induced by the air conditioner (AC). The air streams out of the AC parallel to the ceiling. After hitting the back wall it is spread along the wall and directed downwards. From the vehicle's floor it is sucked into the AC again. Figure 3.12 shows the velocity and the temperature fields of the simulated refrigerated vehicle.

The listed results for the individual measuring regions of the experimental measurements, the validation simulation and their absolute errors are given in Table 3.5. With absolute errors of below 0.4 m/s for the velocities and below 1 K for the temperatures these are very good agreement with our measurements. Other simulations (e.g. Tso et al. 2002; Hoang et al. 2015; Cardinale et al. 2016) have found differences up to 50 % for the velocities and between 3 K and 4 K for the temperatures in very similar geometries and measurement setups. This shows the advantage of the used method: By resolving a larger part of the turbulent energy spectrum compared to k-ϵ turbulent models and by spatially resolving the walls heat flux instead of modeling it as constant heat flux boundary conditions, better agreement between measurements and simulation data is achieved.

Although, considering the high computation time and hardware requirements for following simulations, incorporating a turbulent wall function into the method could allow lower resolutions while maintaining high accuracy. Turbulent wall functions for the TLBM have not yet been shown in the literature.

3.3.2.3 Heat Flux through Insulation Walls

An important measurement in order to optimize cooling efficiency of a refrigerated vehicle is the conductive heat flux through the insulation walls. By re-

Figure 3.11: *Streamline representation of the simulated air flow inside the refrigerated vehicle.*

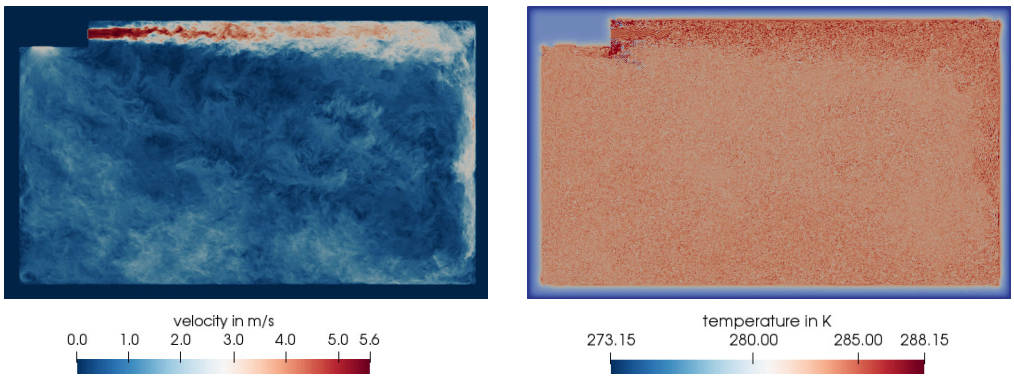

Figure 3.12: *Velocity and temperature field in x-y-plane at $z = 0.995\,\mathrm{m}$ of the simulated air and the insulated walls.*

Table 3.5: *Experimental measurements and simulated results of the velocity and temperature recordings in the cooling stage after $t = 0\,\mathrm{s}$ and $60\,\mathrm{s}$ including absolute deviations for $t = 60\,\mathrm{s}$.*

	measurement		simulation		deviation
time in s	0	60	0	60	60
V1 in m/s	0	5.0 ± 0.2	0	4.92	0.08
V2 in m/s	0	4.3 ± 0.2	0	3.94	0.36
V3 in m/s	0	2.2 ± 0.2	0	2.17	0.03
V4 in m/s	0	1.3 ± 0.2	0	1.22	0.08
T1 in K	283.95 ± 0.20	286.95 ± 0.30	284.45	287.38	0.43
T2 in K	283.85 ± 0.20	286.95 ± 0.30	284.45	287.03	0.08
T3 in K	284.15 ± 0.20	287.15 ± 0.30	284.45	287.19	0.04
T4 in K	284.45 ± 0.20	287.25 ± 0.30	284.45	286.93	0.32
T5 in K	285.25 ± 0.20	287.95 ± 0.30	284.45	287.76	0.19
T6 in K	284.55 ± 0.20	287.35 ± 0.30	284.45	287.31	0.04
T7 in K	283.65 ± 0.20	287.45 ± 0.30	284.45	287.49	0.04
T8 in K	285.35 ± 0.20	287.65 ± 0.30	284.45	286.99	0.66
T9 in K	285.55 ± 0.20	287.85 ± 0.30	284.45	288.33	0.48
T10 in K	285.65 ± 0.20	287.85 ± 0.30	284.45	288.68	0.83
T11 in K	283.85 ± 0.20	287.15 ± 0.30	284.45	288.09	0.94
T12 in K	284.95 ± 0.20	287.85 ± 0.30	284.45	287.99	0.14
T13 in K	282.55 ± 0.20	286.85 ± 0.30	284.45	287.28	0.43

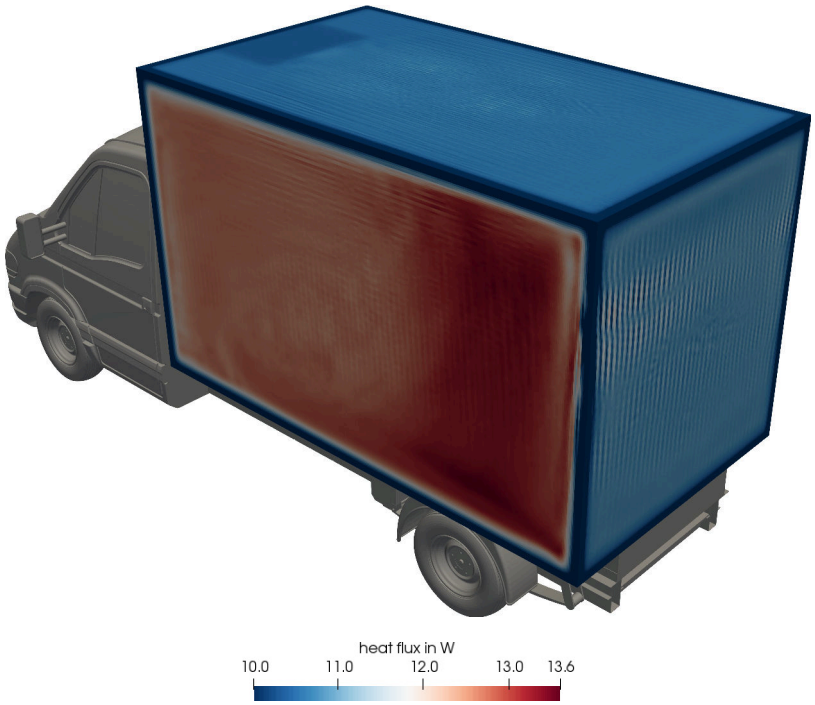

Figure 3.13: *Heat flux through the insulation of the refrigerated vehicle*

solving the insulation walls as a structure of specific materials in our simulations, we are able to calculate the spacial heat transfer in normal direction through the walls for every grid point. Figure 3.13 shows the heat influx in the outermost plane of the insulation walls. Note, that we make the assumption of quasi steady state heat transfer through the insulation walls.

High differences between the edges of the refrigerated body with $\dot{Q} = 0\,\mathrm{W}$ to $4\,\mathrm{W}$ and the walls with $\dot{Q} = 10\,\mathrm{W}$ to $13.6\,\mathrm{W}$ are recognized. Additionally, the wall thickness' influence can be seen as the thinner side walls induce a higher heat flow compared to the thicker ceiling, front and back side.

With Nusselt correlations taken from the VDI-Wärmeatlas, an expected value is calculated in order to obtain an estimation of the incoming heat flow of this insulation concept. For this purpose, the correlation for the overflow of planar plates is used for the interior space on all internal walls separately and averagely. For each wall, a specific Reynolds number is calculated using the experimentally determined velocities from the validation, a laminar Nusselt number according to (3.23), as well as a turbulent Nusselt number according

to (3.24).

$$\mathrm{Nu}_{lam} = \left(\frac{2}{1 + 22 \cdot \frac{\nu \cdot \rho \cdot c_p}{\lambda}} \right)^{\frac{1}{6}} \cdot \sqrt{\mathrm{Re} \cdot \frac{\nu \cdot \rho \cdot c_p}{\lambda}} \tag{3.23}$$

$$\mathrm{Nu}_{turb} = \frac{0.037 \cdot \mathrm{Re}^{0.8} \cdot \frac{\nu \cdot \rho \cdot c_p}{\lambda}}{1 + 2.443 \cdot \mathrm{Re}^{-0.1} \cdot \left(\left(\frac{\nu \cdot \rho \cdot c_p}{\lambda} \right)^{\frac{2}{3}} - 1 \right)} \tag{3.24}$$

$$\mathrm{Nu} = \sqrt{\mathrm{Nu}_{lam}^2 + \mathrm{Nu}_{turb}^2} \tag{3.25}$$

With the help of the wall-specific heat transfer coefficients, an insulation $k_{\mathrm{PUR}} = 0.275\,\mathrm{W/(m^2\,K)}$ for pure hard foam can be obtained, so for a temperature difference of $\Delta T = 50\,\mathrm{K}$. A total incoming heat flow of $\dot{Q}_{\mathrm{PUR}} = 479\,\mathrm{W}$ is determined. The simulated heat influx through the walls sums up to a value of $\dot{Q}_{\mathrm{PUR}} = 458\,\mathrm{W}$ and thus shows a relative deviation from the Nusselt correlation of only 4.38 %. The simulation arrives within the deviation of the Nusselt correlation, which has a general discrepancy due to the semi-empirical determination by measured values.

With the method shown, in contrast to averaged total heat currents, spatially resolved heat flows can be determined, which can be used as a valuable basis for customized insulation optimization at positions of higher heat flow.

3.4 Conclusions

In this paper, we extend a double distribution BGK-based LBM by the Smagorinsky turbulence model for both velocity and temperature distribution functions. This method is found stable for a coarse discretization ($\tau \approx 0.5001$) with high Re and Ra numbers and accurate for the turbulent natural convection in a square cavity with $Ra \leq 10^{10}$. Due to the relatively small resolutions of $y^+ \approx 2$ used here, the boundary layer is not completely resolved. Therefore, a turbulent wall function implementation should further improve the accuracy of the model for wall bounded turbulence, which will be inspected in a planned publication.

Simulation of the flow field and heat transfer within a given cooling truck shows very good agreement with measurement results. By resolving the truck's insulation walls in a conjugate heat transfer model, the model is able to predict the heat flux through the walls close to Nusselt correlations, but spatially resolved. This allows new insights to the refrigerated vehicle's heat transfer,

which is essential for the optimization process of the wall materials and structures considering economic conditions.

Therefore we conclude this simulation model as beeing able to accurately describe the insulation effect in a refrigerated vehicle with turbulent cold air flows including spatially resolved heat flux through the vehicle's walls.

4

Flow and Heat Transfer Simulation with a Thermal Large Eddy Lattice Boltzmann Method in an Annular Gap with an Inner Rotating Cylinder

In this study, a thermal Large Eddy Lattice Boltzmann Method (LBM-LES) is applied to Taylor-Couette flow simulations, allowing detailed analysis of local heat transport over a wide range of Taylor numbers, including resolved transient Taylor vortices.

The challenge in thermal management of electric motors is to control the temperature in the air gap between rotor and stator due to the gap's small width and complex geometry, in which Taylor vortices strongly influence the heat transfer. This thin gap – here simplified by an annulus – is solved for the first time by a Thermal Lattice Boltzmann Method with a Smagorinsky sub-grid model. The influence of the rotational velocity of the inner cylinder with Taylor numbers from 36 to 511 – corresponding to a Reynolds number on the inner cylinder of up to 126,000 – is numerically investigated.

The simulations are validated on basis of the global Nusselt number, where we find good agreement with a published measurement series, an empirical correlation and Finite Volume simulations using the SST turbulence model. Special attention is paid on predicting the critical Taylor number,

which is reproduced almost exactly by Direct Numerical Simulations (DNS) with LBM, whereas LBM-LES slightly overestimates and the SST model further overestimates the occurrence of Taylor vortices.

This chapter corresponds to the work of the same title published in the journal *International Journal of Modern Physics C* (Gaedtke et al. 2019a). Following the contributor roles taxonomy (Brand et al. 2015), my contribution to this publication includes conceptualization, methodology, software, validation, investigation, data curation, writing – original draft and visualization.

4.1 Introduction

The temperature behavior of rotating electric machines, for example electric motors or generators, is of great interest. With their application to energy conversion from electric to rotational energy or vice versa, a lot of industries are looking for efficient devices, in particular with the impending energy revolution constantly asking for higher efficiency. If one knows the exact temperature distribution in an electric machine, detailed statements on the operating behavior can be made. This knowledge can then contribute to improved designs for these machines by preventing individual components overheating or increasing overall electric efficiency. By now, internal temperature distributions in rotating electric machines are not fully understood and often approximated from empirical global heat flux correlations. Providing detailed flow and heat transfer insights will therefore help design more efficient electric machines.

One domain of particular interest is the space between rotor and stator of the electrical machine, which is called air gap and can be depicted approximately as an annulus. Thermal management in this gap is challenging as many geometrical influences, materials and mechanisms of heat transfer have to be considered. Due to this challenging nature, previous measurements limited themselves on simplified devices and empirical correlations for the effective global heat transfer coefficients have been proposed in literature.

Howey et al. (2012) recently reviewed studies on the convective heat transfer within the air gap of cylindrical and disk geometry rotating electrical machines. Herein, they showed empirical correlations for example from turbo machinery to be well applicable for rotating electric machines, as well. Earlier, Fénot et al. (2011) summarized previous studies on heat transfer within concentric rotating cylinders with and without axial flow. They state the importance of Taylor-Couette flows for electric motors cooling being a long-existing

academic and industrial research field. In their review they concluded that although the global heat transfer for smooth cylindrical gaps is well documented, the influence of local heat transfer has not yet been investigated in detail.

Spatial resolution of local heat transfer distribution is a particular challenge in experiments. Therefore, Computational Fluid Dynamics (CFD) are being used more and more to investigate the heat transfer in rotary machines. Anderson et al. (2015) performed a CFD analysis with the commercial software STAR-CCM+ to evaluate forced air cooling and winding losses for high-speed air-cooled electric motors and proposed a new correlation to calculate the heat transfer coefficient for their application. Deaconu et al. (2015) numerically analyzed a non-uniform annular gap and, very recently, Hosain et al. (2017) studied the thermal behavior in an electric motor's air-gap using CFD. They used the commercial software Ansys Fluent to resolve the temperature and velocity field inside a closed electric motor. Although these studies show good accordance with measurements and empirical correlations, the simulation's detail is limited due to solving Reynolds Averaged Navier-Stokes equations (RANS), like the $k-\epsilon$, the $k-\omega$ or the Shear Stress Transport (SST) turbulence model. These turbulence models solve time averaged equations, so that small fluctuations are not resolved. In some cases, these models are not able to recover the mean flow characteristics correctly, for example when it comes to transient heat transfer coupling. To overcome this drawback, Large Eddy Simulations (LES) are often suggested (e.g. Chandra et al. 2010; Romanazzi and Howey 2015), which however require considerably more computing power than RANS models.

Despite the high speed of modern computers, which allow simulations of increasingly complex flow problems, LES are rather uncommon in industrial applications due to the high demands on parallel computation power. A promising discretization approach is the Lattice Boltzmann Method (LBM) (S. Chen et al. 1998; Aidun and Clausen 2010), which has already shown in earlier studies that it is particularly suitable for LES in complex geometries and coupled physical effects (Fietz et al. 2012; Henn et al. 2016; Trunk et al. 2016). It uses parallel computers with several thousand processor cores very efficiently and thus enables large calculation grids with well over one hundred million cells in a matter of hours (Gaedtke et al. 2018c). With these features, the LBM is able to reduce the computing time required for LES (Jacob et al. 2019). A number of recent studies have investigated the applicability of the LBM for the simulation of turbulence by means of Direct Numerical Simulations (DNS), LES and RANS (Jahanshaloo et al. 2013). Hou et al. (1994) proposed the first LBM-LES model based on the constant coefficient Smagorinsky eddy viscosity, which was extended

by Dong et al. (2008) to be inertial range-consistent and later consistent sub grid closures for the BGK-Boltzmann equation were proposed by Malaspinas and Sagaut (2012). Meanwhile, the Smagorinsky eddy viscosity has also been adopted to the multi-relaxation time (MRT) collision operator (Krafczyk et al. 2003). Besides Smagorinsky-type LES models, the approximate deconvolution model has been introduced to the LBM (Sagaut 2010; Malaspinas and Sagaut 2011) and extended with adaptive filtering (Nathen et al. 2018). Very recently, Liou and C. S. Wang (2018) have applied an LBM based on constant coefficient Smagorinsky model to the simulation of turbulent heat transfer in a rotating channel.

However, the applicability of neither LBM-DNS nor LBM-LES to the determination of heat transfer in electrical machines has not yet been demonstrated, which directly motivates the aims of this work:

(a) verify, that the combination of LBM and LES is well suited for use in resolved air gap simulations and

(b) allow detailed analysis of local heat transport over a wide range of Taylor numbers, including time and spatially resolved turbulent properties.

It should be noted that LBM is relatively easy to apply to complex geometries. The annulus in this study is to be considered a first step providing validated and reliable simulation of the specific properties of this particular flow regime, whereas the application to more accurate gap geometries will be a simple one. Despite the axial symmetric geometry in this study and the possibility of using LBM on cylinder coordinates (Zheng et al. 2010), Cartesian coordinates were used here to (a) keep the extension to real, not necessarily axial symmetric engine geometries as straightforward as possible in the future and (b) maintain the validity of this validation study even under these apparently non-optimal conditions. The challenge is rather to simulate the coupled mass and heat transfers in the thin gap which are strongly influenced by Taylor vortices. This is accomplished with LBM for the first time in this study.

The next sections of this study are structured as follows. In Section 4.2 the machine geometry and its operating conditions are presented, while the fundamentals of Taylor-Couette flow including its flow structure and convective heat transfer are summarized. The LBM for the mass and momentum equation and the temperature equation are described in Sections 4.3.1 and 4.3.2, respectively. In Section 4.3.4 the sub-grid scale model is introduced, followed by the description of the application setup in Section 4.3.5. The results of the

Table 4.1: *Dimensions of the apparatus used in Becker (1957).*

annulus length	L	1.4224 m
heated length	L_{H}	1.4059 m
outer radius	r_{out}	42.774 mm
inner radius	r_{in}	34.531 mm
annulus width	$b = r_{out} - r_{in}$	8.2423 mm

present study are presented and discussed in Section 4.4. First, a grid convergence study is presented in Section 4.4.1. Then the flow properties and the heat transfer in the annulus are compared against earlier studies' findings in Sections 4.4.2 and 4.4.3, respectively. Finally a conclusion is given in Section 4.5.

4.2 Machine Geometry and Operating Conditions – Fundamentals of the Taylor-Couette Flow

The heat and mass flow is considered from rotor to stator through the air gap of a drum-type machine. For further information about the distinction between disk- and drum-type machines, the reader is referred to the review of Howey et al. (2012). Here, the main focus is placed on the basic problem of air flow and heat transfer between concentric cylinders with the inner cylinder rotating, hence neglecting end effects. This model problem, which is also known as the rotating Couette or the Taylor-Couette problem, is illustrated in Figure 4.1 with outer radius r_{out} and inner radius r_{in} of the annulus and rotating speed ω_{in} of the inner cylinder. In this article a Totally Enclosed, Fan-Cooled (TEFC) motor geometry is considered. Due to the closed housing there is no axial air flow in the air gap.

An extensive experimental and theoretical study on fluid flow and heat transfer between concentric cylinders with inner rotating and heated cylinder with and without axial flow is carried out by Becker as documented in his PhD thesis from 1957 (Becker 1957). This measurement series is used for validation of the simulation results. Becker's experimental data is well-founded and precise and thus is a good basis for validating the simulation results. The dimensions of the apparatus used therein are listed in Table 4.1.

A maximum rotational speed of $\omega_{in} = 550/\mathrm{min}$ and consequently a maximum Taylor number of approximately 530 is obtained with this apparatus,

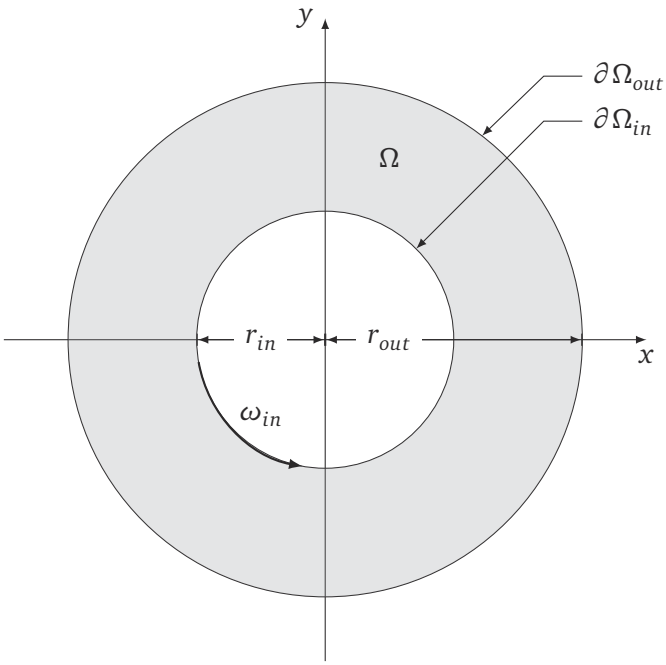

Figure 4.1: *Annulus with inner rotating cylinder at rotational speed ω_{in}. The flow domain Ω is bounded by two concentric cylinders $\partial\Omega_{in}$ and $\partial\Omega_{out}$ with radii r_{in} and r_{out}, respectively.*

where the Taylor number is defined by

$$\mathrm{Ta} = \frac{\omega_{in}\, {r_m}^{\frac{1}{2}}\, b^{\frac{3}{2}}}{\nu} \tag{4.1}$$

with the mean radius $r_m = \frac{1}{2}(r_{out} + r_{in})$ and the fluid's kinematic viscosity ν. Besides runs with axial flow, Becker measured 44 runs without axial flow and rotational speeds from 38.2/min to 522/min, which are used for comparison in this work.

4.2.1 Flow Structure

Elgar (1956) showed that four different modes of flow can be present in an annulus with an inner rotating smooth cylinder. The mode of flow which is present in the annulus depends on the axial velocity of the air in the annulus and the rotational speed of the inner cylinder. These four modes are:

1. Laminar flow
2. Laminar flow plus Taylor vortices
3. Turbulent flow
4. Turbulent flow plus Taylor vortices

The third and fourth type of flow can only be present with axial flow. As we consider concentric cylinders with an inner rotating cylinder and without axial flow, only the first and second type of flow are expected to occur. In addition to the axial air velocity and the rotating speed, the rate of heat transfer in the air gap of a real machine depends on the surface roughness of the cylinders and effects due to non-developed thermal and viscous boundary, which, however, are not considered here (Becker 1957).

For laminar flow between concentric cylinders without axial flow but with rotation of one or both of the cylinders the exact solution of the Navier-Stokes equations (NSE) is known:

$$u = A\, r + B\, \frac{1}{r}\,, \tag{4.2}$$

with the constants A and B given by

$$A = \frac{r_{out}^2\, \omega_{out} - r_{in}^2\, \omega_{in}}{r_{out}^2 - r_{in}^2}\,, \qquad B = \frac{r_{out}^2\, r_{in}^2 (\omega_{in} - \omega_{out})}{r_{out}^2 - r_{in}^2} \tag{4.3}$$

and the rotation speeds of the inner and outer cylinder ω_{in} and ω_{out}. When the outer cylinder is stationary and the inner cylinder rotates, (4.2) reduces to the circular type of Couette flow which is characterized by

$$u = -\frac{r_{in}^2\,\omega_{in}}{r_{out}^2 - r_{in}^2}\,r + \frac{r_{out}^2\,r_{in}^2\,\omega_{in}}{r_{out}^2 - r_{in}^2}\,\frac{1}{r}\,. \tag{4.4}$$

Laminar flow only holds for relatively small fluid velocities. If a certain velocity is exceeded, the flow becomes unstable, breaks down and Taylor vortices begin to form. Predicting the velocity at which transition from laminar to turbulent flow takes place is a complicated problem and is done in theory of hydrodynamic stability. The three types of hydrodynamic instability are:

1. Thermal instability
2. Centrifugal instability
3. Parallel flow instability

Thermal instability arises due to a temperature gradient. For the fluid flow in an annulus, a temperature difference between the inner and outer cylinder can lead to a transition from laminar to turbulent flow. A centrifugal force, which occurs when a fluid moves in curved streamlines, yields centrifugal instability. Whereas the parallel flow instability arises when a fluid flows in straight ducts. All of these types of instability play a role for the type of fluid flow in an annulus.

Once the transition point is exceeded, Taylor vortices occur in the annulus. When and how this transition takes place is discussed in the following subsection.

4.2.2 Stability of the Isothermal Couette Flow

Rayleigh (1917) was the first who studied the stability of isothermal fluid flow between rotating cylinders. Rayleigh's stability criterion leads to the assumption that the flow is always stable when the inner cylinder is stationary and the outer cylinder rotates. Contrary, if the outer cylinder is stationary and the inner cylinder rotates the flow is assumed to be always unstable. This conclusion contradicts the fact that Couette motion exists for low rotational speeds, but the discrepancy can be explained by the neglection of the viscosity in the derivation of the criterion. Additionally the results for an inner stationary cylinder and the outer cylinder rotating, are not correct. Experimentally it was found by

Taylor (1936), that the fluid flow becomes unstable for large rotational speeds of the outer cylinder.

Taylor made a theoretical and experimental study on the stability of viscous incompressible flow contained between rotating cylinders without axial flow by Taylor (1923). Taylor assumed that the gap width b is small in his calculations for the case where the inner and outer cylinder rotate in the same direction. Thus he located the lowest value for the rotating speed of the inner cylinder which causes growing perturbations. This value is called the critical rotational speed $\omega_{in,\mathrm{c}}$, which is used to calculate the critical Taylor number by

$$\mathrm{Ta_c} = \frac{\omega_{in,\mathrm{c}}\, r_m^{1/2}\, b^{3/2}}{\nu}\,. \tag{4.5}$$

If this critical value is exceeded, the laminar Couette flow breaks down. Instead of the characteristic random motion of a turbulent flow, Taylor found the flow to form pairs of counter-rotating vortices, now known as Taylor vortices.

By applying this to the case of a stationary outer cylinder, Elgar (1956) found the critical Taylor number $\mathrm{Ta_c} = 41.2$ for the limiting case, where $\frac{b}{r_m}$ tends to zero. With this, the critical Taylor number for an arbitrary value of $\frac{b}{r_m}$ can be expressed by

$$\mathrm{Ta_c} = 41.2\, F_g \tag{4.6}$$

with the geometrical factor $F_g = F_g(b, r_m)$. These theoretical findings have been approved experimentally e.g. by J. W. Lewis (1928).

4.2.3 Stability of the Couette Flow with Heat Transfer

The flow of a fluid confined between two horizontal and parallel plates is an analogous case to the fluid flow between concentric cylinders. This analogy was mathematically shown by Jeffreys (1928) for the limiting case, where $\frac{b}{r_\mathrm{m}}$ tends to zero.

In the case of a fluid confined between two parallel plates, the fluid flow can become unstable if the lower plate is heated. If the temperature difference through the fluid reaches a value that exceeds the critical Rayleigh number $\mathrm{Ra_c}$, convective motion starts in the fluid between the plates, where the Rayleigh number is defined by

$$\mathrm{Ra} = \frac{g\beta}{\nu\kappa}(T_{bot} - T_{top})b^3 \tag{4.7}$$

with the acceleration due to gravity g pointing in negative y-direction, the thermal expansion coefficient β and the thermal diffusivity κ the temperatures at

the bottom and top plate T_{bot} and T_{top} as well as the distance between the plates b. The first analytical study of this problem was done by Rayleigh (1916). Pellew and Southwell (1940) derived a differential equation for solving the characteristic value problem, solved this equation by variational calculus and found the critical Rayleigh number

$$\mathrm{Ra_c} = 1707.8\,. \tag{4.8}$$

In case of flow between concentric cylinders with the inner cylinder rotating, the force field is the centrifugal field in radial direction from the inner to the outer cylinder. Heating the inner cylinder creates a temperature gradient in the same direction as the centrifugal field. This leads to the assumption, that heating the inner cylinder stabilizes the flow while heating the outer cylinder destabilizes the flow. Becker (1957) did an analytical study of the stabilizing effect of a radial temperature gradient and found the critical Taylor number for the limiting case, where $\frac{b}{r_\mathrm{m}}$ tends to zero, as

$$\mathrm{Ta_c} = \sqrt{\mathrm{Ra_c} + \mathrm{Ra}}\,. \tag{4.9}$$

If the inner cylinder is heated, the Rayleigh number is positive. Therefore, the critical Taylor number in (4.9) is higher than the critical Taylor number without radial temperature gradient. If, otherwise, the outer cylinder is heated, the Rayleigh number is negative and the critical Taylor number becomes lower. These results confirm the assumption that heating the inner cylinder stabilizes the fluid flow and heating the outer cylinder destabilizes it.

Gazley (1958) supplied heat to the inner cylinder by a resistance heating coil and cooled the outer cylinder with a water jacket. He found that the Nusselt number

$$\mathrm{Nu} = \frac{2\,b\,q}{k_m\,A\,(T_{in} - T_{out})} \tag{4.10}$$

with the heat flux q, the thermal conductivity k_m, the surface area A and the temperature difference $(T_{in} - T_{out})$ remains constant for low rotational speeds, which means that the heat transfer is independent of the rotational speed for the laminar flow of low rotational speeds. Above the transition point where Taylor vortices begin to form, Gazley found increasing Nusselt numbers for increasing rotational speeds. Becker (1957) later found a good correlation between measurement results and laminar theory by taking the radiative heat transfer into account.

In this work we look at the most common electrical machines with an inner rotating rotor and an outer stationary stator. For this case and the dimensions listed in Table 4.1, no axial flow and no heating, the isothermal critical

Taylor number as described in Section 4.2.2 is calculated to

$$\mathrm{Ta_c} = 49.978 \tag{4.11}$$

with the geometrical factor $F_g = 1.2129$. The critical Taylor number with radial temperature gradient then calculates to

$$\mathrm{Ta_c} = 54.5\,. \tag{4.12}$$

This is about 9 % higher than the critical Taylor number without radial temperature gradient computed in (4.11). As mentioned above, heating of the inner cylinder stabilizes the fluid flow and leads to an increase of the critical Taylor number.

The empirical correlations and characteristic values presented here are considered as reference values for the validation of the proposed simulation method. To what extent these are reproducible by the simulations is examined in the following. For this purpose, the next section explains the methodology of the present model and the setup of the corresponding numerical experiments.

4.3 Methodology

The LBM is a grid-based method which is for example used for fluid flow simulations. The mesh is generated by discretisation of space with uniform step length Δx and discretisation of time with step length Δt. As usual in the literature, the time step Δt and the lattice spacing Δx are chosen in lattice units, such that $\Delta t = 1$ and $\Delta x = 1$. Quantities can easily be converted between lattice units and physical units by conversion factors (Krüger et al. 2017).

A discrete particle density distribution function $f_i = f_i(x,t)$ is used to trace the evolution of the fluid. This velocity distribution function represents the density of particles with discrete velocity $e_i = (e_{ix}, e_{iy}, e_{iz})$ at position x and time t. The mass density ρ and the momentum density ρu are known as the moments of f_i and can be calculated by weighted sums

$$\rho(x,t) = \sum_i f_i(x,t), \qquad \rho u(x,t) = \sum_i e_i f_i(x,t)\,. \tag{4.13}$$

The discrete velocities e_i together with weighting coefficients w_i are called velocity sets $\{e_i, w_i\}$. These velocity sets are named in the form $\mathrm{D}n_\mathrm{d}\mathrm{Q}n_\mathrm{q}$, where n_d stands for the space dimension and n_q for the number of velocity directions. In the present work the velocity set D3Q19 is used for the mass and momentum

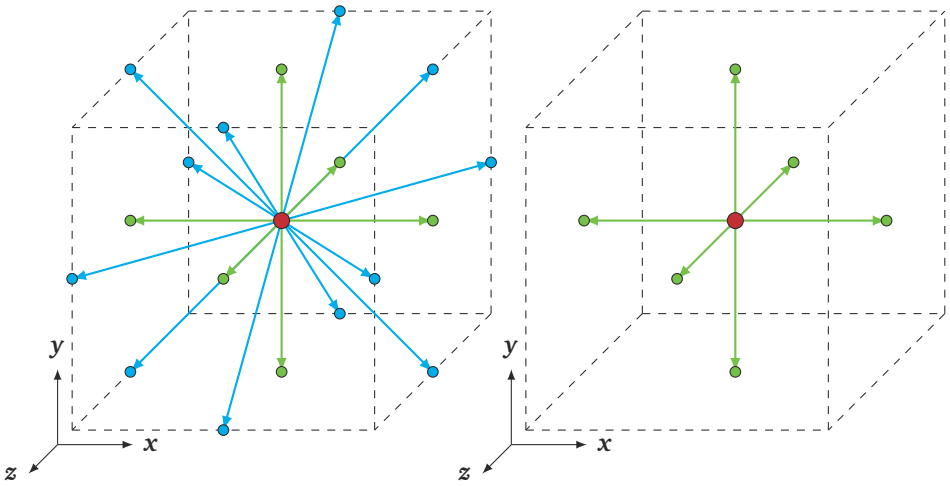

Figure 4.2: *Schematic representation of speed directions according to D3Q19 and D3Q7 (adopted form Gaedtke et al. (2018c)).*

equation, see Section 4.3.1. For the temperature equation (see Section 4.3.2), the velocity set D3Q7 is sufficient (Li et al. 2017). These velocity sets are popular choices by several authors (see e.g. Guo et al. 2002a; Yoshida and Nagaoka 2010; Li et al. 2013; Li et al. 2014a). Figure 4.2 shows the schematic representation of the D3Q19 and D3Q7 discrete velocity combinations used for the purpose of this paper. Depending on the direction of motion, predefined weighting factors w_i – distinguished by different colors in Figure 4.2 – are expressed in (4.14) for D3Q19 and in (4.15) for D3Q7. Note that the speed of sound in lattice units is $c_s = \sqrt{\frac{1}{3}}$ in the D3Q19 lattice and $c_s = \sqrt{\frac{1}{4}}$ in the D3Q7 lattice.

$$\text{D3Q19:} \quad w_i = \begin{cases} \frac{12}{36}, & |c_i| = 0 \\ \frac{2}{36}, & |c_i| = 1 \\ \frac{1}{36}, & |c_i| = \sqrt{2} \end{cases} \tag{4.14}$$

$$\text{D3Q7:} \quad w_i = \begin{cases} \frac{2}{8}, & |c_i| = 0 \\ \frac{1}{8}, & |c_i| = 1 \end{cases} \tag{4.15}$$

In this work we use the Double Distribution Thermal Lattice Boltzmann Method (DDT-LBM) including a Smagorinsky turbulence model as described in Gaedtke et al. (2018c), which is briefly summarized in the following Sections 4.3.1 to 4.3.4. For a detailed description and validation of the method, the reader is referred to the original article.

Two distribution functions f_i and g_i are introduced in Sections 4.3.1 and 4.3.2, solving the incompressible Navier-Stokes equation (NSE) and the advection-diffusion equation (ADE) for the temperature, respectively given by

$$\nabla \cdot u = 0 \quad , \quad \frac{\partial u}{\partial t} + (u \cdot \nabla)u - \nu \nabla^2 u = -\frac{\nabla p}{\rho_0} \tag{4.16}$$

and

$$\frac{\partial T}{\partial t} = \kappa \nabla^2 T - u \cdot \nabla T \tag{4.17}$$

with the velocity u, kinematic viscosity ν, pressure p and reference density ρ_0, temperature T, thermal diffusivity κ. The Smagorinsky sub-grid model is described in Section 4.3.4. It adds an eddy viscosity as well as an eddy diffusivity, which are incorporated into the Lattice Boltzmann equation (LBE) by modifying the relaxation times τ_f and τ_g.

4.3.1 LBM for Mass and Momentum Equation

The Single Relaxation Time Lattice Boltzmann Equation (SRT-LBE) including a force term $F_i(x,t)$ is given by

$$f_i(x + c_i \Delta t, t + \Delta t) - f_i(x,t) = \frac{\Delta t}{\tau_f}\left(f_i(x,t) - f_i^{eq}(x,t)\right) + F_i(x,t) \ , \tag{4.18}$$

where f_i denotes the discrete probability function and x denotes the space coordinate, t the time coordinate, i the discrete direction and c_i the discrete velocity in direction i. The collision operator is given by the Bhatnagar–Gross–Krook (BGK) operator. The discrete–velocity equilibrium distribution function f^{eq} is defined by

$$f_i^{eq}(\rho, u) = w_i \rho \left(1 + \frac{u \cdot e_i}{c_s^2} + \frac{(u \cdot e_i)^2}{2c_s^4} - \frac{u \cdot u}{2c_s^2}\right) , \tag{4.19}$$

where the weights w_i and the discrete velocities e_i are given by the chosen velocity set, D3Q19 in this work. By the Chapman-Enskog analysis described by e.g. Krüger et al. (2017) or Guo et al. (2000), it can be shown that the solution of the LBE consistently approaches the solution of the incompressible NSE. The kinematic shear viscosity ν is then given by the relaxation time τ_f as

$$\tau_f = \frac{\nu}{c_s^2} + \frac{1}{2}\Delta t \ . \tag{4.20}$$

The macroscopic values of density ρ and velocity u are calculated from the distribution function's moments

$$\rho(x,t) = \sum_i f_i(x,t) \text{ and } u(x,t) = \frac{1}{\rho}\sum_i e_i f_i(x,t)\,. \tag{4.21}$$

4.3.2 LBM for Temperature Equation

With the similarities between the ADE and the incompressible NSE, it is conclusive to use the same single relaxation time as in the Lattice Boltzmann algorithm for advection-diffusion problems:

$$g_i(x + e_i\Delta t, t + \Delta t) = g_i(x,t) - \frac{\Delta t}{\tau_g}(g_i(x,t) - g_i^{\text{eq}}(x,t)) \tag{4.22}$$

where g_i denotes the discrete temperature distribution function in velocity direction i. The equilibrium distribution function is deduced from the zeroth and first moments of g_i receiving the simplest equilibrium distribution function that leads to the macroscopic ADE as

$$g_i^{\text{eq}}(T,u) = w_i T\left(1 + \frac{e_i \cdot u}{c_s^2}\right), \tag{4.23}$$

where the velocity u is provided by the first moment of f, see (4.21).

Through Chapman-Enskog analysis it can be shown that the relaxation time τ_g is then given as a function of the thermal diffusivity κ by

$$\tau_g = \frac{\kappa}{c_s^2} + \frac{1}{2}\Delta t\,, \tag{4.24}$$

similar to the viscosity in the NSE (Mohamad 2011).

The macroscopic temperature is then obtained from

$$T(x,t) = \sum_i g_i(x,t)\,. \tag{4.25}$$

While the LBM for NSE requires preserving moments up to first order, the LBM for ADE does only need to preserve the zeroth moment. Hence lattices with less discrete directions are adequate in the LBM for ADE, so that the D2Q5 and D3Q7 lattice sets are sufficient (Li et al. 2017).

4.3.3 Coupling by Boussinesq Approximation

As fluid velocity and temperature mutually influence each other, they cannot be computed separately. In LBM it is possible to couple the velocity and temperature fields in order to model the interactions between them. This coupling is possible even if different lattices are chosen for the velocity field and the temperature field. Guo et al. (2002a) present a coupled LBM with the BGK collision operator, where the Boussinesq approximation is used for the coupling. Therein, the force term according to (4.18) is used to couple the two fields by the Boussinesq buoyancy force, which is given by

$$F(x,t) = -\rho_0 \beta g \left(T(x,t) - T_0\right) , \tag{4.26}$$

where ρ_0 and T_0 are the reference density and temperature and the forcing method described by Guo et al. (2002c) is used to obtain the lattice forcing term F_i as a function of F.

4.3.4 Turbulence Model

Our previous work in Gaedtke et al. (2018c) has shown the usefulness of the Smagorinsky sub-grid-scale model introduced to the LBM by Hou et al. (1994). In this method the effective viscosity ν_{eff} is set to be the sum of molecular ν_0 and eddy viscosity ν_t with

$$\nu_{\text{eff}} = \nu_0 + \nu_t = \nu_0 + (C_S \triangle)^2 \sqrt{2 \sum_{\alpha,\beta} S_{\alpha\beta} S_{\alpha\beta}} , \tag{4.27}$$

where the strain rate $S_{\alpha\beta}$ is computed locally using the non-equilibrium stress tensor $\Pi^{neq}_{\alpha,\beta}$ by

$$S_{\alpha\beta} = -\frac{1}{2\rho\tau_{f,\text{eff}} c_s^2} \Pi^{neq}_{\alpha,\beta} = -\frac{1}{2\rho\tau_{f,\text{eff}} c_s^2} \sum_q e_{i,\alpha} e_{i,\beta} (f_i - f_i^{eq}) \tag{4.28}$$

with $\tau_{f,\text{eff}} = \frac{\nu_{\text{eff}}}{c_s^2} + \frac{1}{2}$ denoting the modified relaxation time as a function of ν_{eff}. The Smagorinsky constant C_S is choosen as $C_S = 0.1$ and the filter width $\triangle$ is choosen as the mesh width $\triangle = \Delta x$.

Analogously, the effective thermal diffusivity is calculated by

$$\kappa_{\text{eff}} = \kappa_0 + \kappa_t = \kappa_0 + \frac{\nu_t}{\text{Pr}_t} , \tag{4.29}$$

where the turbulent thermal diffusivity κ_t is calculated by the turbulent Prandtl number

$$\mathrm{Pr}_t = \frac{\nu_t}{\kappa_t}\,, \tag{4.30}$$

which is set to $\mathrm{Pr}_t = 0.86$ for the scope of this work. This method is henceforth refereced as LBM-LES.

4.3.5 Discretization and Simulation Setup

The previously described LBM including its turbulence model has been implemented in the open source code OpenLB, which is used for the simulations in this work. This section describes the implementation within OpenLB. In Sections 4.3.5.1, 4.3.5.2 and 4.3.5.3 are presented the geometry preparation, choice of discretization parameters and boundary conditions. In Section 4.3.5.4 the choice of initial conditions for the velocity and temperature fields are given. The Nusselt number calculation is described in Section 4.3.5.5.

4.3.5.1 Geometry and Parallel Meshing

Construction of the three dimensional annulus in the simulation is accomplished by two cylinders with the radii r_{in} and r_{out} and length L. Subtracting the cylinder with the smaller radius r_{in} from the cylinder with the greater radius r_{out} yields the annulus, which represents the dimensions of the experiment as described in Section 4.2. The width of the annulus is small compared to the radii r_{in} and r_{out}. In order to get an accurate simulation the mesh length has to be chosen so small, that a sufficient number of lattice cells resolve the gap width. This number of cells over the gap width is henceforth called resolution N.

The dimensions of the annulus in Table 4.1 would lead to a huge amount of lattice cells, because of the relatively long length L of the annulus. *A priori* tests indicated, that the length of the annulus has an impact on the number and width of resolved Taylor vortices. Although, in order to make the simulations more efficient, the annulus is modeled with a length $\tilde{L} = 4\ b$ and periodicity is set in axial direction (z axis). This chosen length arrives at a global Nusselt number difference below 4 % between longer and shorter simulation domains and is thus sufficient for this work.

In OpenLB material numbers describe the simulated geometry and its boundaries. The boundary with the outer radius r_{out} is set to material number two, the boundary with the inner radius r_{in} is set to material number three.

For the air in the annulus, the material number one is used. Everything else is set to material number zero.

The geometry is split in several cuboids which can then be assigned to different CPU cores and be processed in parallel. After decomposition, the cuboid's extends are decreased in order to minimize cells with material number zero, where cuboids solely containing material number zero are dropped. Therefore the splitting in cuboids not only enables distributed memory parallelism, but also minimizes memory allocation of redundant cells. For details, the reader is referred to Fietz et al. (2012).

4.3.5.2 Discretization Parameters

Creating a grid for LBM is simple, because it is equidistant having the same lattice length in all space dimensions. The downside of such a uniform lattice is that, in the case of curvatures, the geometry representation strongly depends on the chosen resolution. *A priori* tests showed relatively good geometry representation for the given annulus for the lattice length

$$\Delta x_N = \frac{r_{out} - r_{in}}{N_{\min}} \tag{4.31}$$

with $N_{\min} = 16$ lattice points between the inner and the outer radius.

Besides the representation of the geometry, the choice of the lattice length depends on the simulation of the flow field. For an accurate simulation, the lattice has to be properly sized particularly near the wall. This is achieved by choosing a sufficiently small value for the parameter y^+, as described in the following. Based on White's Boundary Layer Theory (White 2003, p. 467), the distance of the first lattice point to the wall Δx_{y^+} is calculated by

$$\Delta x_{y^+} = \frac{y^+ \, \nu}{u_{\text{fric}}} \tag{4.32}$$

with

$$u_{\text{fric}} = \sqrt{\frac{C_f \, u_{\max}^2}{2}} \quad , \quad C_f = \frac{0.026}{\text{Re}_{\text{r}}^{1/7}} \quad \text{and} \quad \text{Re}_{\text{r}} = \frac{u_{\max} \, b}{\nu} \, , \tag{4.33}$$

where ν and ρ are the kinematic viscosity and density of the fluid, τ_{wall} is the wall shear stress, u_{fric} is the friction velocity, Re_{r} is the rotational Reynolds number and $u_{\max}$ is the maximum velocity. The maximum velocity $u_{\max}$ for the annulus between an inner rotating cylinder and an stationary outer cylinder is

assumed to be defined by the rotating speed of the inner cylinder

$$u_{\max} = \omega_{in}\, r_{in}\,. \tag{4.34}$$

For an accurate simulation of the flow's boundary layer, y^+ should be relatively small. In this work, y^+ is set to $y^+ = 2$, unless stated otherwise. The resulting lattice spacing is chosen as the minimum of lattice spacing calculated by y^+ in (4.32) and lattice spacing calculated by (4.31):

$$\Delta x = \min(\Delta x_N, \Delta x_{y^+})\,. \tag{4.35}$$

As a consequence, it is guaranteed that the geometry and the flow are accurately resolved – for low rotational speeds of the inner cylinder as well as for turbulent cases. This results in grids with resolutions of up to $N = 52$ with about 16.5 million fluid cells and more than 820 000 boundary cells.

To achieve an equivalent compromise between calculation duration and accuracy for the time discretization with time step Δt, the lattice Mach number is chosen to be constant for all simulations with

$$\mathrm{Ma} = \frac{u_{\max}}{c_s}\frac{\Delta t}{\Delta x_s} = 0.1\,. \tag{4.36}$$

4.3.5.3 Boundary Conditions

For the present simulations, the boundary values ω_{in}, T_{in} and T_{out} are set according to each measurement run from the experiments documented in the appendix of Becker (1957) resulting in Ra numbers from 721 to 1429. The outer cylinder is stationary in all runs, so the velocity of the annulus wall with radius r_{out} is set to zero. To simulate the rotation, the velocity of the lattice points corresponding to the inner wall of the annulus is set in accordance with the rotational speed of the inner cylinder ω_{in} by the function *RotatingLinear3D* of OpenLB. The function calculates the velocity on the boundary in x- and y-direction depending on the rotation axis z. The regularized boundary approach as described by Latt et al. (2008) is used for this purpose. The temperatures at the inner cylinder T_{in} and the outer cylinder T_{out} are set to their respective constant value, wherefore the Dirichlet-type temperature boundary scheme is implemented as described in Krüger et al. (2017).

4.3.5.4 Initial Conditions

Properly set initial conditions can lead to shorter simulation times if one knows how the fluid flow is supposed to develop. Another reason for an initial condi-

tion unequal to zero is the fact, that a simulated model is an ideal model without any disturbances. For example the walls are taken as perfectly smooth, the cylinders as perfectly concentric and so on. A measurement always deals with slight deviations of the position or texture of the components. These deviations can contribute to faster development of the flow.

In a model without such deviations and without wall roughness, it can take an unnaturally long simulation time for the turbulent flow to develop, especially in the transition regime. For a given rotational speed, all fluid cells are initialized with the velocity and temperature distributions linearly approximated between the boundary values. In order to speed up the formation of eddies during the simulation, some small disturbance is added. So, random values between plus and minus five percent of the local value are added at each lattice point.

4.3.5.5 Nusselt Number Calculation

A target-oriented way for the comparison of simulation results and measurement results is the computation of the Nusselt number. To compute the Nusselt number in the simulation, the wall of the inner cylinder is chosen. For each lattice point of the inner cylinder boundary condition $\partial\Omega_{in}$, its individual heat flux q_j is computed by

$$q_j = -k_m \nabla T(x_j) \cdot n(x_j) \quad \text{for } x_j \in \partial\Omega_{in}\,, \tag{4.37}$$

where ∇T is the temperature gradient, n is the normal vector on the inner cylinder and x_j is the position vector of the individual lattice point. The radial direction depends on the x- and y-position of the wall lattice point x_j and is independent of the z-position because the z-axis is orthogonal to the radial direction. The temperature gradient is approximated by the forward finite difference with second order accuracy as given by

$$\nabla T(x_j) \cdot n(x_j) \approx \frac{1}{\Delta x}\left(-\frac{3}{2}T(x_j) + 2T(x_{j+1}) - \frac{1}{2}T(x_{j+2})\right)\,, \tag{4.38}$$

with the boundary cell at x_j and first and second neighbor in the boundary's discrete normal direction x_{j+1} and x_{j+2}. The sum over the boundary heat fluxes is then divided by the number of inner boundary lattice points N_{in} to get the average Nusselt number over the area of the inner cylinder with

$$\mathrm{Nu} = -\frac{2\,b}{(T_{in} - T_{out})\,N_{in}} \sum_{x_j \in \partial\Omega_{in}} \nabla T(x_j) \cdot n(x_j)\,. \tag{4.39}$$

The Nusselt number is not only used for comparing the simulation results with the measurement results or other simulation results. Additionally the Nusselt number is used as termination condition. The simulation is considered converged, when the standard deviation of five sequential Nusselt number calculations each 1000 time steps is smaller than 10^{-4}.

4.4 Results and Discussion

4.4.1 Grid Convergence Study

In order to verify the simulation's correctness it is common practice to conduct a grid convergence study. Therefore, the problem is solved with several grid refinements. It is assumed that the simulation, usually indicated by a chosen global key value, converges to the correct value for an infinitesimal fine grid. In lack of such a grid, we compared the global Nusselt number for several coarse grids against the corresponding Nusselt number calculated from the finest grid used. Therefrom we introduce a relative error ϵ_{Nu} for each coarse resolution N as

$$\epsilon_{\mathrm{Nu}} = \frac{|\mathrm{Nu}(N) - \mathrm{Nu}(N_{\mathrm{fine}})|}{\mathrm{Nu}(N_{\mathrm{fine}})}\,, \tag{4.40}$$

where N is the number of grid cells over the gap width.

In order to compare the accuracy of the present model, corresponding simulations were carried out using a Finite Volume Method (FVM). Ansys' commercial code CFX was used to solve the steady-state RANS equations with the Shear Stress Transport (SST) turbulence model from Menter (1994) and with automatic wall functions, the details of which are documented in Ansys (2006). The mesh is created with a fine inflation layer close to the walls to assure proper boundary layer resolution. For the heat transfer, the *total energy* option was chosen with the reference temperature set as an expert parameter. This setup has been used by Hosain, Fdhila and Rönnberg in Hosain et al. (2017) and led to reliable results. This setup is further referenced as FVM-SST.

Relative errors for three different rotational speeds $\omega_{in} = 40/\mathrm{min}$, $75/\mathrm{min}$ and $206/\mathrm{min}$ and for four different resolutions are shown in Figure 4.3. The resolution has been varied between 10 to 40 cells over the gap width for FVM-SST and 4 to 64 cells over the gap width for LBM-LES, where the resolution of the fine grid is chosen to be $N_{\mathrm{fine,FVM\text{-}SST}} = 60$ for FVM-SST and $N_{\mathrm{fine,LBM\text{-}LES}} = 128$ for LBM-LES, respectively. Both methods show approximately constant Experimental Order of Convergences (EOC). Although the LBM simulations are sta-

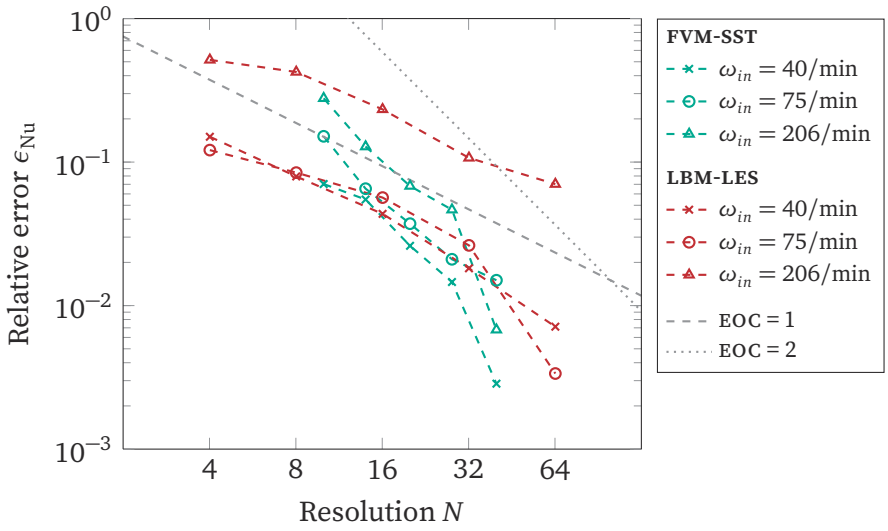

Figure 4.3: *Relative error of the Nusselt number for three different rotational speeds plotted over the resolution. Comparison of the Experimental Order of Convergence (*EOC*) between* FVM-SST *and* LBM-LES.

ble and relatively accurate even at very low resolutions of only 4 and 8 lattice cells, they show a first order convergence. From the method's derivation one could expect to see a second order convergence here, which is displayed for the FVM-SST. The loss of an order is probably caused by the present boundary condition scheme, which does not consider the curvature of the geometry, but uses a staircase approximation instead. Proposed schemes for curved boundaries such as the interpolated bounce back from Bouzidi et al. (2001) or the non-equilibrium extrapolation scheme from Guo et al. (2002b) have either not been extended for constant temperature boundaries or have not been demonstrated to be stable in turbulent regimes, yet. Therefore, the addition of a curved boundary scheme compatible with the present LBM goes beyond the scope of this work and will be considered in a future study. Besides the lower order, the LBM can compete well against the FVM's results with lower relative errors for resolutions up to 16 for the cases without Taylor vortices ($\omega_{in} =$ 40/min and 75/min). For the case with Taylor vortices, FVM-SST shows smaller errors with all resolutions tested here, which indicates the advantage of spatial grid refinement near the wall over equidistant cells for this regime.

4.4.2 Flow Characteristics

Figure 4.4 shows streamline representations of the simulation results with rotational speeds of 50/min, 206/min and 401/min from left to right. As expected from theory, the streamlines of the simulation with rotational speed 50/min of the inner cylinder are laminar as shown in Figure 4.4a, no vortexes occur and the streamlines are parallel to each other. The Taylor number with $\mathrm{Ta} = 47.19$ is smaller than the critical Taylor number. In Figure 4.4b simulated streamlines at rotational speed 206/min are shown. In this simulation the Taylor number $\mathrm{Ta} = 197.27$ is higher than the critical Taylor number. Therefore, Taylor vortices are expected to be present and this is in good agreement with the Taylor vortices shown in Figure 4.4b. The Taylor number $\mathrm{Ta} = 389.14$ of the simulation with rotational speed 401/min is even higher. Figure 4.4c shows, that in this case the Taylor vortices are more bundled than the Taylor vortices of rotating speed 206/min in Figure 4.4b. A slice through the x-y-plane showing a vector representation of the axial part of the flow field is given in Figure 4.5. Here again, the resolved vortexes are in very good agreement with previous results (Fénot et al. 2011).

Besides Taylor vortices with strong periodicity in the rotation direction, this studies' simulations are able to recover the wavy regime. This regime is first mentioned by Coles (1965), who found Taylor vortices to have a non strictly perpendicular orientation to the cylindrical axis for $1.2 \leq \frac{\mathrm{Ta}}{\mathrm{Ta}_c} \leq 96$ (Fénot et al. 2011). Figure 4.6 shows isosurfaces of the Q-criterion of $80/\mathrm{s}^2$ from the simulation with Taylor number $\mathrm{Ta} = 116$ with the Q-criterion defined as

$$Q = \frac{1}{2}\left(|\Omega|^2 - |S|^2\right) \tag{4.41}$$

with the vorticity tensor Ω and strain rate tensor S (Haller 2005). The wave characteristic is found to be in good accordance with earlier findings in Fénot et al. (2011).

4.4.3 Heat Transfer

4.4.3.1 Local Heat Transfer

Figure 4.7 shows an exemplary instantaneous temperature field and the corresponding local heat transfer in radial direction as computed by (4.37). With its fluctuating heat transfer over the rotation axis, the heat transfer's dependency from the Taylor vortices is clearly shown. The radial heat flux is high, wherever a vortex pair convects heat from inner to outer cylinder, it is low wherever

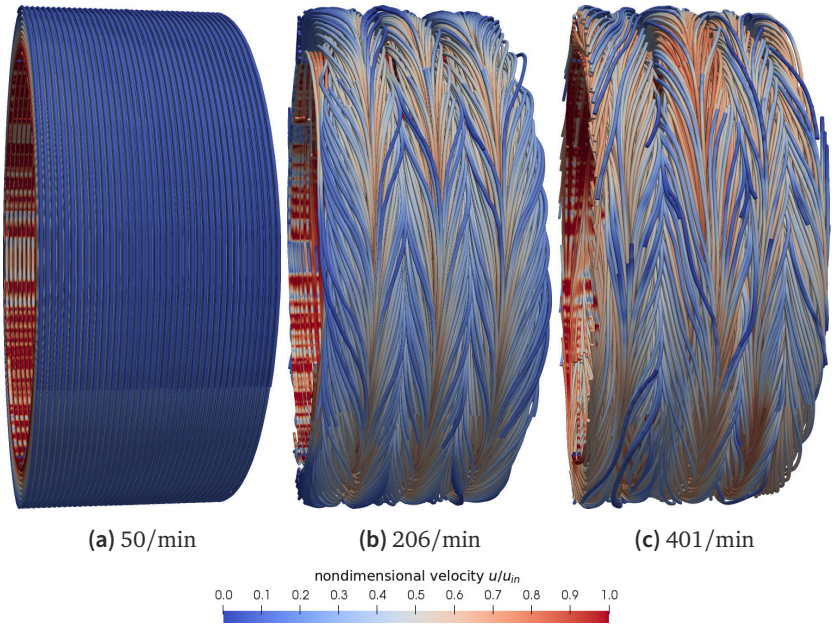

(a) 50/min **(b)** 206/min **(c)** 401/min

Figure 4.4: *Streamlines with rotating speeds* $\omega_{in} = 50/\text{min}$, $206/\text{min}$ *and* $401/\text{min}$ *of the inner cylinder from* LBM-LES *simulation. Blue indicates a velocity magnitude of zero, red indicates the velocity magnitude of the inner cylinder.*

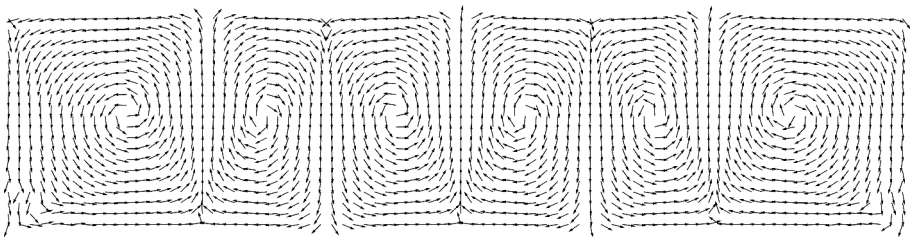

Figure 4.5: *Instantaneous velocity distribution in the y-z-plane indicated by vector arrows.*

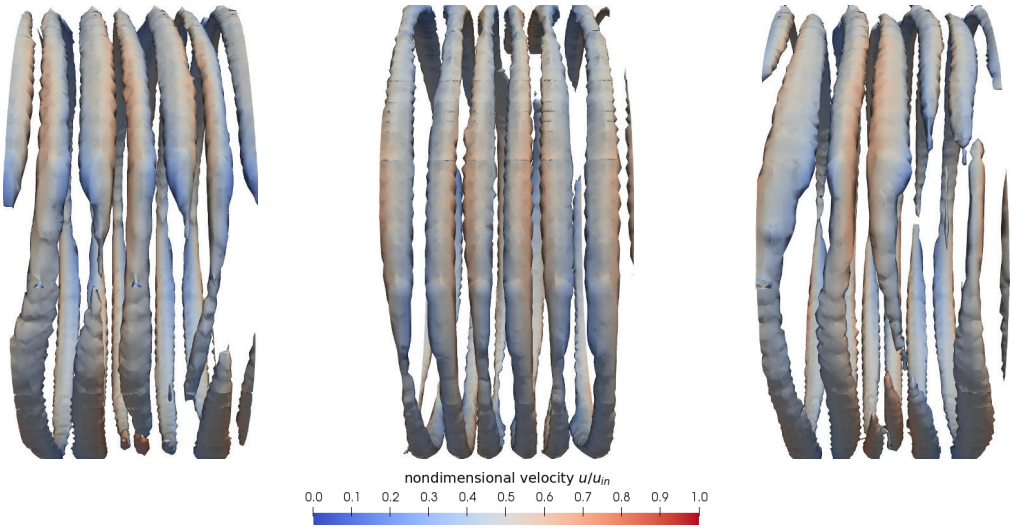

Figure 4.6: *Isosurface of the Q-criterion of* $80/s^2$ *at three different time steps showing the wave character of the taylor eddies. Blue indicates a velocity magnitude of zero, red indicates the velocity magnitude of the inner cylinder.*

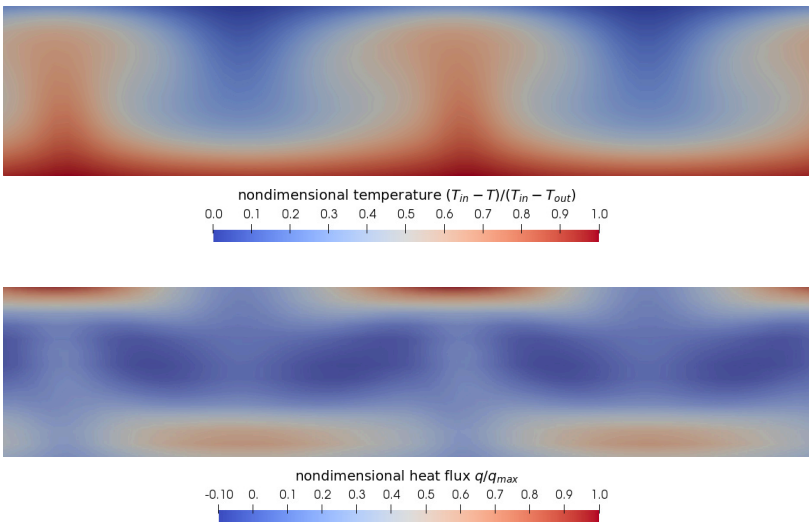

Figure 4.7: *Instantaneous temperature field and corresponding local heat transfer rate in radial direction in the y-z-plane. Blue indicates the temperature of the outer cylinder, red indicates the temperature of the inner cylinder in the upper figure and blue indicates the minimum heat flux in radial direction and red the maximum heat flux in the lower figure.*

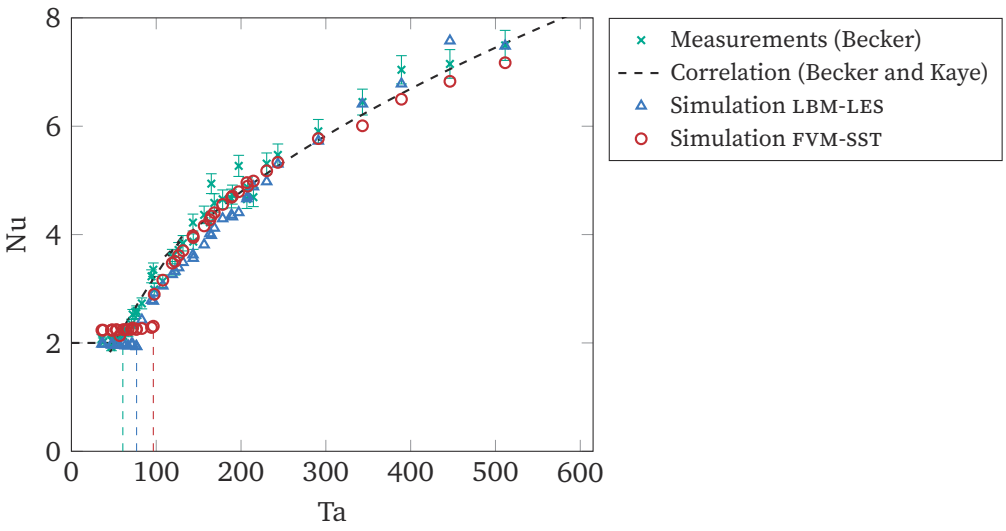

Figure 4.8: *Nusselt number over Taylor number: Comparison of meassured data from Becker (1957) and the correlation from Becker and Kaye (1962) against simulation results by* LBM-LES *and* FVM-SST.

vortex pairs flow towards the inner cylinder. This is in good agreement with previous results, e.g. Howey et al. (2012) or Hosain et al. (2017).

4.4.3.2 Global Heat Transfer

By averaging the local heat transfer over the surface of the inner cylinder, the global net heat flux is derived, from which the global Nusselt number is computed (see (4.39) in Section 4.3.5.5) to compare the simulation results against measurements and correlations. Here, we compare against measurements over a wide range of Taylor numbers by Becker (1957). Later, Becker and Kaye (1962) derived an empirical correlation for the global Nusselt number from these measurements, which is also used for comparison. Figure 4.8 shows the measurements, the correlation and present simulation results for the global Nusselt number over the Taylor number. The measurement results are plotted with error bars, which represent the relative error 3.7 % given by Becker (1957).

Overall, the simulation results for the global Nusselt number of both, FVM-SST and LBM-LES, are in good agreement with the measurement results as well as the correlation. Additionally, these results show that both simulation methods predict a higher critical Taylor number than the theoretical critical Taylor number $\mathrm{Ta}_c = 54.5$ and the critical Taylor number $\mathrm{Ta}_c = 60.6$ obtained by

the measurements of Becker. While the LBM-LES simulations predict a critical Taylor number of $\mathrm{Ta}_{\mathrm{c,LBM\text{-}LES}} = 76.8$, the simulations with FVM-SST even yield a critical Taylor number of $\mathrm{Ta}_{\mathrm{c,FVM\text{-}SST}} = 96.6$. For Taylor numbers below the critical Taylor number, the simulation results are in very good agreement with the measurement results. Excellent agreement with theory is obtained for the radial temperature distribution of simulations with Taylor numbers below the critical Taylor number Ta_c, where fully developed laminar flow is present in the annulus (not shown here).

When the critical Taylor number obtained by LBM-LES is exceeded, the Nusselt numbers from the present simulations are also in good agreement with the Nusselt numbers from Becker's measurements. It is noticeable, that the Nusselt numbers from the LBM simulations are slightly lower than the Becker's Nusselt numbers.

The average relative error of the Nusselt number over all 44 experiments is defined by

$$\epsilon^\star = \frac{1}{44} \sum_{i=1}^{44} \frac{|\mathrm{Nu}_{\mathrm{m},i} - \mathrm{Nu}_{\mathrm{s},i}|}{\mathrm{Nu}_{\mathrm{m},i}} \tag{4.42}$$

where i denotes the simulation of the corresponding measurement run, Nu_m is the Nusselt number obtained from the measurements of Becker (1957) and Nu_s the Nusselt number obtained from the simulation. With this definition the average relative errors of the simulations are

$$\epsilon^\star_{\mathrm{FVM\text{-}SST}} = 6.907\,\% \quad \text{and} \quad \epsilon^\star_{\mathrm{LBM\text{-}LES}} = 8.199\,\% \,. \tag{4.43}$$

Although these errors are quite close, the average relative error of the LBM simulation is slightly higher, which could be addressed in the future for example by another choice of y^+, considering curved boundary schemes or a wall adaptive LES. In spite of the slightly higher error, one should also consider the simulation time required to achieve this error: An average run with the rotational speed of $\omega_{in} = 151/\mathrm{min}$ needs approximately 20 min with Ansys CFX on 4 cores, for which the mesh is generated beforehand requiring user input. The present LBM converges to a steady Nusselt number in under 6 min on a 20 core node – including automated mesh generation, decomposition and load balancing. The LBM is therefore favored if different geometries are frequently meshed and run in parallel, as is common for rapid product development cycles.

One reason for the higher Ta_c predicted by the simulation could be the overdissipative LES and SST turbulence models. In the transition regime between laminar flow field and first Taylor eddies, the eddy viscosity models are

known to spuriously add diffusion to the system and therefore smoothen it, while small perturbations should lead to small scale eddy structures, see e.g. in Sayadi and Moin (2012). To confirm this hypothesis in this particular case, further DNS were conducted. For the DNS runs, the Smagorinsky model was deactivated so that the model falls back to standard BGK-collision scheme (see Section 4.3.1), henceforth referenced as LBM-DNS. In addition, the model's grid was refined to assure well resolved flow field by choosing $y^+ = 0.6$ in (4.32).

Figure 4.9 compares the LES and DNS simulation results with the measurements and correlation for the transition regime. Yielding a critical Taylor number of $\mathrm{Ta}_c = 61.1$, the LBM-DNS is able to recapture the measured critical Taylor number almost exactly, which confirms the hypothesis proposed earlier. For further studies on the transition regime it is recommended to use the DNS setup for reliable results, despite the higher computational cost compared to the LES setup. Besides applying the constant coefficient Smagorinsky model, a dynamic Smagorinsky procedure following Premnath et al. (2009) could deliver even better results for the transition regime. However, a similar dynamic procedure for a thermal LBM has not been presented, yet. Consequently, future research will have to derive and develop a dynamic Smagorinsky model for the thermal LBM and investigate its accuracy for this particular application.

4.5 Conclusion

In the present work the applicability of the present LBM-LES on the determination of flow characteristics and heat transfer has been examined. Namely, Taylor eddies in an annular gap with inner rotating cylinder have been resolved with an LES model. We showed detailed simulations on a large range of rotational speeds from almost creeping flow to mid-range turbulent cases and found good agreement with the previous results for the flow structure. Furthermore, heat transfer enhancement resulting from Taylor eddies has been simulated with good agreement to previous measurements.

To validate the proposed simulation setup, we compared our global heat transfer simulations to the measurements of Becker and a correlation from Becker and Kaye and simulations using Ansys CFX with the SST turbulence model. Comparing the simulation results with the measurements of Becker and theoretical estimations, leads to the conclusion that the LBM is well suited for use for the simulation of fluid flow and heat transfer in an annulus. Besides precise recovery of the Taylor-Couette flow field and the resolution of transient

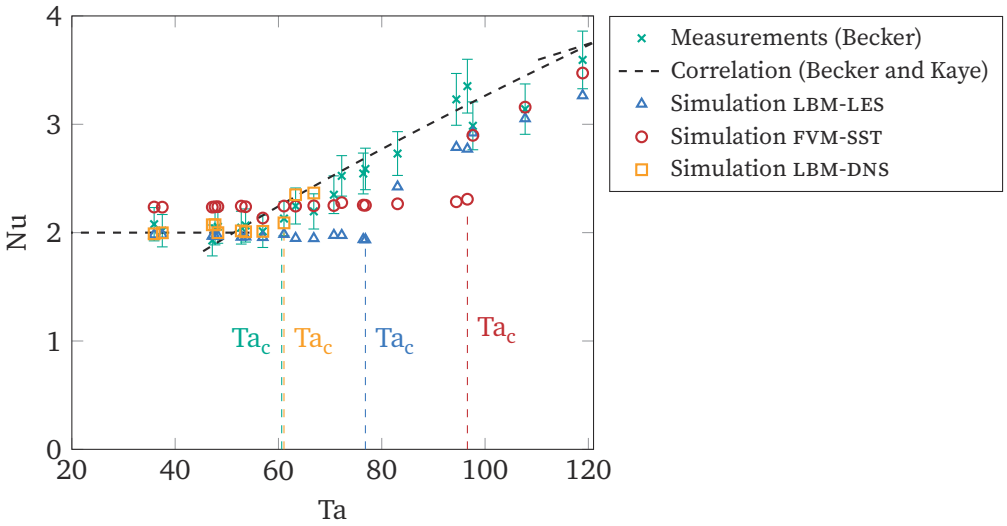

Figure 4.9: *Comparison of Nusselt numbers over Taylor number for the laminar and transition regime with meassured data from Becker (1957), correlation from Becker and Kaye (1962) and simulations results with* LBM-LES, FVM-SST *and* LBM-DNS *methods.*

wavy Taylor vortices, the LBM-LES does also compute accurate Nusselt numbers for heat transfer between concentric cylinders with inner rotating cylinder.

Special attention was paid on the prediction of the critical Taylor number. It has been demonstrated that with a Lattice Boltzmann DNS with a resolution of $y^+ = 0.6$ the critical Taylor number from experiments can be determined almost exactly, whereas with LES the occurrence of the Taylor vortices is slightly overestimated. The RANS simulations using the SST model in the configuration applied here further overestimate the critical Taylor number and are therefore not well suited for the transition range.

Using a relatively coarse grid with $y^+ = 2$ in the LBM-LES simulations, we found close agreement with all comparison values resulting in an overall mean error for the global Nusselt number below 8.2 %. Considering the challenge resolving Taylor-Couette flows and their corresponding heat transfer, this is a very good result.

Our results provide a valid basis for future applications of the proposed LBM-LES in thermal management of electric drives or similar rotating machines. Future work should focus on restoring second-order grid convergence

and wall-adaptive sub-grid models to further increase competitiveness with other numerical schemes.

5

Numerical Study on the Application of Vacuum Insulation Panels and a Latent Heat Storage for Refrigerated Vehicles with a Large Eddy Lattice Boltzmann Method

The development of sustainable trucks has drawn a lot of attention lately. However, the reduction of fuel consumption and emissions related to deep frozen food transports has not yet been satisfactorily considered. In this paper, a thermal Large Eddy Lattice Boltzmann Method (LES-LBM) is applied to investigate two concepts for optimized refrigerated vehicles: (a) the inclusion of vacuum insulation panels (VIP) in the refrigerated body's walls and (b) the introduction of a latent heat storage (LHS) to exchange fuel-driven air conditioning (AC), both with conveniently worth while potential to decrease fuel consumption and related emissions. The present numerical method allows for an accurate and efficient transient conjugate heat transfer simulation including the spatial and temporal resolution of the temperature distribution inside the insulation walls and the cargo in addition to the turbulent surrounding air flow induced by the AC.

The present concept of VIP inclusion is found capable of halving the required cooling energy. In addition, it effectively reduces the variations in the temperature of the chilled goods during cooling operation, which is an impor-

tant measure of the quality of the refrigerated body. The reduced required cooling energy is further found to enable the AC system to be replaced by an LHS mounted near the top of the refrigerator body and an additional ventilation system of lower total capacity. A comparison between simulations with conventional AC and LHS is conducted concerning the temperature homogeneity of loaded deep frozen food products. It is shown that a slight flow around the refrigerated goods is necessary and the maximum downtime of the AC system is 8 min in case of combined PUR and VIP insulation and 11 min in case of an additional LHS.

This chapter corresponds to the work of the same title published in the journal *Heat and Mass Transfer* (Gaedtke et al. 2020c). Following the contributor roles taxonomy (Brand et al. 2015), my contribution to this publication includes conceptualization, methodology, software, validation, formal analysis, investigation, data curation, writing – original draft, visualization, project administration and funding acquisition.

5.1 Introduction

At present, the use of fossil fuels (e.g. coal, oil and gas) is still increasing, due to industrialization of developing nations and growing world population (International Energy Agency 1998). In the last decades more and more renewable energy systems were developed, using hydro and wind power, geothermal heat, solar energy and others (Demirbaş 2006). Supporting the fossil energy revolution towards renewable energy supply, the European Commission (EC) presented a road map up to the year 2050 with suggested actions reducing the carbon dioxide emissions by 80 % to 95 % compared to the level of 1990 (European Commision 2012). It is argued that to reach these requirements, electricity will play a central role in a future low-carbon economy and that a sole change from fossil fuels to renewable energy resources in the energy production sector is insufficient (Van der Zwaan et al. 2013).

Recently, the attention on the mobility sector is increased with an initial focus on small passenger cars with combustion engines. As a start hybrid, plug-in hybrid and electric vehicles are developed, enabling the transportation over short distances (Al-Alawi and Bradley 2013). Another approach is the production of bio diesel for all heavy weight and transportation vehicles. By using biomass in a gasification process part of the actual diesel consumption can by replaced by bio diesel (Demirbaş 2006; Dahmen et al. 2017). The manda-

tory reduction of the diesel consumption of transportation vehicles may be achieved through an improvement in efficiency of many different small scale processes. One process with conveniently worth while potential to decrease fuel consumption and related emissions is the use of efficiently optimized refrigerated vehicles for the delivery of cooled products. Additional to their fuel-driven locomotion, a fuel-driven cooling unit is used in present vehicles. Furthermore, food delivery to personal homes in times of expanding internet food providers and upcoming ideas for autonomous driving cars will increase permanently and the optimized efficiency of improved insulation systems for refrigerated vehicles is mandatory for energetic as well as economic reasons.

Embedded in a long-term project many different improvement possibilities of the energy consumption for refrigeration are tested. Two promising concepts to reduce the fuel consumption of refrigerated trucks are considered in this paper:

- Concept A – insulation optimization using vacuum insulation panels (VIP),
- Concept B – passivation of the cooling effect by latent heat storages (LHS).

Concept A replaces previous used polyurethane rigid foam insulation at all possible locations through vacuum isolation panels (VIP). These panels are characterized by much lower heat conduction and at the same time lower thickness. VIP are filled and mechanically stabilized by highly porous grid structures made of polyurethane or silicates which are on both sides covered by a stable housing and evacuated. Through the porous grid, heat transfer through the panel can be reduced to values as low as the heat conduction of the branched structure plus radiation (Sonnick et al. 2019). Thus, thermal conductivities five to ten times lower than for traditional insulation are achieved (Wegger et al. 2011).

VIP were firstly applied in the construction industry for thermal insulation of external facades. Here filling materials could be used without high static load capacity and danger of vibrations. Initial test methods were applied to describe the average thermal conductivity of VIP. With the help of these test measurements, local differences in thermal conductivity were detected. This is known as the *edge effect*, whereby a high proportion of the heat conduction takes place through the frame of the panels (Wakili et al. 2004). Since the first experimental tests, most diverse studies on the thermal conductivity of the panels have been carried out with models for calculating the heat transfer of

different panel types (H. Singh et al. 2015). In addition to the core material, a dependence on the temperature level, internal pressure, gas type, permeability and water content in the internal residual air were found to be possible influencing parameters of thermal conductivity (Bouquerel et al. 2012; Lorenzati et al. 2017). Since the publication of the first reviews on VIPs, new areas of application have been identified, most notably the cooling and hot water technology (Kalnæs and Jelle 2014). In 2012 Bouquerel et al. (2012) proposed a model and applied it to describe combined heat transfer phenomena for determining an average thermal conductivity. They identified the main modeling disadvantages to be the assumptions of a regular structure and the Fourier law. Addressing these drawbacks, Ross-Jones et al. (2019) presented a pore scale model based on resolved packed bed simulations with a Lattice Boltzmann Method (LBM) taking into account solid and gas phase heat conduction as well as thermal radiation.

In concept B the fuel-driven cooling unit is exchanged with an LHS filled with a phase change material (PCM). Extensive reviews on the modeling and simulation of thermal behavior as well as initial tests on combinations of VIP and LHS have been carried out by Ahmad et al. (2006), Verma et al. (2008) and others. Zalba et al. (2003) showed a compilation of various phase change materials including solutions of salts with a suitable temperature range for the transport of refrigerated goods.

Due to the fact that prototypes of refrigerated bodies with built-in AC are expensive in material and manufacturing costs, computational fluid dynamics are used to investigate both concepts before actually constructing a prototype. In addition, spatially resolved measurements without influencing the wall properties or the flow properties in the system are costly if not hardly possible. In a previous study Gaedtke et al. (2018c) showed the applicability of a double distribution thermal LBM to the simulation of a refrigerated vehicle's insulation. By replacing the widely applied Reynolds averaging turbulence model with a large eddy turbulence model and transiently resolving the flow field, the refrigerated vehicle's walls and their conjugate heat transfer, they found much closer accordance to measured data than previous studies (James et al. 2006; Smale et al. 2006). The application of the inherently transient LBM to large eddy simulations (LES) has shown to provide a significant speedup and parallel scalability over traditional Finite Volume Methods, see for example in the work of Barad et al. (2017), where a speedup of ~12 is achieved by LBM over FVM for simulations on similar grids and with similar accuracy. With this scalable and fast solver and successful validation of realistic velocity and temperature

distributions in the interior of a refrigerated body it is consistent to employ the same simulation method in this study.

The structure of this paper is following the subsequent line of reasoning: Section 5.2 introduces the applied thermal LBM including the sub-grid scale model (Section 5.2.4) and used boundary conditions (Section 5.2.5). The refrigerated body's geometry, material properties and initial conditions are presented in Section 5.3, where three different simulation case setups are introduced: conventional PUR insulation (Section 5.3.1), improved PUR+VIP insulation (Section 5.3.2) and additional inclusion of an LHS (Section 5.3.3). In Section 5.4 the results of the two introduced concepts are discussed by comparison to the conventional PUR insulation case. Mass and heat flux simulations of the two insulation concepts are presented and an application on the leakage of rear doors is shown. Afterwards, the passivation of the temperature field is numerically assessed by an exchange of the cooling unit through the LHS. For this purpose six trolleys with deep-frozen goods, which are modeled by the material values of pure ice, are included in the simulation. The cargo temperature's sensitivity considering switching off the cooling engine is compared for three different insulation and cooling options by flow and temperature fields within the loaded refrigerated vehicle.

5.2 Mathematical Modeling

In this work we use the double distribution thermal LBM (DDT-LBM) including a Smagorinsky turbulence model as described in detail in our previous study (Gaedtke et al. 2018c), in which we also presented a rigorous validation of the model itself as well as its implementation in the open source code OpenLB. This validation study included

- a grid convergence study showing that the scheme is second order in space by comparing it with the analytical solution of the porous plate problem,
- a comparison with the benchmark of natural convection in a square cavity for different Rayleigh numbers from laminar to turbulent natural convection,
- and a comparison with measurements for the refrigerated transporter, which is also investigated in the current manuscript.

All three tests showed good agreement with the respective reference values. The method used is briefly introduced in the following Subsections 5.2.1 to 5.2.4, while the reader is referred to the original article for a detailed description and validation of the method.

Two distribution functions f_i and g_i are introduced in Sections 5.2.1 and 5.2.2 to solve the mass, momentum and energy equation on the macroscopic scale. The Smagorinsky sub-grid scale model is described in Section 5.2.4. It adds an eddy viscosity and an eddy diffusivity, which both are incorporated into the Lattice Boltzmann equation (LBE) by modifying the relaxation times τ_f and τ_g.

Note that the LBEs presented in the following are solved in their non-dimensional form. Thus, all physical quantities are converted to so called *lattice units* before the simulation and converted back before post processing. Krüger et al. (2017, Chapter 7) provide an overview on the dimensionalization of the LBE including complete instructions on how to choose corresponding conversion factors.

5.2.1 LBM for Mass and Momentum Equation

The Single Relaxation Time Lattice Boltzmann Equation (SRT-LBE) including a force term $F_i(x,t)$ is given by

$$f_i(x+e_i\Delta t, t+\Delta t) - f_i(x,t) = \frac{\Delta t}{\tau_f}\left(f_i(x,t) - f_i^{eq}(x,t)\right) + F_i(x,t) \tag{5.1}$$

with the discrete probability function f_i, the space and time coordinates x and t, the discrete velocity e_i, direction index i, and the equilibrium distribution function

$$f_i^{eq}(\rho,u) = w_i\rho\left(1 + \frac{u\cdot e_i}{c_s^2} + \frac{(u\cdot e_i)^2}{2c_s^4} - \frac{u\cdot u}{2c_s^2}\right). \tag{5.2}$$

Herein the weights w_i, the discrete velocities e_i and the speed of sound c_s are given by the standard D3Q19 velocity set (Krüger et al. 2017). The relaxation time τ_f in Equation 5.1 is given as a function of the kinematic shear viscosity ν with

$$\tau_f = \frac{\nu}{c_s^2} + \frac{1}{2}. \tag{5.3}$$

The macroscopic values of density ρ and velocity u are calculated from the distribution function's moments

$$\rho(x,t) = \sum_{i=0}^{18} f_i(x,t) \quad \text{and} \quad u(x,t) = \frac{1}{\rho}\sum_{i=0}^{18} e_i f_i(x,t). \tag{5.4}$$

5.2.2 LBM for Energy Equation

With the similarities between the advection-diffusion equation (ADE) and the incompressible Navier-Stokes equations, it is evident to use an analogous Lattice Boltzmann algorithm for advection-diffusion problems: The SRT-LBE for the energy equation is given by

$$g_i(x + e_i\Delta t, t + \Delta t) = g_i(x,t) - \frac{\Delta t}{\tau_g}(g_i(x,t) - g_i^{\mathrm{eq}}(x,t)) \tag{5.5}$$

with the discrete temperature distribution function g_i in discrete direction i, the equilibrium distribution function

$$g_i^{\mathrm{eq}}(T,u) = w_i T\left(1 + \frac{e_i \cdot u}{c_s^2}\right) \tag{5.6}$$

and the macroscopic temperature T. The velocity u is provided by Equation 5.4.

While the LBM for the NSE requires preserving up to first order moments (mass and momentum, see Equation 5.4), the LBM for the ADE does only need to preserve the zeroth order moment (temperature, see Equation 5.6). The first order moment of the LBM for the ADE calculates to Tu, which is not conserved during the collision operation stated above given that u is calculated from the distribution f rather than from g. Thus, using the D3Q7 lattice set is sufficient (Mohamad 2011).

The relaxation time τ_g is given as a function of the diffusion coefficient κ by

$$\tau_g = \frac{\kappa}{c_s^2} + \frac{1}{2}\,, \tag{5.7}$$

similar to the viscosity in the NSE (for example see Krüger et al. 2017).

The macroscopic temperature and heat flux Q are given by

$$T(x,t) = \sum_{i=0}^{6} g_i(x,t) \quad \text{and} \quad Q(x,t) = -A\lambda\nabla T(x,t)\,. \tag{5.8}$$

Herein, A is the surface area over which the heat flux is calculated and λ is the thermal conductivity.

5.2.3 Coupling by Boussinesq Approximation

In order to model the interactions between the velocity and temperature fields a coupling procedure is introduced. Guo et al. present a coupled LBM with

the BGK collision operator in (Guo et al. 2002a) based on the Boussinesq approximation. Therein, the force term according to Equation 5.1 is set to be the Boussinesq buoyancy force as

$$F(x,t) = -\rho_0 \beta g \left(T(x,t) - T_0\right) , \tag{5.9}$$

where ρ_0 and T_0 are the reference density and temperature, respectively, and the lattice forcing term F_i is calculated as a function of F with the forcing scheme presented by Guo et al. (2002c).

5.2.4 Large Eddy Turbulence Model

As in our previous work (Gaedtke et al. 2018c), the Smagorinsky sub-grid-scale model introduced to the LBM by Hou et al. (1994) is used. Following Hou et al., the viscosity ν in Equation 5.3 is replaced by the effective viscosity ν_{eff}, which is defined as the sum of molecular viscosity ν_0 and eddy viscosity ν_t with

$$\nu_{\text{eff}} = \nu_0 + \nu_t = \nu_0 + (C_S \triangle)^2 \sqrt{2 \sum_{\alpha,\beta} S_{\alpha\beta} S_{\alpha\beta}} , \tag{5.10}$$

with the Smagorinsky constant $C_S = 0.1$ and the filter width $\triangle = \Delta x$. The strain rate $S_{\alpha\beta}$ is computed locally using the second moment of the non-equilibrium distributions with

$$S_{\alpha\beta} = -\frac{1}{2\rho\tau_{f,\text{eff}} c_s^2} \sum_{i=0}^{18} e_{i,\alpha} e_{i,\beta} (f_i - f_i^{eq}) \tag{5.11}$$

and $\tau_{f,\text{eff}} = \frac{\nu_{\text{eff}}}{c_s^2} + \frac{1}{2}$ denoting the modified relaxation time as a function of ν_{eff}.

The thermal diffusivity κ in Equation 5.7 is analogously replaced by the effective thermal diffusivity given by

$$\kappa_{\text{eff}} = \kappa_0 + \kappa_t = \kappa_0 + \frac{\nu_t}{\text{Pr}_t} , \tag{5.12}$$

where the turbulent thermal diffusivity κ_t is calculated by the turbulent Prandtl number

$$\text{Pr}_t = \frac{\nu_t}{\kappa_t} = 0.86 . \tag{5.13}$$

5.2.5 Boundary Conditions

As in our previous work (Gaedtke et al. 2018c) Latt's regularized boundary approach (Latt et al. 2008) is used for pressure and velocity boundary conditions. A constant temperature boundary condition is implemented as described in Krüger et al. (2017) and the outflow boundary condition for the temperature is used as recommended by Junk and Z. Yang (2008). Simple bounce back (Succi 2001b) is used for no-slip and adiabatic boundaries. The half lattice division scheme described by J. Wang et al. (2007) is utilized to simulate conjugate heat transfer, where the diffusion equation and the advection-diffusion-equation are solved in solid and fluid regions, respectively, on a single mesh.

5.3 Geometry, Material Properties and Simulation Case Setups

5.3.1 Refrigerated Body Geometry and Conventional PUR Insulation

A refrigerated body for the commercial vehicle Mercedes-Benz Sprinter 316 is applied in this study. The refrigerated body itself is the model CoolerBox 2.0 TK 3500 HS from *Kress Fahrzeugbau GmbH* with a double wing rear door and polyurethane hard foam (PUR) insulation walls as shown in the schematic representation in Figure 5.1. The respective wall thicknesses and dimensions of the cooling unit are summarized in Table 5.1. The Carrier Xarios 500T cooling unit is installed, which can be used for both, heating and cooling purposes with a full-load volume flow of $\dot{V} = 990\,\mathrm{m/h^3}$ and a heating and cooling capacity of $Q = 950\,\mathrm{W}$. The energy supply of the transport refrigeration system can be provided either by the diesel engine installed in the vehicle during the journey or externally by 400 V three-phase current during longer rest periods.

The material properties of the internal air and the PUR insulation are given in Table 5.2. At $t = 0$ the velocity in the simulation domain is set to 0 m/s, while the internal air temperature is set to −20 °C. The insulation walls are set to 5 °C and the outer surface of the refrigerated body is assumed to have a constant temperature of 30 °C. It should be mentioned, that the latter represents a worst case scenario for the central European food transport.

The AC flow rate and cooling capacity are adjusted according to the manufacturer information by calculating appropriate velocity and temperature values for the AC outlet boundary every 50 time steps. In order to ensure a stable simulation, the AC flow rate is ramped up to its desired value over a time span

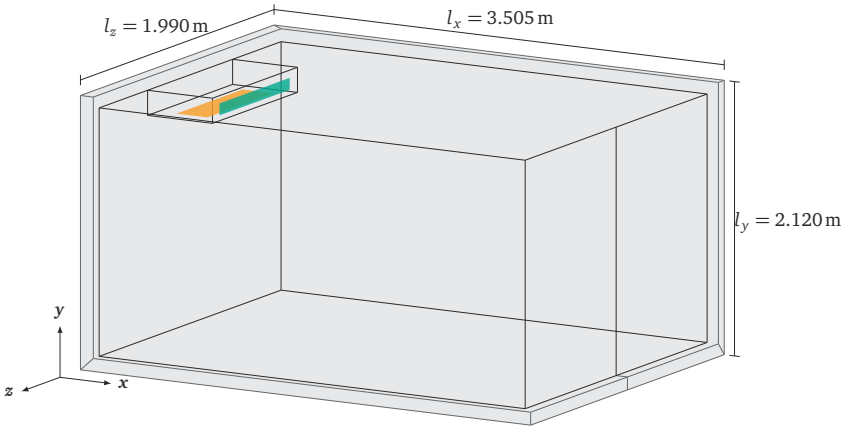

Figure 5.1: *Schematic representation of the refrigerated body and the built-in* AC *system. The* AC*'s outlet and suction side are shown in green and orange, respectively. Adapted from Gaedtke et al. (2018c)*

Table 5.1: *Summary of the geometric dimensions of the refrigerated body, the* AC*, its outlet (O) and suction side (S).*

Refrigerated Body				Air Conditioning Unit			
Dimensions		Wall Thicknesses		Dimensions		Openings	
Length:	3.505 m	Ground:	0.1 m	Length:	0.505 m	(S) Length:	0.12 m
Height:	2.120 m	Ceiling:	0.1 m	Height:	0.194 m	(S) Width:	0.79 m
Width:	1.990 m	Front:	0.1 m	Width:	0.874 m	(O) Height:	0.06 m
		Rear Door:	0.085 m			(O) Width:	0.79 m
		Sides:	0.065 m				

Table 5.2: *Material properties (thermal conductivity λ, density ρ, specific heat capacity c_p, thermal expansion coefficient β and kinematic viscosity ν) for air according to* VDI *Heat Atlas and for the insulation materials* PUR *and* VIP *according to* VDI *Heat Atlas, Eberhardt (2005) and Kwon et al. (2009).*

	λ	ρ	c_p	β	ν
	$10^{-3}\,\mathrm{W/(m\,K)}$	$\mathrm{kg/m^3}$	$10^3\,\mathrm{J/(kg\,K)}$	$10^{-3}\,\mathrm{1/K}$	$10^{-6}\,\mathrm{m^2/s}$
Air	22.62	1.378	1.007	3.974	11.766
PUR	23.00	39.50	1.400	–	–
VIP	7.00	1140	0.746	–	–

of 20 s.

The challenge achieving a physical simulation time of 60 s and more is passed using massive parallel execution of the LB solver on a cluster computer, namely the KIT research high-performance computer FORHLR II. For the scope of this study, the refrigerated body is discretized with about 65 million grid points, which requires eight hours calculation time on 1000 allocated CPU cores for a physical simulation time of 60 s. With the chosen lattice Mach number of $\mathrm{Ma} = 0.2$ a physical simulation time of 60 s corresponds to about half a million time steps.

The geometry and model described above have been validated successfully against transient experimental data for a period of 60 s from 17 characteristic measuring points in the refrigerated body, 13 for the temperature distribution and 4 for the velocity distribution with absolute errors below 0.4 m/s and below 1 K, respectively. The execution of the validation study and its results have been described in detail in our previous work (Gaedtke et al. 2018c).

The conventional PUR insulation is considered as a reference case; its simulation setup is referred to as PUR in the following.

5.3.2 Integration of Vacuum Insulation Panels

For the largest possible integration of the VIPs without changing the outer design of the refrigerated body, the new insulation is mounted in all parts of walls, where no interfering elements such as hinges, edges, corners and brackets exist. A schematic illustration of the resulting insulation concept applying VIPs is shown in Figure 5.2. Herein, light gray elements show a framework made from hard foam insulation, while clear areas are filled with VIPs in the following simulations.

This insulation concept cannot be realized with conventional VIP elements. To ensure an elegant integration into the refrigerated box, the silica-based core material mixture is pressed directly into a frame made of PUR. The walls are made of glass fibre reinforced plastic (GRP), comparable to conventional refrigerated boxes, to ensure the mechanical stability required for this application.

The aforementioned edge effect observed with conventional VIPs is mainly caused by the foil packaging containing metallized layers to reduce gas diffusion through the envelope. This effect is negligible in the present concept as no metallised foil is used. In order to compensate for an inevitable increase in internal pressure over time, it is possible to re-evacuate the VIP elements at a

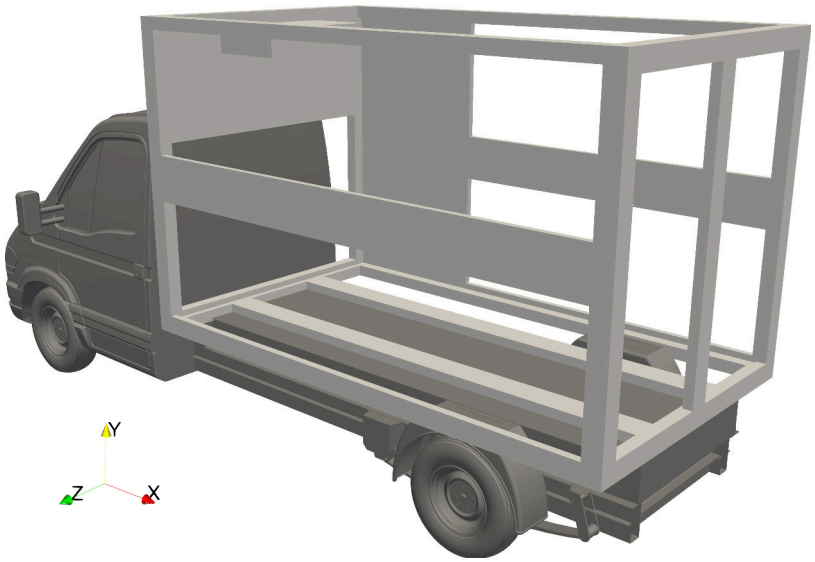

Figure 5.2: VIP *integration concept: Schematic illustration of the refrigerated body. Light gray areas represent the framework made of conventional* PUR *insulation, the clear areas are filled with* VIPs.

later date using an integrated pump.

The surface area replaced by VIPs is calculated to 21.672 m^2 replacing 58.2 % of the body's outer or 67.2 % of it's inner surface. The material properties of VIP insulation used are given in Table 5.2.

This simulation setup including VIP insulation is referred to as PUR+VIP in the following.

5.3.3 Integration of a Latent Heat Storage

The LHS is 2.00 m × 1.40 m × 0.06 m (l×w×h) in size and filled with 95.4 kg of PCM made from an eutectic mixture of water and sodium chloride with a salt mass fraction of 23.3 %, a melting temperature of −21 °C and latent heat of 233 kJ/kg (Han et al. 2006). With a total cooling power of 6.175 kWh, its size and mass are designed to provide the required refrigeration capacity for an eight hour long-distance transport following the DIN 8959 including a 75 % ATP safety factor. The LHS is not permanently integrated into the cooling structure, but is designed using individual modules and can therefore be used and exchanged very flexibly. Thus, in practice, either pre-cooling of the PCM in an external

cooling chamber or crystallization within the truck with a cooling unit is possible.

This enables a straightforward implementation of the LHS into the simulation by assuming the PCM to constantly have the melting temperature. The LHS is mounted in the refrigerated body's interior, 0.05 m under the ceiling and centered in x and z direction.

This simulation setup including VIP insulation and the LHS is referred to as PUR+VIP+LHS in the following.

5.4 Results and Discussion

In this section, the results of the proposed concepts and applications are presented. Section 5.4.1 shows the investigations on an improvement of the wall insulation through a partly exchange with VIPs. Additionally, an application on the leakage of a cooler box door is shown and discussed. In Section 5.4.2 the exchange of the AC system is introduced, as well as the influence of this replacement on the flow and temperature fields in a loaded vehicle. Eventually, the sensitivity of the loading temperature for differently isolated refrigerated bodies is discussed, taking into account switching off the AC.

5.4.1 Concecpt A – Insulation Optimization using Vacuum Insulation Panels (VIP)

5.4.1.1 Comparison of the Insulation Effect

The ingoing heat flux through the walls of the cooled box is an important measurement in order to compare different insulation materials applied in a refrigerated vehicle's wall. It is possible to calculate the spatial heat transfer in normal direction through the walls for every grid point by resolving the insulation walls as a structure of specific material. In order to compare the heat fluxes, the resolved grid with PUR and PUR+VIP insulation is given in Figure 5.3. The flow fields from the simulations with and without VIP show a nearly identical velocity distribution as in Gaedtke et al. (2018c, Figure 11), which is why no illustration is given here.

Figure 5.3 (left) shows high differences between the edges of the refrigerated body with $Q = 0\,\mathrm{W}$ to $4\,\mathrm{W}$ and the surfaces with $Q = 10\,\mathrm{W}$ to $13.6\,\mathrm{W}$. The heat flow through the insulation walls is shown in the simulation. Furthermore, the differences in the wall thicknesses are recognizable, since the side

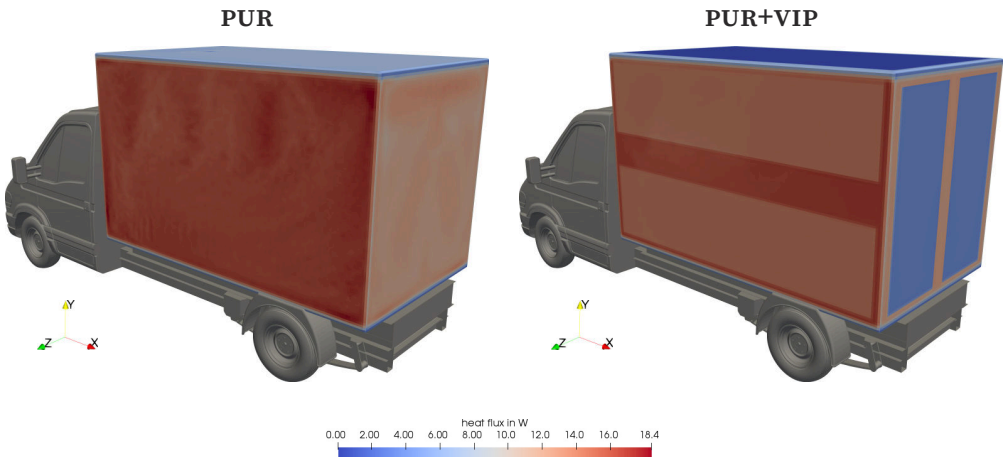

Figure 5.3: *Heat flux in wall normal-direction through the* PUR *insulation (left) and through the* PUR+VIP *insulation (right).*

walls with their smaller thickness, in contrast to the ceiling and front, allow for a higher heat flow.

Figure 5.3 (right) shows the heat flow chart for simulation case with VIPs. The reduced ingoing heat flow of the area of the VIPs is clearly visible, which has dropped from $Q = 10\,\mathrm{W}$ to $13.6\,\mathrm{W}$ to $Q = 0\,\mathrm{W}$ to $5\,\mathrm{W}$. In addition, it becomes apparent that with the help of the new insulation concept, hardly any heat penetrates into the refrigerator car via the ceiling, even at the edges to other walls, whereas the heat flow via the rigid foam insulation of the side wall has maximum values of up to $Q = 13.6\,\mathrm{W}$.

With the help of Nusselt correlations from the VDI Heat Atlas, a rough expectation for the total heat flux was calculated. For this purpose, a correlation for the overflow of planar surfaces is used for interior space on all internal walls separately and averagely as seen in Gaedtke et al. (2018c). For each wall, a specific mean Reynolds number is calculated, using the velocities from the validation case in Gaedtke et al. (2018c). For the PUR insulation a total incoming heat flow of $Q = 470\,\mathrm{W}$ and for PUR+VIP an incoming heat influx through the wall of $Q = 274\,\mathrm{W}$ is determined by the correlations. The simulated heat flux through the wall sums up to $Q = 458\,\mathrm{W}$ for the PUR and $Q = 248\,\mathrm{W}$ for the PUR+VIP insulation, respectively. Thus, the relative deviations from the Nusselt correlation is around 2.6 % and 9.5 %, respectively.

The variation of the insulation material changes the incoming heat flux in

the proposed set-up of more than 54.15 %. This leads to a significant reduction in the cooling energy consumed, which considerably improves the operating costs of the truck and facilitates the provision of the complete cooling energy for a one-day delivery cycle through an LHS system. This is investigated numerically in Section 5.4.2.1.

5.4.1.2 Influence of Leakage in the Rear Door

One of the possible leakage positions in a refrigeration structure is the tailgate insulation due to its mechanical stress by opening and closing. Leakage in technical systems describes the undesired entry or exit of solids, liquids or gases (Ross-Jones et al. 2019). In the event of the leakage of a refrigerated transporter, cooled indoor air could leave the isolated space and warmer outside air could penetrate into the structure. This would cause a loss of cooling energy depending on the size of leakage a high degree of cooling performance of the AC to the environment. With the chilled airflow impinging at high speed at the top of the door, additional performance losses are expected in comparison with leaks in areas of lower velocity. In order to analyze a door leakage an exemplary outflow opening of $l_{z,\mathrm{leak}} = 0.0125\,\mathrm{m}$ width and $l_{y,\mathrm{leak}} = 1.92\,\mathrm{m}$ height is provided at the closing seam of the tailgate at position $z = \frac{l_z}{2}$. This corresponds to a total leakage area of $A_{\mathrm{leak}} = 0.024\,\mathrm{m}^2$.

The resulting velocity field in the leakage area is shown in Figure 5.4. As expected, a significantly higher outflow velocity in the upper part of the door than in the remaining opening is predicted by the simulation. In comparison, however, in a section of the refrigerated body at position $z = \frac{l_z}{2}$ no increased outflow velocity in the x-direction can be determined. The heat flow entering the refrigerated body is determined by means of a time averaged volumetric flow within the simulation. In order to avoid a measurement of the inlet state, the volumetric flow measurement starts after a physical time of one minute and the calculated heat flow is averaged over a time of one minute, while ensembles are recorded every five seconds.

The simulation results in an average heat flow of $Q_{\mathrm{leak}} = (545 \pm 29)\,\mathrm{W}$ entering the cooling transporter via the modeled leakage. The fluctuations are caused by the different volume flow rates, which are themselves caused by the turbulence of the flow. Within the measuring time of one minute maximum and minimum incoming heat flow are $Q_{\mathrm{leak,max}} = 606.5\,\mathrm{W}$ and $Q_{\mathrm{leak,min}} = 487.6\,\mathrm{W}$.

A leakage of this size represents a considerable contribution to the loss of

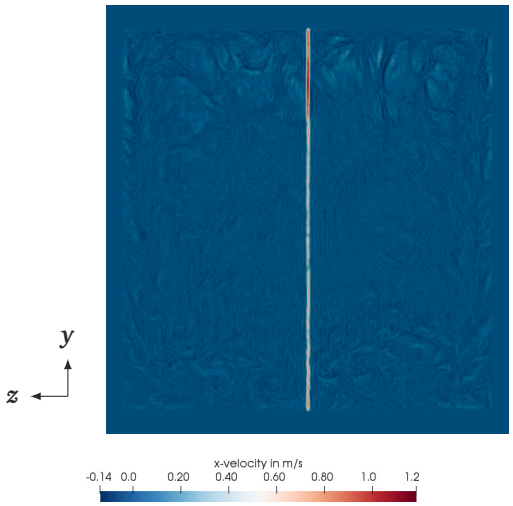

Figure 5.4: *Distribution of the velocity's x component near the rear wall with leakage through rear door, slice in the y-z-plane.*

power and exceeds the loss of cooling capacity via the simulated rigid foam insulation. Taken together with the simultaneous heat loss via the rigid foam insulation, theoretically more than the cooling capacity of the air-conditioning system would be lost to the environment, which implies continuous operation of the air-conditioning system under full load. The interior of the refrigerated body would heat up over a longer period of time, as the heat flow cannot be compensated completly. This would lead to considerable fuel costs, high carbon dioxide emissions and eventually spoilage of the goods and must be avoided urgently in practice.

5.4.2 Concecpt B – Passivation of the Cooling Effect by Latent Heat Storage (LHS)

5.4.2.1 Influence of Passive Cooling on Flow Field and Loading Temperatures

Given that the maximum temperature of the chilled goods after 60 s cooling under full load is a useful measure of the quality for the cooling performance, it is worth to analyze this criterion numerically and apply it to the presented concepts. For this purpose six grid trolleys with deep-frozen goods are included in the simulation. The assumed refrigerated cargo is deep-frozen food, which is modeled by the material values of pure ice given in the VDI Heat Atlas with a

thermal conductivity of $\lambda = 512.6 \times 10^{-3}\,\mathrm{W/(m\,K)}$, a density of $\rho = 993.6\,\mathrm{kg/m^3}$ and a specific heat capacity of $c_p = 4401\,\mathrm{J/(kg\,K)}$. The goods are stacked virtually on a grid trolley, which dimensions are given with 0.72 m × 0.81 m × 1.62 m (l×w×h). In addition, a gap width of 0.05 m between the trolleys is kept for load securing and a gap width of 0.12 m is kept at the bottom due to the rolls (not resolved here). Since the underside of the AC must be kept clear of cargo in order to properly suck in indoor air, a distance of 0.60 m is recommended between the inside front wall and the closest trolley.

Figure 5.5 shows the flow of the internal air around these chilled cargo by means of streamlines and with regular PUR insulation, where significant differences to the flow of the empty refrigerated body become visible, compare in particular Figure 11 in Gaedtke et al. (2018c). The flow field in Figure 5.5 is comparable to that of an empty refrigerated body up to just below the body's rear edge. The average velocity drops from 2.90 m/s to less than 1.45 m/s. There is also an all-round flow both under the trolleys and between the side walls and the trolleys. The diversion of part of the flow into the central channel between the trolleys can also be observed. Comparatively low air movement can be detected for the air in the vertical spaces between the cargoes, while the formation of temperature inhomogeneities in these spaces is mostly avoided in spite of high flow rate around the cargo.

Figure 5.6 shows streamlines of the convection generated by the air conditioning system with VIP. When compared against the case of PUR insulation shown in Figure 5.5, a more uniform and cooler surface temperature of the chilled goods is achieved in the VIP insulation case. This clearly shows an advantage of the new insulation concept. The case with LHS was simulated with a quarter of the volume flow of the AC system and without active cooling. This case is shown in Figure 5.7. In comparison with Figure 5.6, a good flow around the refrigerated goods is ensured even with only a quarter AC power.

The cargo's internal temperature distributions are shown in Figure 5.8 for all three cases by means of isotemperature contours. With a minimum and maximum temperature of 253.15 K to 254.65 K, the PUR insulation results in the largest temperature variation of 1.5 K, while the PUR+VIP and the LHS cases show temperature variations of 0.26 K and 0.66 K. Figure 5.8 (left) illustrates much larger inhomogeneities of the cargo's temperature distribution with PUR insulation compared to the two VIP insulation cases, while the reduced AC flow of the LHS case (Figure 5.8 right) results in slightly higher inhomogeneity than in the PUR+VIP case. Particularly in the case of PUR+VIP insulation (Figure 5.8 mid), the locally different cooling effect can be detected, where the coolest tem-

Figure 5.5: *Streamline representation of the simulated air flow inside the refrigerated vehicle including surfaces temperatures of the loading with* PUR *insulation.*

Figure 5.6: *Streamline representation of the simulated air flow inside the refrigerated vehicle including surfaces temperatures of the loading for the simulation case* PUR+VIP.

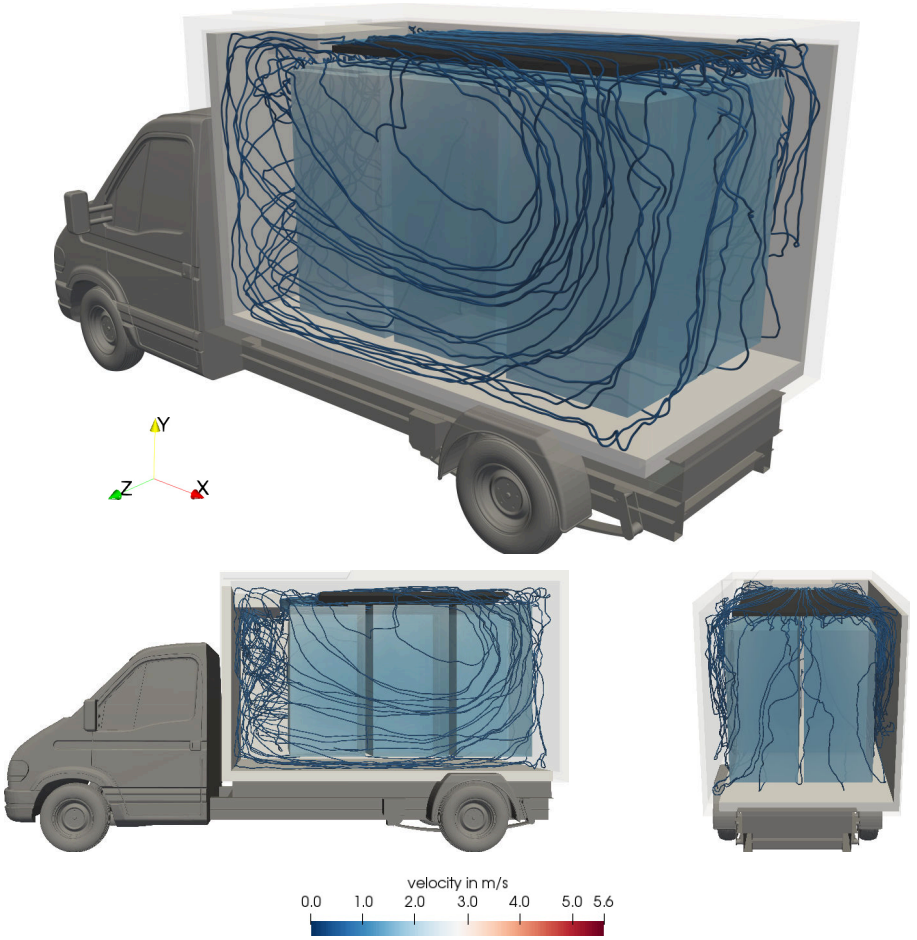

Figure 5.7: *Streamline representation of the simulated air flow inside the refrigerated vehicle including surfaces temperatures of the loading for the simulation case* PUR+VIP+LHS.

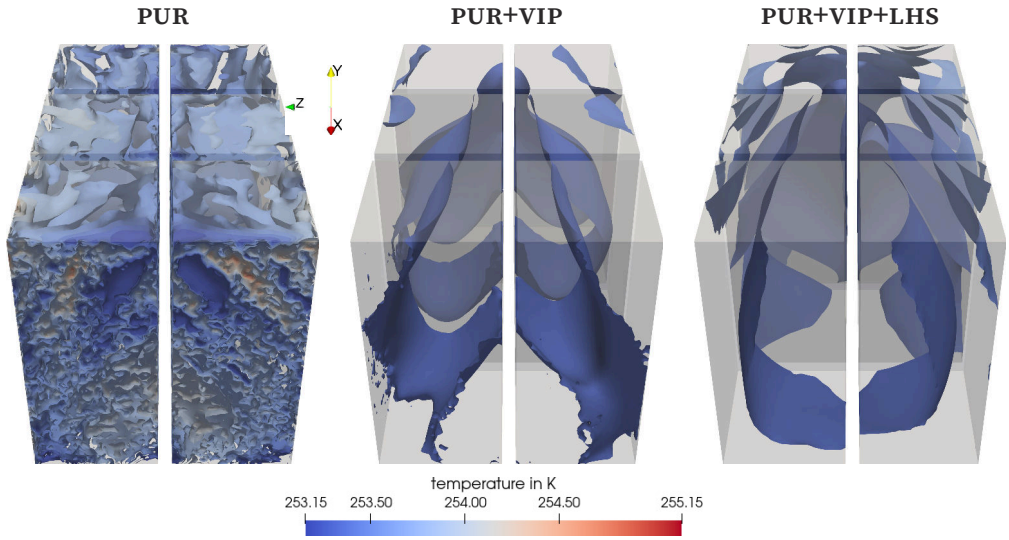

Figure 5.8: *Isotemperature contours every* 0.1 K *between* 253.15 *and* 255.15 K *of the simulated loading with* PUR *insulation (left), with* PUR+VIP *insulation (mid) and with* PUR+VIP *insulation and* LHS *(right). The two rear trolleys are shown at the bottom, the two front trolley are shown at the top, respectively, and the view point is from above.*

perature follows the surrounding flow (compare Figure 5.6 bottom right). This is also visible for the LHS case, which directly recommends the use of an active flow. However, while a relatively narrow outlet of the AC system is used here, ventilation across the entire width of the refrigerated body seems to make sense for a more even flow around the LHS and thus also around the chilled goods. The surface temperature of the chilled goods is still competitively uniform and cold as the PUR+VIP case, which is a very good result, measured by the fact that only passive cooling was provided.

5.4.2.2 Influence of Switching Off the Air Conditioning

When the AC system switches off, the refrigerated body is no longer provided with cooling capacity, but heat continues to penetrate into the volume through the walls. After a certain time, the first temperature gradients begin to appear in the inside air and in the cargo. As a starting point for these simulations, flow and temperature fields after 60 s of air conditioning under full load are used as initial distributions. The AC is then deactivated and a maximum simulation

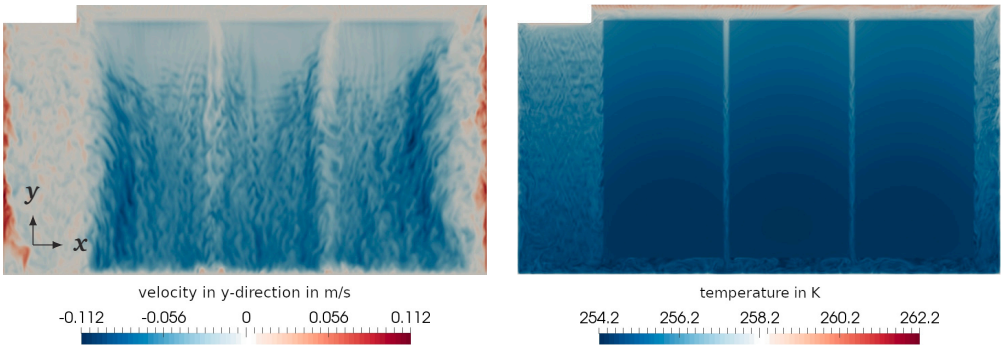

Figure 5.9: *Distribution of the velocity's y-component and the temperature after shutdown of the cooling unit at the mid of the truck, in the middle gab between the trolleys, slice in the x-y-plane.*

time of 11 min is set.

Figure 5.9 (left) shows a slice through the velocity field in y-direction at $y = \frac{l_y}{2}$ to demonstrate the flow in the middle channel, while Figure 5.9 (right) shows the corresponding temperature field on the same slice to demonstrate temperature differences in the load after a physical time of $t = 4\,\text{min}$. The onset of turbulent natural convection is clearly visible. Air rises along the inner walls of the refrigerated body and reaches velocities of over 0.1 m/s, whereas the air in the gap between the cooling containers sinks by up to 0.1 m/s. The air in the gap between the cooling containers is then cooled down and sinks by up to 0.1 m/s. The temperature field of the air shows a stratification: warm air collects in the ceiling area of the refrigerated body and cooler air drops towards the floor. The Rayleigh number of the formed natural convection can be determined to $\text{Ra} = 3.45 \times 10^9$.

For comparison, the simulations are carried out for the setups PUR, PUR+VIP and PUR+VIP+LHS. The three configurations are compared in Figure 5.10 on the basis of the maximum cooling temperature occurring over time.

It can be seen for both insulation concepts, that the increase in cargo temperature already starts after $t = 10\,\text{s}$, with an approximately linear increase in the maximum cargo temperature. The upper limit temperature of the cold chain is already exceeded after $t = 3.33\,\text{min}$ with the pure rigid foam insulation. The use and sale of the warmed up frozen goods would be prohibited. In contrast, the new insulation concept with integrated VIPs reduce the incline

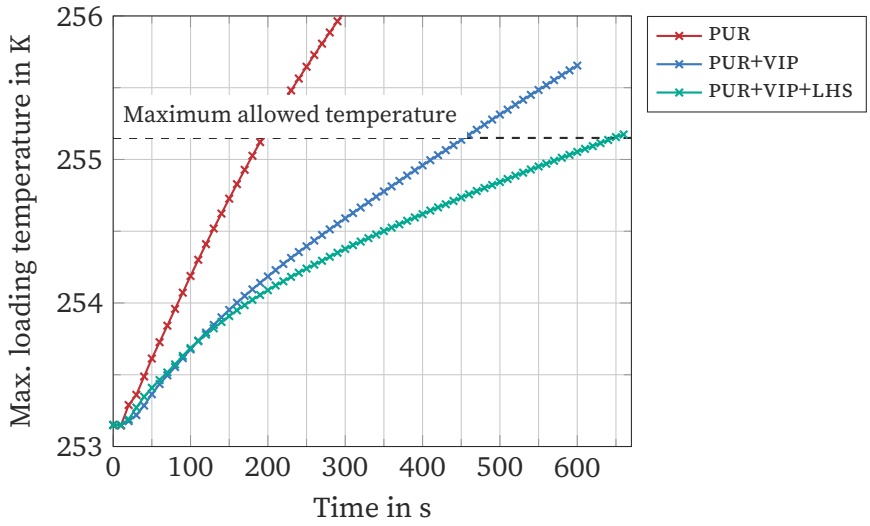

Figure 5.10: *Loading temperature over time for the three simulation cases* PUR, PUR+VIP, PUR+VIP+LHS.

of the cargo temperature effectively. The time after which the good's temperature exceeds the cooling limit temperature for the new insulation concept is $t = 7.66\,\text{min}$. A further increase in this duration can be achieved by installing the LHS on the ceiling: As shown in Figure 5.10 the cooling limit temperature is exceeded after $650\,\text{s} \approx 11\,\text{min}$ in the LHS case.

5.5 Conclusion

In this paper, two innovative concepts for an improved refrigerated vehicle are numerically investigated – an improved insulation combined of polyurethane hard foam and VIPs and the application of an LHS in the refrigerated body. Both concepts are simulated with the double distribution thermal Lattice Boltzmann Method including spatially and transient conjugate heat transfer resolving the insulation walls and the deep frozen cargo.

Based on our simulations the key findings of this study are summarized as follows:

- A homogenized and highly reduced ingoing heat flux is found for the combined PUR and VIP insulation material case compared to pure PUR

insulation. The present concept of VIP inclusion is found capable of halving the required cooling energy.

- The VIP inclusion is further found to enable the AC system to be replaced by an LHS mounted near the top of the refrigerator body and an additional ventilation system of lower total capacity, for which a configuration and an inclusion concept is presented in Section 5.4.2.
- In order to assure a homogeneous temperature in the cargo during operation, a slight flow around the refrigerated goods is found to be necessary by considering the temperature homogeneity of deep frozen food products loaded in the refrigerated body.
- In addition, the maximum downtime of the AC system is determined to about 8 min in case of PUR+VIP insulation and to 11 min in case of an additional LHS.

Thus, this study shows that the evaluated concepts are promising and that the LES-LBM approach offers a good analysis tool providing helpful insights for the design of a prototype including both concepts to reduce the fuel consumption. In cooperation with the medium-sized company *Kress Fahrzeugbau GmbH* as part of the research project ZF4005102CL5 funded by the *Central Innovation Program for* SMEs, these concepts and their practical implementation are being pursued. We look forward to presenting corresponding results in a future contribution.

6

Total Enthalpy-Based Lattice Boltzmann Simulations of Melting in Paraffin/Metal Foam Composite Phase Change Materials

Phase change materials (PCM) have become a popular choice for building thermal management due to their low cost, chemical stability and high energy density. Though, their low thermal conductivity is a limiting factor in their use. To overcome this limitation, there has been considerable interest in the application of highly conductive substrates such as metal foams. These offer a potential to increase the thermal performance of PCM and to broaden their area of application. However, the influence of micro structured properties on melting is not completely understood and difficult to explore experimentally.

In this study, a lattice Boltzmann method (LBM) based on the two relaxation time (TRT) collision scheme for the simulation of melting and conjugate heat transfer is proposed, validated and applied to melting in three-dimensional (3D) structures of composite PCM-metal foam latent heat storages. The model and its implementation is validated against the analytical transient solution of the Stefan problem, proving superlinear grid convergence and close agreement for a large range of lattice relaxation times and Stefan numbers. The interfacial diffusion is found to be effectively limited by leveraging a TRT collision scheme. Very close accordance to measurements and simulation results obtained with other methods is shown for the vali-

dation case of melting gallium including natural convection in 2D and 3D. Subsequently, the melting of paraffin in two complex metal foam geometries is simulated. The present simulations successfully describe the multi-domain heat transfer in 3D, where the thermal conductivity of the foam is more than 1000 times larger than that of the paraffin. The predicted progression of the melting front and the influence of the different foam's specific surface area are in close agreement to earlier simulations.

This chapter corresponds to the work of the same title published in the journal *International Journal of Heat and Mass Transfer* (Gaedtke et al. 2020a). Following the contributor roles taxonomy (Brand et al. 2015), my contribution to this publication includes conceptualization, methodology, software, validation, investigation, writing – original draft, visualization and funding acquisition.

6.1 Introduction

The need for energy sustainability has led to a great deal of research towards development of efficient energy storage systems. Mahlia et al. (2014) discuss various types of storages including (flow) battery energy storage, synthetic fuels, and thermal energy storage. Thermal energy storages have become an especially important component of renewable and waste heat energy technologies (Spoletini 2016; Mumtaz et al. 2017). They are particularly advantageous in systems that have intermittent (chemical or manufacturing processes, electric vehicle battery operations) or transient and cyclic thermal loading (solar loads on buildings, refrigerated vehicles), where the energy requirement for heating or cooling can be offset by storing the excess heat and releasing it during appropriate demand (Zalba et al. 2003; Baetens et al. 2010a; Gaedtke et al. 2020c). Thermal energy storage is typically accomplished by systems employing materials with high specific heat capacity or through the process of melting and solidification. Phase change materials (PCM) such as paraffins or salt hydrates have been found to be excellent candidates for such applications due to their high latent heats of fusion, chemical stability, availability over a wide range of temperatures and low cost (Farid et al. 2004; Kasaeian et al. 2017). The appropriate selection of material allows the application of PCMs over a range of temperatures. However, these advantages are often offset by their poor thermal conductivities that limit their use in applications requiring precise rates of heating or cooling, such as for accurate temperature control in process engi-

neering, and thermal management of electronics and batteries.

Several studies have looked into the possibility of controlling the melting or solidification rates using porous media filled with PCM in a composite matrix (see Fan and Khodadadi 2011; L. Liu et al. 2016; R. Singh et al. 2019, for an overview and references within). This involves substrates of varying macroscopic properties (porosity and isotropy) micro structure or materials (copper, aluminum, carbon, ceramics) and thermophysical properties. Highly open (porosity $> 90\,\%$) PCM filled metal-composites have substantially greater effective thermal conductivities as compared to pure PCMs, and have been shown to increase the melting or solidification rates by 3 to 44 times (Thapa et al. 2014; Xiao et al. 2014), for a fractional increase in size. Several studies – Abishek et al. (2018), Drissi et al. (2019), and X. Yang et al. (2019) among others – have looked into optimizing the porous-PCM composites by varying the substrate material and other macroscopic properties of the porous media such as packing density. In a recent paper, Abishek et al. (2018) showed that the micro structural properties of the porous media (using open-cell foams) play a critical role in the melting and energy storage performance of metal-PCM composites. Using several foams with similar porosities and micro-structure (polydispersity, cell shapes, etc), it was shown that, the specific surface area of the substrate was one such parameter that can significantly control the melting rates of the PCM in the composite. Given the wide spectrum of potential substrate candidates, such as open-cell foams or fibrous structures that are also common in other thermal applications, it is important to fully understand the interstitial thermal and phase-change physics to enable truly optimal designs of PCM-composites for any application. This is particularly important, to ensure that the overall volume fraction of the PCM in the composite is maximized in any energy storage unit of a given size for maximal energy storage density, with optimal melting or solidification rates that are required for each application.

A limiting factor in the use of PCMs has been the low thermal conductivity of the matrix, which has typically been composed of calcium carbonate or cellulose (C. Y. Zhao 2012). While this may be useful if the PCM is also a cosmetic feature (e.g. cladding), this is sub-optimal for many other applications. For this reason, there has been considerable interest in highly conductive substrates, such as metal foams. These offer the potential to increase the thermal performance of PCMs and to broaden their areas of application. Recent work has explored the possibility of using modularized PCM units which could be swapped out once the phase change has completed (Shang et al. 2018). Efficient design optimization requires thorough knowledge of the influence of these mi-

cro structural properties on the melting and solidification processes, which inevitably play a central role in the performance of the energy storage system. The detailed study of such systems, however, is non-trivial, with localized phenomena difficult to characterize experimentally. Recent work by B. Yang et al. (2019) has measured and characterized the "mushy" zone within a PCM, though this required the use of confocal microscopy and therefore only considered a thin layer of material. Given the challenges faced by experiments, there is a clear rationale to apply numerical methods here.

Simulations using approximated homogeneous porous media approaches with thermal equilibrium or non-equilibrium assumptions are normally preferred for engineering design, but are not suitable to recover the geometrical influences observed here. Computational simulations on the pore scale, however, can aid characterizing the melting and solidification processes with isolated variations in governing micro structural properties. There is a growing body of work in this area and the suitability of computational fluid dynamics in this application has been clearly demonstrated (M. Wang et al. 2009; Alshaer et al. 2015; C. Chen et al. 2016; Abishek et al. 2018; Y. Xu et al. 2018). In a recent study, Abishek et al. (2017) provided a computational tool for generating realistic porous media, involving open-cell foam, fibrous or knitted structures with customizable micro structural properties (the technique that is used in this study for generating the porous structures). This has allowed a range of parameters to be tested in Abishek et al. (2018) and an exploration the optimization the configuration of metal foams to be performed (Y. Xu et al. 2018). While resolved simulations of melting in metal foams are possible, creating high quality meshes is demanding due to the complex geometry (M. Wang and N. Pan 2008; Li et al. 2014a). This is especially true for conjugated heat transfer, which often requires matching grids for the respective material domains. In view of the computational scalability and parallel performance on such meshes, optimal decomposition and load balancing of multiple meshes pose additional challenges. This usually limits the efficient use of a large number of cores of processors on a machine or high performance computing (HPC) system for this application and leads to very long run times.

In order to address these difficulties, this study examines the suitability of a Lattice Boltzmann Method-based (LBM) solver. The LBM has previously been shown to be suitable for high-performance simulations in complex geometries due to its ease of parallelization and the use of simple structured grids (Feichtinger et al. 2009; Xian and Takayuki 2011; Lin et al. 2013; A. Xu et al. 2017). In particular, the LBM has been applied to simulations of resolved porous struc-

tures and conjugate heat transfer, demonstrating its suitability for these applications, see e.g. C. Pan et al. (2004), M. Wang and N. Pan (2008), and Ross-Jones et al. (2019) among others.

Thus, it seems reasonable to investigate the suitability of the LBM also for the simulation of resolved composite PCMs. While LB models for the simulation of the melting process were proposed, these have so far mostly been applied to simulations in 2D – see He et al. (2019) for an overview. First microscopic modeling of melting by means of LBM has been presented in De Fabritiis et al. (1998) with a one dimensional model. Jiaung et al. (2001) and Chatterjee and Chakraborty (2005) later proposed an enthalpy-based method, which needs an iterative solution procedure within each time step. Later R. Huang et al. (2013) presented an LBM based on the transport equation for the total enthalpy. They eliminate the iterative procedure by introducing an arbitrary reference heat capacity in the equilibrium term of the algorithm. With special consideration of the interfacial effects, it could be shown that the commonly used Bhatnagar-Gross-Krook (BGK) collision operator introduces numerical diffusion near the phase interface (R. Huang and Wu 2015). R. Huang and Wu (2015) have therefore proposed a special multi relaxation time (MRT) collision that effectively limits numerical diffusion. Ren et al. (2018) implemented this method on GPUs to investigate the PCM melting process in a latent heat storage unit enhanced with metal foams in two-dimensional simulation domains. Very recently, Lu et al. (2019) have presented a model for solving the total enthalpy method based on an optimally two relaxation time (TRT) collision operator that also limits numerical diffusion near the interface. Compared to MRT, this model is both, easy to implement and trivial to apply to 3D. To the authors' knowledge, this has so far only been applied to simple problems in cubic geometries (Chatterjee and Chakraborty 2005; Hu et al. 2017; Zhu et al. 2017; Q. Liu et al. 2019). This application of such an LBM algorithm to the simulation of melting in a complex geometry including conjugated heat transfer to a three-dimensional metal foam is as yet, unavailable – this is also one of the motivations for the present work.

The next sections of this study are structured as follows. The governing equations for the melting problem and fluid flow are formulated in Section 6.2.2, followed by the LBM for the enthalpy equation and the fluid flow in Section 6.2.3. In Section 6.3 this model and its implementation is validated against the analytical solution of the Stefan problem in Section 6.3.1 and the melting of pure gallium in Section 6.3.2. Subsequently, simulations of composite latent heat storages are carried out as described in Section 6.4. Special

attention is given to the mesh generation procedure and resulting mesh quality in Section 6.4.2. The results of transient melting simulations are compared against earlier studies' findings in Section 6.4.3. Finally, a discussion and conclusion is given in Section 6.5.

6.2 Methodology

In this work the double distribution thermal LBM (DDT-LBM) is applied. By employing the total enthalpy equation, the model is capable of describing the phase transition from solid to liquid. The respective macroscopic target equations are briefly introduced in the following Section 6.2.1. For solving these with an LB algorithm, two distribution functions g_i and f_i are introduced in Sections 6.2.2 and 6.2.3, respectively.

Note that the Lattice Boltzmann Equations (LBE) presented in the following are solved in their non-dimensional form. Hence, all physical quantities are converted into so-called *lattice units* prior to simulation and reconverted before post-processing. Krüger et al. (2017) give an overview of the dimensioning of the LBE in chapter 7.

6.2.1 Governing equations

The fluid is considered to be a weakly compressible Newtonian fluid and can thus be described by the Navier-Stokes equation (NSE) and the Advection-diffusion equation (ADE) for the enthalpy H as follows

$$\frac{\partial \rho}{\partial t} + \boldsymbol{\nabla} \cdot (\rho \boldsymbol{u}) = 0 \,, \tag{6.1}$$

$$\frac{\partial (\rho \boldsymbol{u})}{\partial t} + \boldsymbol{\nabla} \cdot (\rho \boldsymbol{u}\boldsymbol{u}) = -\boldsymbol{\nabla} p + \boldsymbol{\nabla} \cdot (\nu \boldsymbol{\nabla} \boldsymbol{u}) + \boldsymbol{F} \,, \tag{6.2}$$

$$\frac{\partial (\rho H)}{\partial t} = -\boldsymbol{\nabla} \cdot (\rho c_p T \boldsymbol{u}) + \boldsymbol{\nabla} \cdot (\lambda \boldsymbol{\nabla} T) \,, \tag{6.3}$$

where t denotes time and ρ, $\boldsymbol{u}$, p and T are the fluid's density, velocity, pressure and temperature, respectively. The constant viscosity and thermal conductivity are given by ν and λ. The buoyancy force $\boldsymbol{F}$ is given by the Boussinesq approximation with

$$\boldsymbol{F} = \rho \beta \boldsymbol{g} (T - T_{ref}) \,, \tag{6.4}$$

where T_{ref} is the reference temperature, β is the thermal expansion coefficient and $\boldsymbol{g}$ is the gravitational vector. For the enthalpy

$$H = c_p T + f_l L \tag{6.5}$$

further applies with c_p, f_l and L being the specific heat capacity at constant pressure, liquid fraction and the latent heat, respectively.

6.2.2 Lattice Boltzmann Method for the enthalpy equation

In order to solve (6.3) numerically, the enthalpy-based LBM has been proposed by R. Huang et al. (2013) and R. Huang and Wu (2015) for which the particle distribution function g_i is given with

$$g_i(\boldsymbol{x} + \boldsymbol{c_i}\Delta t, t + \Delta t) = g_i(\boldsymbol{x}, t) - \frac{\Delta t}{\tau_g}\left(g_i(\boldsymbol{x}, t) - g_i^{eq}(\boldsymbol{x}, t)\right), \tag{6.6}$$

where i is the discrete direction, $\boldsymbol{c_i}$ the discrete velocity in direction i, the relaxation time $\tau_g = \frac{\alpha}{c_s^2} + \frac{1}{2}\Delta t$ as a function of thermal diffusivity $\alpha = \frac{\lambda}{\rho_0 c_{p,ref}}$ with the the speed of sound c_s. The equilibrium distribution function is given by

$$g_i^{eq} = \begin{cases} H - c_{p,ref} T + \omega_i c_p T \left(\dfrac{c_{p,ref}}{c_p} - \dfrac{\boldsymbol{u}\cdot\boldsymbol{u}}{2c_s^2} \right) & i = 0 \\ \omega_i c_p T \left(\dfrac{c_{p,ref}}{c_p} + \dfrac{\boldsymbol{u}\cdot\boldsymbol{c_i}}{c_s^2} + \dfrac{(\boldsymbol{u}\cdot\boldsymbol{c_i})^2}{2c_s^4} - \dfrac{\boldsymbol{u}\cdot\boldsymbol{u}}{2c_s^2} \right) & i \neq 0 \end{cases} \tag{6.7}$$

where the discrete weights ω_i, the discrete velocities $\boldsymbol{c_i}$ and the speed of sound c_s are given by the standard D2Q5 and D3Q7 velocity sets (Krüger et al. 2017) for 2D and 3D simulations, respectively.

The enthalpy is then calculated from the zero$^{\text{th}}$ moment of g_i with

$$H = \sum_i g_i(\boldsymbol{x}, t)\,. \tag{6.8}$$

From that, the temperature T and liquid fraction f_l are obtained by

$$T = \begin{cases} T_s - \dfrac{H_s - H}{c_{p,s}} & H < H_s \\ \dfrac{H_l - H}{H_l - H_s} T_s + \dfrac{H - H_s}{H_l - H_s} T_l & H_s \leq H \leq H_l \\ T_l + \dfrac{H - H_l}{c_{p,l}} & H > H_l \end{cases}, \tag{6.9}$$

$$f_l = \begin{cases} 0 & H < H_s \\ \dfrac{H - H_s}{H_l - H_s} & H_s \leq H \leq H_l \\ 1 & H > H_l \end{cases}, \tag{6.10}$$

with the enthalpy at solidus temperature T_s and liquidus temperature T_l respectively given by H_s and H_l. With the thermal conductivities λ_s and λ_l as well as the specific heat capacities $c_{p,s}$ and $c_{p,l}$, respectively given for solid and liquid phase, the thermophysical properties are calculated as a function of the liquid fraction with

$$\lambda = (1 - f_l)\lambda_s + f_l \lambda_l \,, \tag{6.11}$$

$$c_p = (1 - f_l)c_{p,s} + f_l c_{p,l} \,. \tag{6.12}$$

For the sake of numerical stability (R. Huang and Wu 2015), the reference specific heat capacity is chosen as

$$c_{p,ref} = \frac{2 c_{p,s} c_{p,l}}{c_{p,s} + c_{p,l}} \,. \tag{6.13}$$

As shown by R. Huang and Wu (2015) this Lattice Boltzmann (LB) model based on the single relaxation time (SRT, also known as BGK) collision operator suffers from numerical diffusion across the phase interface. In R. Huang and Wu (2015) a model based on a specialized multi relaxation time (MRT) collision operator is proposed for two-dimensional simulations and shown to limit the numerical diffusion. MRT-based models are not trivially adapted to three-dimensional simulations, thus we propose a collision model based on two relaxation times (TRT), which not only enables 2D and 3D simulations but is also simple to implement and computationally efficient.

The particle distribution function in the case of TRT collision is given by

$$\begin{aligned} g_i(\boldsymbol{x}+\boldsymbol{c_i}\Delta t, t+\Delta t) = g_i(\boldsymbol{x},t) \\ -\frac{\Delta t}{\tau_g^+}\left(g_i^+(\boldsymbol{x},t)-g_i^{eq+}(\boldsymbol{x},t)\right) \\ -\frac{\Delta t}{\tau_g^-}\left(g_i^-(\boldsymbol{x},t)-g_i^{eq-}(\boldsymbol{x},t)\right) \end{aligned} \tag{6.14}$$

with

$$g_i^+ = \frac{1}{2}(g_i + g_{\bar{i}})\,, \qquad g_i^- = \frac{1}{2}(g_i - g_{\bar{i}})\,, \tag{6.15}$$

$$g_i^{eq+} = \frac{1}{2}(g_i^{eq} + g_{\bar{i}}^{eq})\,, \qquad g_i^{eq-} = \frac{1}{2}(g_i^{eq} - g_{\bar{i}}^{eq})\,. \tag{6.16}$$

The two relaxation times are given through

$$\tau_g^- = \frac{\alpha}{c_s^2} + \frac{1}{2}\Delta t \quad \text{and} \quad \Lambda = \left(\frac{\tau_g^+}{\Delta t} - \frac{1}{2}\right)\left(\frac{\tau_g^-}{\Delta t} - \frac{1}{2}\right), \tag{6.17}$$

where the "magic parameter" $\Lambda = \frac{1}{4}$ is found to limit the numerical diffusion across the interface, which coincidences with recent findings of Lu et al. (2019).

6.2.3 Lattice Boltzmann Method for the fluid flow

In this work the partially saturated method (PSM) firstly proposed by Noble and Torczynski (1998) is adopted to deal with the transiently changing phase interface location. The particle distribution function f_i is given by

$$f_i(\boldsymbol{x}+\boldsymbol{c_i}\Delta t, t+\Delta t) = f_i(\boldsymbol{x},t) + B\Omega_i^s(\boldsymbol{x},t) + (1-B)\Omega_i^f(\boldsymbol{x},t) + F_i \tag{6.18}$$

with the weighting function $B(\boldsymbol{x},t)$

$$B(\boldsymbol{x},t) = \frac{(1-f_l(\boldsymbol{x},t))\left(\frac{\tau_f}{\Delta t}-\frac{1}{2}\right)}{f_l(\boldsymbol{x},t)+\left(\frac{\tau_f}{\Delta t}-\frac{1}{2}\right)}\,. \tag{6.19}$$

The solid collision operator $\Omega_i^s(\boldsymbol{x},t)$ is further given by

$$\Omega_i^s(\boldsymbol{x},t) = \left(f_i^{eq}(\rho,\boldsymbol{u_s}) - f_i(\boldsymbol{x},t)\right) + \left(1-\frac{\Delta t}{\tau_f}\right)\left(f_i(\boldsymbol{x},t) - f_i^{eq}(\rho,\boldsymbol{u})\right) \tag{6.20}$$

with solid velocity $\boldsymbol{u_s} = 0$, while the fluid collision operator $\Omega_i^f(\boldsymbol{x},t)$ is given by

$$\Omega_i^f(\boldsymbol{x},t) = \frac{\Delta t}{\tau_f}\left(f_i^{eq}(\rho_f,\boldsymbol{u}) - f_i(\boldsymbol{x},t)\right)\,. \tag{6.21}$$

The equilibrium distribution function f_i^{eq} is provided by

$$f_i^{eq} = \omega_i \rho \left(1 + \frac{\boldsymbol{u} \cdot \boldsymbol{c_i}}{c_s^2} + \frac{(\boldsymbol{u} \cdot \boldsymbol{c_i})^2}{2c_s^4} - \frac{\boldsymbol{u} \cdot \boldsymbol{u}}{2c_s^2} \right) \tag{6.22}$$

and the relaxation time τ_f is calculated from

$$\tau_f = \frac{\nu}{c_s^2} + \frac{1}{2}\Delta t \, . \tag{6.23}$$

The weights ω_i, the discrete velocities $\boldsymbol{c_i}$ and the speed of sound c_s are given by the standard D2Q9 and D3Q19 velocity sets (Krüger et al. 2017) for 2D and 3D simulations, respectively. The fluid's density ρ, pressure p and fluid velocity $\boldsymbol{u}$ are then calculated from

$$\rho(\boldsymbol{x}, t) = \frac{p}{c_s^2} = \sum_i f_i(\boldsymbol{x}, t) \, , \tag{6.24}$$

$$\boldsymbol{u}(\boldsymbol{x}, t) = \frac{1}{\rho} \sum_i \boldsymbol{c_i} f_i(\boldsymbol{x}, t) \, . \tag{6.25}$$

6.3 Validation

6.3.1 One dimensional melting – Stefan problem

In order to validate the present approach and its implementation into the open source LB framework OpenLB (Krause et al. 2020), we conduct a series of simulations of the Stefan problem. For this purpose, a medium is initialized at its melting temperature $T_m = T_s = T_l$, while the left hand side is set to a constant high temperature above the melting temperature $T_h > T_m$; the other boundaries are fully adiabatic. A schematic drawing of the simulation domain including boundary conditions is given in Figure 6.1. This classical one dimensional melting setup has been used to validate other approaches and codes – see Dutil et al. (2011) for an overview – because of its analytical solution (Solomon 1966) for $t > 0$: The location of the melting phase interface measured from the left hand wall is given by

$$X(t) = 2k\sqrt{\alpha t} \, , \tag{6.26}$$

from which the liquid fraction is deduced

$$f_l(x, t) = \begin{cases} 1 & 0 < x < X(t) \\ 0 & x > X(t) \end{cases} \, . \tag{6.27}$$

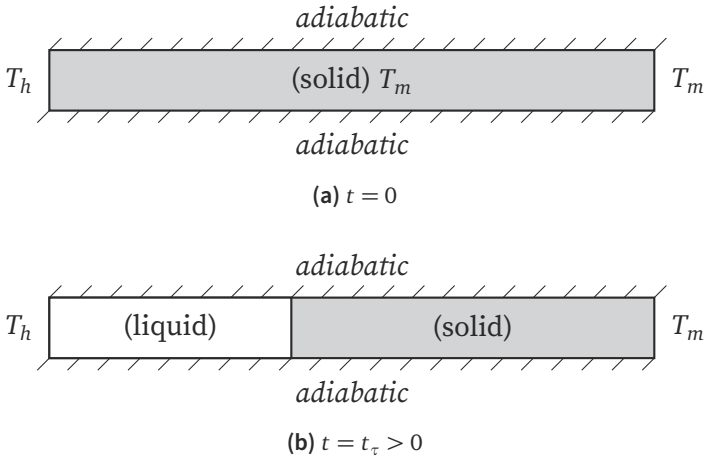

Figure 6.1: *Schematic representation of the simulation setup of the one dimensional Stefan melting including boundary conditions.*

The temperature T is given by

$$T(x,t) = \begin{cases} T_h - (T_h - T_m)\dfrac{\operatorname{erf}\left(\frac{xk}{X(t)}\right)}{\operatorname{erf}(k)} & 0 < x < X(t) \\ T_m & x > X(t) \end{cases} \tag{6.28}$$

with the thermal diffusivity $\alpha = \frac{\lambda}{\rho c_p}$. The parameter k is given as a function of the Stefan number

$$\mathrm{St} = \frac{c_p(T_h - T_m)}{L} \tag{6.29}$$

by the root of equation

$$\frac{\mathrm{St}}{\exp(k^2)\operatorname{erf}(k)} = k\sqrt{\pi}\,, \tag{6.30}$$

which is solved numerically using Brent's method (Brent 1971). Here, two-dimensional simulations with a resolution of $N = 64$, relaxation time $\tau_g = 0.6$, Stefan number $\mathrm{St} = 0.01$ are considered. The height of the domain is set to one eighth of the length, the vertical resolution consequently follows $N_v = \frac{N}{8}$. The cases are run until the melting interface position $X(t)$ reaches one fourth of the simulation domain, so with (6.26) it follows that $t_{max} = \frac{1}{\alpha}\left(\frac{0.25}{2k}\right)^2$. It should be noted that although only 2D simulations will be shown and discussed in the following, the results are equally valid for 3D, which will not be shown for the sake of brevity.

Figure 6.2 shows the results of a grid convergence study for the BGK and present TRT models with resolutions of the simulation domain – given by the amount of cells over the length of the domain in x-direction – from $N = 16$ to 512 and relaxation times $\tau_g = 0.6$ and 1.0. The global absolute error is calculated with the L^2-norm

$$E_{\phi,L^2} = \frac{1}{25}\frac{1}{X}\sum_{t_c=1}^{25}\sqrt{\sum_{x}|\phi(x,t_c)-\phi_a(x,t_c)|^2}\,, \tag{6.31}$$

where ϕ denotes the quantity of interest – either the liquid fraction f_l or the temperature T, and ϕ_a is the corresponding analytical solution given by either (6.27) or (6.28), the summation of x is over the whole grid with X being the total amount of cells. Since this is a transient problem, the error is also averaged over 25 evenly distributed time steps t_c. Additionally, the global absolute error is evaluated based on the L^∞-norm with

$$E_{\phi,L^\infty} = \frac{1}{25}\sum_{t_c=1}^{25}\max|\phi(x,t_c)-\phi_a(x,t_c)|\,. \tag{6.32}$$

Proper convergence can be seen for the L^2-norm errors in all cases considered regarding the liquid fraction as well as the temperature distribution. However, as stated by Lu et al. (2019), the expected convergence of the total enthalpy based LBM should be of order two. While the temperature is generally scaling with second order in the bulk region (see e.g. in Gaedtke et al. 2018c), it does not seem to scale close to the interface in this case, thus the reduced global experimental order of convergence $\mathrm{EOC}_T \approx 1.66$ and $\mathrm{EOC}_{f_l} \approx 1.03$. The maximum error always occurs for the cells in which the phase change takes place. The L^∞-norm displayed in Figure 6.2 shows that the error of the liquid fraction as well as the temperature for finer resolutions decreases, but is not of second order.

Further, comparing the global errors in the temperature field between the BGK and TRT models as shown in Figure 6.2, it can be seen that the BGK scheme gives larger deviation for $\tau = 0.6$ than for $\tau = 1.0$, while the errors are identical for TRT. This coincidences with the findings of R. Huang and Wu (2015) and Lu et al. (2019), where the BGK scheme is shown to suffer from artificial diffusion at the solid-liquid melt interface for $\tau \neq 1$.

To further evaluate the accuracy of the model in the vicinity of the melt front a comparison against results of Abishek et al. (2018) is carried out. Figure 6.3 shows the liquid fraction and Figure 6.4 shows the temperature over

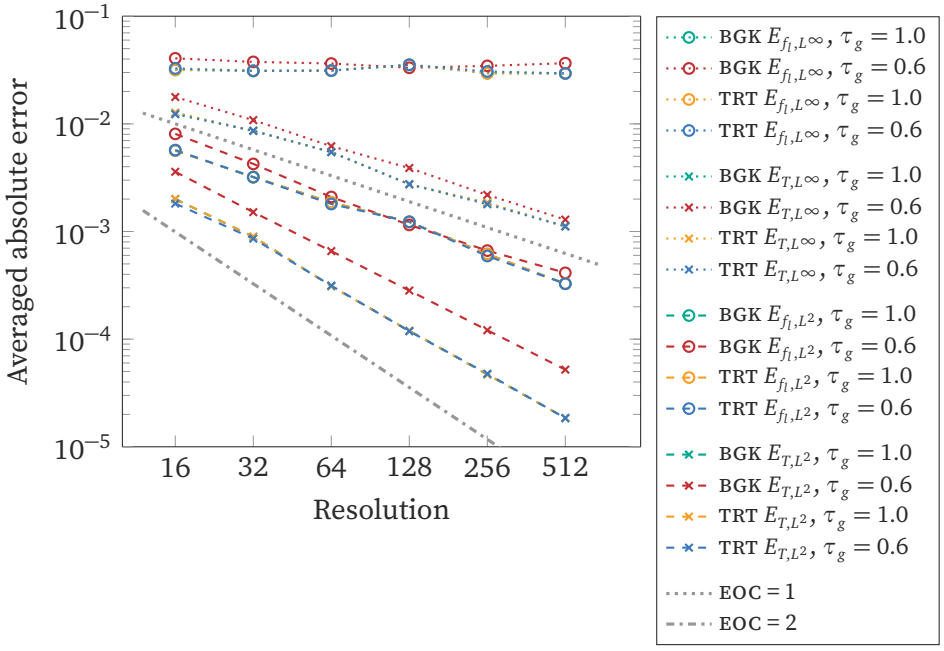

Figure 6.2: *Grid convergence study: Averaged absolute L^2-norm and L^∞-norm errors over resolution for the present* BGK *and* TRT *models and for $\tau_g = 1.0$ and $\tau_g = 0.6$.*

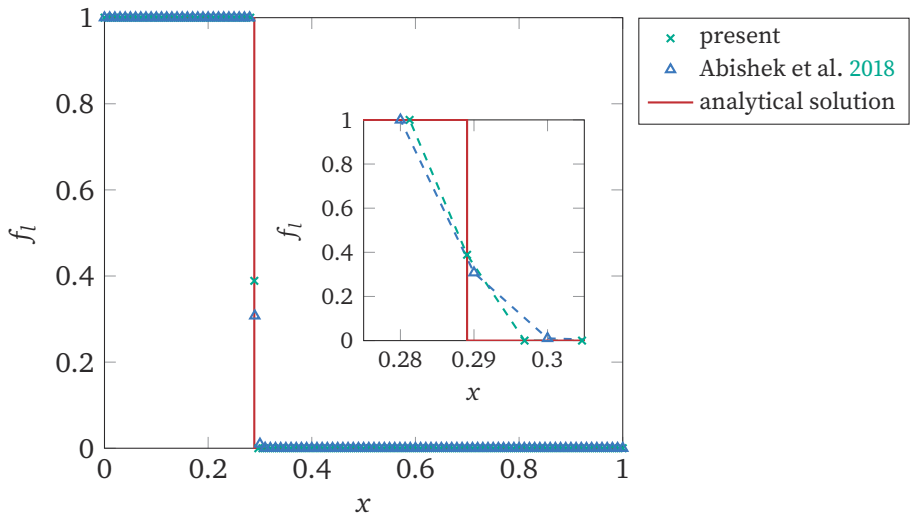

Figure 6.3: *Liquid fraction over x-position: Comparison of the interface's sharpness between the present* TRT *model, results from Abishek et al. (2018) and analytical solution.*

the distance from the hot wall x. The model's results are compared against the analytical solution as well as OPENFOAM simulations with the implementation explained in Abishek et al. (2018). Both methods are well able to capture the transient position of the interface and the temperature distributions are very close to the analytical solution. A detail of the domain of the interface is shown in the embedded plots in both figures highlighting the respective numerical diffusivity of each method, which seems to be slightly less for the present LBM approach.

Figure 6.5 (a) shows the global errors for several relaxation times τ_g. The BGK collision scheme results in a global minimum for the errors at $\tau_g = 1$, which is a consequence of truncation errors of the LBE (Holdych et al. 2004). By contrast, the present TRT model results in almost constant errors over the considered range. This has been indicated by R. Huang and Wu (2015) before, but it has not explicitly been demonstrated by means of spacial and temporal error norms. Figure 6.5 (b) presents the accuracy of the TRT model over a range of Stefan numbers from $\mathrm{St} = 10^{-3}$ to 1. It can be seen from the figure that the error in the global liquid fraction between the predictions and the analytical solution appears to be mostly independent from the Stefan number at $E_{f_l} \approx 0.01$, whereas the temperature error is lowest for $\mathrm{St} = 1$ with $E_T = 0.0009$ and converges to $E_T = 0.0022$ for smaller St.

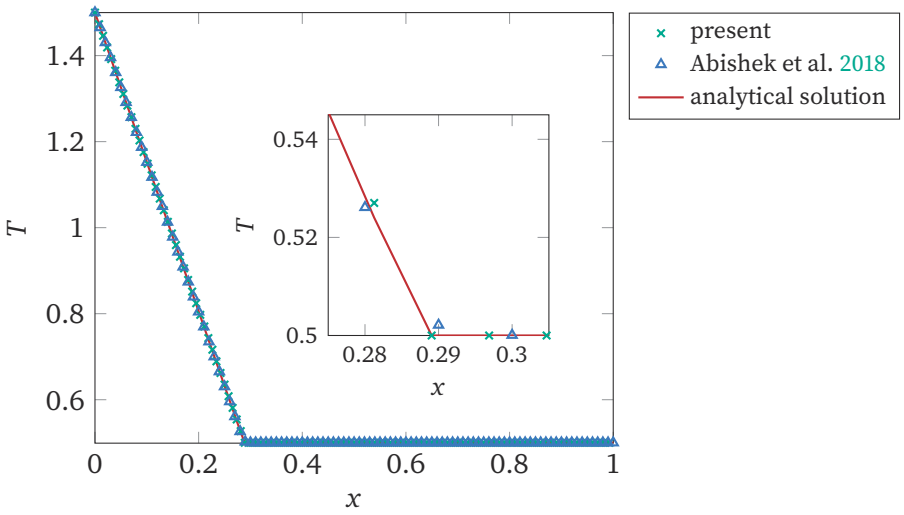

Figure 6.4: *Temperature over x-position: Comparison of the interface's sharpness between the present* TRT *model, results from Abishek et al. (2018) and analytical solution.*

Because of its superior accuracy due to limited numerical diffusion close to the melting interface, the TRT-based scheme is used for the remainder of this study.

6.3.2 Melting of gallium

The second case considered for validation in this study is the melting of pure gallium, for which a schematic representation of the simulation setup is given in Figure 6.6. This validation case includes natural convection, which has been investigated experimentally as well as numerically using the Finite Volume Method (FVM) and LBM before (Gau and Viskanta 1986; Kumar et al. 2006; Wittig and Nikrityuk 2011; Zhu et al. 2017; Abishek et al. 2018). Geometry and operation conditions follow the experiments of Gau and Viskanta (1986) using an enclosure of size $88.9 \times 63.5 \times 38.1\,\mathrm{mm}^3$, in which a hot wall ($x = 0\,\mathrm{mm}$) is maintained at $T_h = 311\,\mathrm{K}$ and the opposing wall ($x = 88.9\,\mathrm{mm}$) is maintained at $T_c = 301.3\,\mathrm{K}$, while the other walls are adiabatic. Initially, the enclosure is filled with solid gallium at temperature T_c. The melting temperature of gallium is given with $T_m = 302.8\,\mathrm{K}$. In both, 2D and 3D simulations, the enclosure is resolved with $N = 320$ cells over the distance from hot to cold wall and with $\tau_g = 1$.

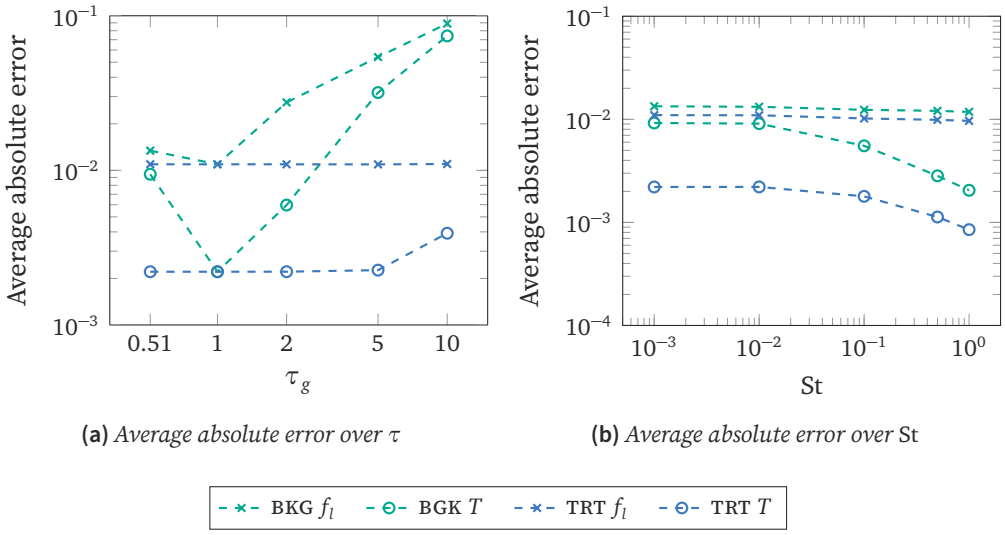

(a) *Average absolute error over* τ

(b) *Average absolute error over* St

Figure 6.5: *Average absolute error over relaxation time* τ *(a) and over the Stefan number* St *(b).*

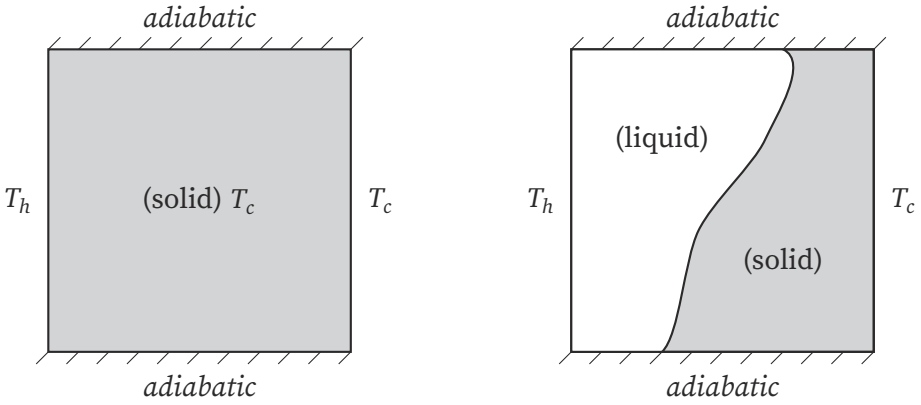

(a) $t = 0$

(b) $t = t_\tau > 0$

Figure 6.6: *Schematic representation of the simulation setup of the melting of pure gallium including boundary conditions.*

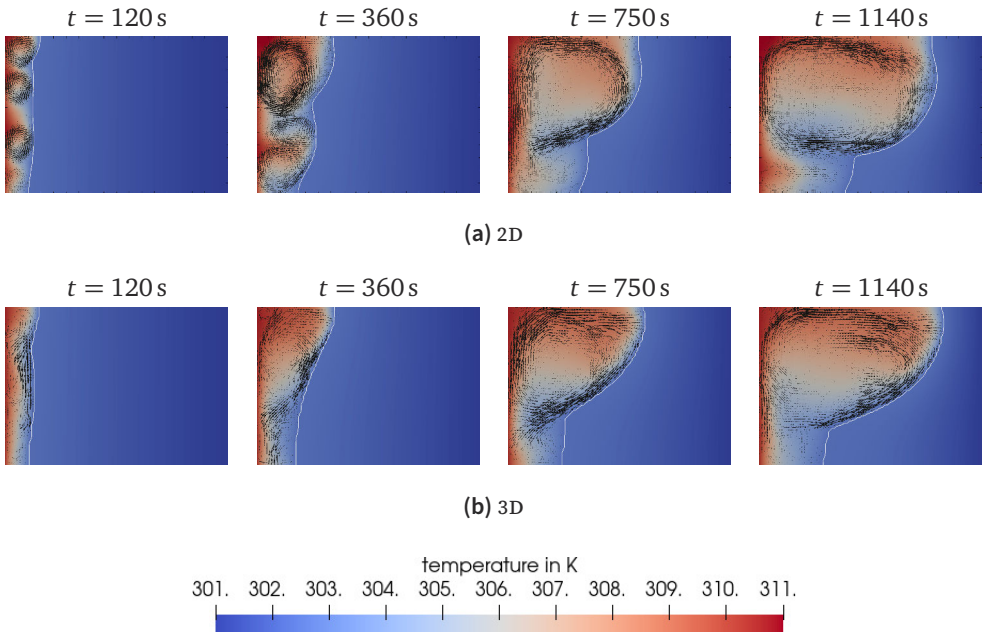

Figure 6.7: 2D *(a) and* 3D *(b) slice for the case of melting gallium at time steps* $t = 120\,\text{s}$, $360\,\text{s}$, $750\,\text{s}$ *and* $1140\,\text{s}$. *Velocity vectors in black, melting front in white, temperature in blue (cold) to red (hot).*

Figure 6.7 shows slices at the middle of the domain of the simulation results for 2D and 3D at different time steps t =120 s, 360 s, 750 s and 1140 s. The circulation flow of molten gallium induced by buoyancy forces is depicted through vector representation of the velocity field in the x-y-plane, while the temperature distribution is depicted through color gradients. It can be seen from the figures that the predicted transient flow structures and temperature distributions are in good agreement with the results of Zhu et al. (2017), which also found initially three, then two vortex ensembles and finally one large convection vortex with increasing duration, leading to the characteristic melt front sequence. The difference between 2D and 3D melting is clearly visible, which again confirms the findings from Zhu et al. (2017).

Figure 6.8 shows the comparison of the position of the melt front for the mentioned time steps between the present LBM, experimental data from Gau and Viskanta (1986) and simulations from Kumar et al. (2006), Wittig and Nikrityuk (2011) and Abishek et al. (2018). As seen from the plot in Figure 6.8 close agreement with the literature is observed; the present simulations are espe-

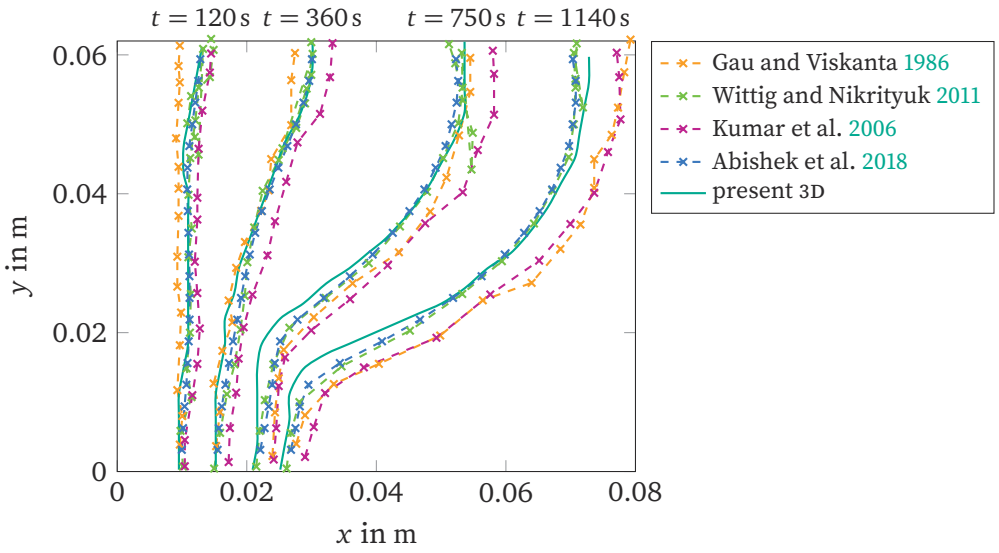

Figure 6.8: *Melting front over x and y-position for the case of melting gallium at time steps $t = 120\,\mathrm{s}$, $360\,\mathrm{s}$, $750\,\mathrm{s}$ and $1140\,\mathrm{s}$. Comparison between Gau and Viskanta (1986), Wittig and Nikrityuk (2011), Kumar et al. (2006) and Abishek et al. (2018) with the present* 3D TRT *model.*

cially close to the simulations presented in Wittig and Nikrityuk (2011) and Abishek et al. (2018), which suggests that deviations from experimental data originate from the adaption of the experimental setup into the simulations and less likely to be due to the current LBM model.

6.4 Application

6.4.1 Paraffin/Metal foam composite PCM

Abishek et al. (2017) recently provided a computational methodology for the generation of realistic foam models with customizable micro-scale properties. This validated technique is used to produce the metal foam geometries for this study. Two of the foam geometries investigated in Abishek et al. (2018) are used in this study to compare the present models applicability to pore-scale melting simulations. Referenced as GEO48 and GEO72, the porosity of the foam is $\epsilon = 94\,\%$ in both cases and their respective strut diameters are $d_{\mathrm{GEO48}} = 0.48\,\mathrm{mm}$ and $d_{\mathrm{GEO72}} = 0.72\,\mathrm{mm}$. These cubic foam structures with di-

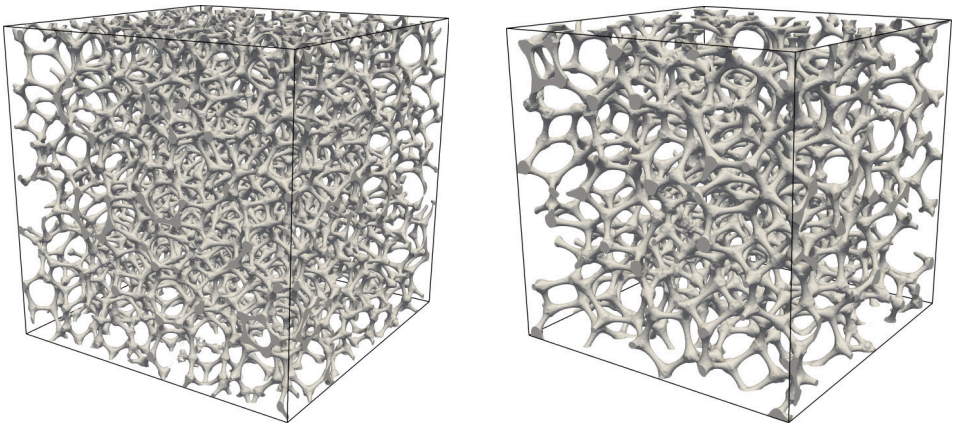

(a) GEO48 **(b)** GEO72

Figure 6.9: *Generated foam structures with a porosity of* $\epsilon = 94\,\%$ *and strut diameters* $d_{\mathrm{GEO48}} = 0.48\,\mathrm{mm}$ *(a) and* $d_{\mathrm{GEO72}} = 0.72\,\mathrm{mm}$ *(b).*

mensions of $l_x = l_y = l_z = 40\,\mathrm{mm}$ are shown in Figure 6.9. For a detailed description of the geometry generation and its validation, the reader is referenced to Abishek et al. (2017) and Abishek et al. (2018). As in reference Abishek et al. (2018), both, the internal (foam) and external (paraffin) meshes were retained for the conjugate thermal analysis, however, for the LBM it is not necessary to create matching meshes of the two regions. Instead, the simulation domain is uniformly voxelized and the respective material properties assigned to each cell, either commercial n-eicosane paraffin ($C_{20}H_{42}$) or 6061 aluminum alloy foam. The thermophysical material properties used here are given in Table 6.1. For the melting simulation the entire domain is set to an initial temperature of 309.15 K (slightly below the melting temperature of 309.55 K), while the upper wall is considered to be constantly heated at a temperature of 330.16 K and the lower wall is assumed adiabatic. The Stefan number for the given problem is $\mathrm{St} = 0.188$. Because of the highest temperature at the top of the considered domain, natural convection of the molten paraffin is negligible allowing an isolated investigation of the influence of the micro structure. In order for the simulation domain to represent a larger composite PCM, the vertical facets are assumed symmetric.

The mesh generation and resulting mesh quality is assessed in Section 6.4.2, followed by the results of the transient melting simulations in Section 6.4.3.

Table 6.1: *Thermophysical material properties.*

property	units	aluminum	solid paraffin	liquid paraffin
ρ	kg/m^3	2700.0	815.0	739.2
c_p	J/(kg K)	872.0	1926.0	$1323 + 3.011\ T$
λ	W/(m K)	167.0	0.423	0.146
L	J/kg	–	24300	–
T_m	K	–	309.55	–

6.4.2 Mesh generation and quality assurance

As a first step for the mesh generation, the imported STL file is distributed into a given number of blocks and subsequently discretisized into a voxel mesh by applying a ray tracing algorithm (Fietz et al. 2012). This supplies a boolean mask, which evaluates to true for the voxels inside of the body described by the STL surface and false if the respective voxel lies outside – also referred to as solid voxelization (Schwarz and Seidel 2010). More precisely, a voxel is considered to be *inside* if its center is within the volume enclosed by the STL surface. Similar boolean masks distinguish between bulk and boundary cells; these masks are used to assign different material properties, collision schemes, boundary models and other properties to the respective cells. Due to its locality, the process can be easily distributed over hundreds of cores (taking load balancing into account), so that even complex geometries such as metal foams can be generated and pre-processed on modern HPC hardware in less than six minutes (Fietz et al. 2012). For example the foam geometry GEO72 – described by 2.52 million triangles – is discretized into a mesh of 134.22 million cells and distributed for parallel computation in 5 min 37 s on 72 Intel Xeon cores (E5-2690 v3, Haswell) on the Magnus Cray XC40 supercomputer.

The mesh quality is investigated for both the foam geometries considered. The dependence on the resolution N, which is determined by the amount of cells per 40 mm, is examined. The quality is assessed based on the accuracy of both, the porosity and the foam's surface area. For resolutions between $N = 32$ and 512 porosities of 94.04 % and 94.59 % have been observed, while the reference geometry's porosities for GEO48 and GEO72 are 94.22 % and 94.16 % resulting in the relative errors shown in Figure 6.10. Herein, the volume representation of the simulation domain is shown to converge towards its respective reference value.

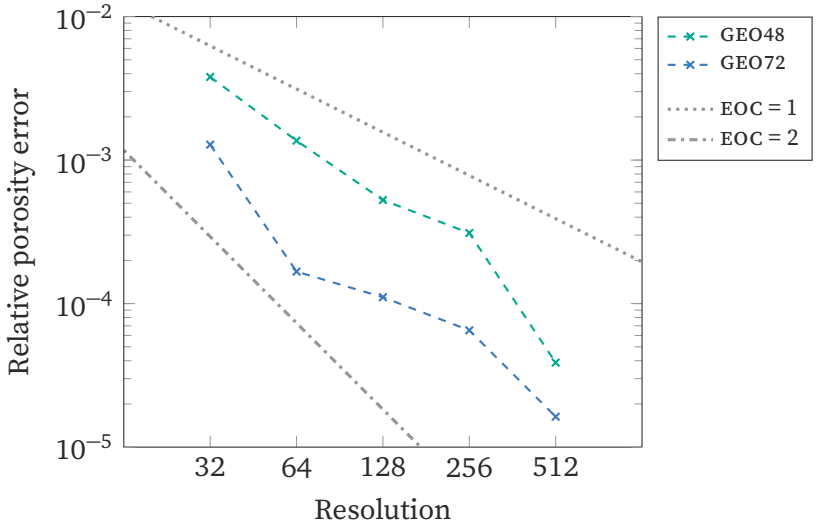

Figure 6.10: *Grid convergence study: Relative porosity error over resolution for the two foam geometries.*

However, for the error with regard to the foam's surface area this convergence is not the case as shown in Figure 6.11. The calculated surface area from the voxel meshes and the relative error are plotted against the reference values of $A_{\text{GEO48}} = 0.019\,768\,1\,\text{m}^2$ and $A_{\text{GEO72}} = 0.013\,402\,7\,\text{m}^2$ for several resolutions from $N = 64$ to 450. It is evident that the surface area is underpredicted for small resolutions, whereas it is over predicted for higher resolutions. Thus, there is an optimum resolution, at which the relative error regarding the surface area is minimal, which is found with $N^{opt}_{\text{GEO48}} = 279$ and $N^{opt}_{\text{GEO72}} = 183$, respectively.

To explain these deviations from the reference surface area, a schematic drawing is given in Figure 6.12 showing the two cases of the discretization of a circle in 2D – with minimal resolution of the inscribed cell in Subfigure (a) and with almost infinite resolution in Subfigure (b). In the case of one inscribed cell it is trivial to calculate the circumferences of the square cell and the reference circle, which results in an underrepresentation of the surface with a relative error of −9.97 %. At almost infinite resolution, the circle can be approximated as a diagonal straight line. Comparing the outward circumference of the square cells with the length of the reference line, an over prediction of the surface with a relative error of 41.4 % can be approximated as the upper limit. Thus,

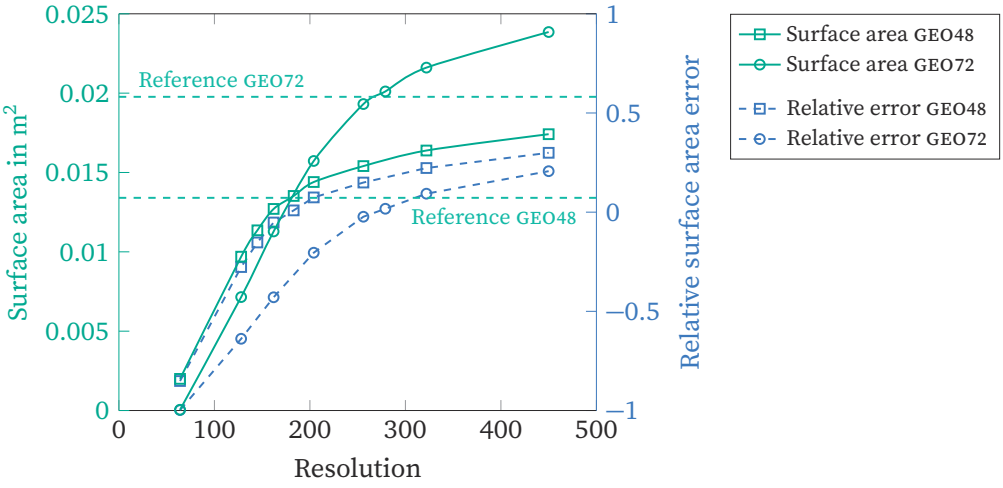

Figure 6.11: *Surface area (left y-axis) and relative error of surface area with respect to reference value (right y-axis) over the resolution.*

the deviations presented in Figure 6.11 for the 3-dimensional voxelization of the foam geometries appear plausible. Concerning spatially resolved conjugated heat transfer methods utilizing LBM, this seems to be an insufficiently addressed problem, which should be explored in more detail in future studies. Since the transient melting process within the composite PCMs is likely to be very sensitive to the representation of the foam surface area, these optimal resolutions stated above are used for the following simulations.

6.4.3 Transient melting results

The melting fronts for the two foam geometries and four time steps corresponding to Fourier numbers $\mathrm{Fo} = \frac{\alpha_{foam}\, t}{L_z^2} = 12$, 25, 38 and 51 are shown in Figure 6.13. Above the melting front shown in blue the paraffin wax is liquid and solid below. It can be seen from Figure 6.13 that the micro structural features of the foam are greatly influencing the melting procedure. The heat from the top wall is mainly transported through the metal structure due to its much higher conductivity, resulting in faster melting of the wax on the foams surface. Thus, the effective surface available for the heat transfer into the wax is increased giving a higher effective thermal conductivity for the composite PCM over the wax-only PCM. A deeper penetration of the melting front along the foam structures is observed in Figure 6.13 for the foam with strut diame-

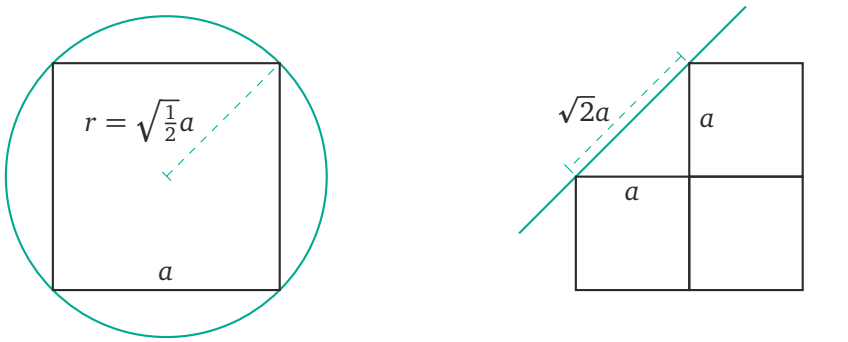

$U_{ref} = 2\pi\sqrt{\frac{1}{2}}a \quad U_{mesh} = 4a$

$\epsilon_{rel} = \frac{U_{mesh} - U_{ref}}{U_{ref}} \approx -9.97\,\%$

(a) $N = 1$

$U_{ref} = \sqrt{2}a \quad U_{mesh} = 2a$

$\epsilon_{rel} = \frac{U_{mesh} - U_{ref}}{U_{ref}} \approx 41.4\,\%$

(b) $N \to \infty$

Figure 6.12: *Schematic drawing of the simplified meshing of a circle (shown in green) in* 2D *with the cells depicted as squares (shown in black). The cases of minimal resolution $N = 1$ (a) and maximum resolution $N \to \infty$ (b) are shown, where for the latter the curvature of the circle is assumed to be flat when infinitesimally close.*

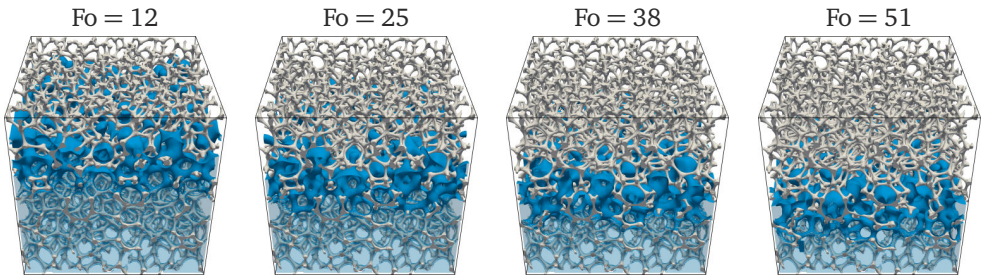

(a) GEO48

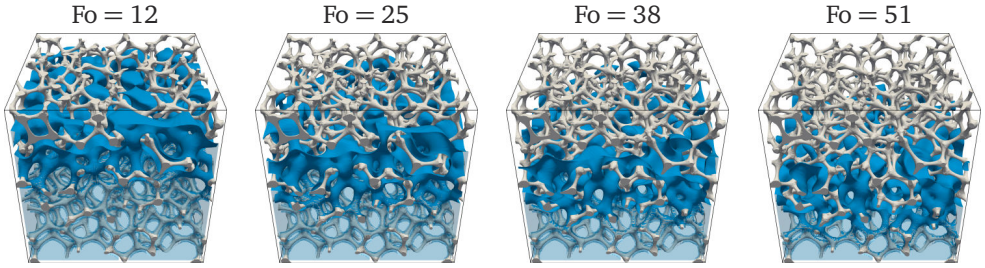

(b) GEO72

Figure 6.13: *Melting front (blue) at time steps corresponding to* Fo = 12, 25, 38 *and* 51 *for* GEO48 *(a) and* GEO72 *(b). The liquid paraffin is translucent, the solid paraffin is colored in blue and the metal foam is shown in light gray.*

ter of $d = 0.72\,\text{mm}$ compared to the total height of the melting front within the foam with thinner strut diameter ($d = 0.48\,\text{mm}$). This coincidences well with the findings of Abishek et al. (2018), compare Figure 3 therein.

To further investigate the melting speed, the total liquid fraction (by means of the volume) is plotted over the Fourier number in Figure 6.14. In addition to the present simulation results, the liquid fraction obtained by Abishek et al. (2018) are shown. In the beginning, a rapid increase in the liquid fraction is observed, while the steepness decreases with time and the liquid fraction converges against unity. By investigating the relative melting interface area A_i/A_f, where A_i identifying the melting interface area and A_f is the specific surface area of the foam, Abishek et al. observed four distinct melt stages: (1) the initiation of melting associated with a steep rise in the relative melting interface area, (2) the substantial melting associated with a small rise of A_i/A_f, (3) in which the relative melting interface area and the melt fraction increase simultaneously, and (4) the decrease of A_i/A_f until all the paraffin has melted. According to Abishek et al. (2018), each of these four stages is influenced by

the micro structural properties of the foam. Other studies also noted similar phenomena (X. Chen et al. 2019; Dinesh and Bhattacharya 2019; Dinesh and Bhattacharya 2020), but have not discussed the observation in detail. While the present simulations show the first, second and fourth stage with close agreement to the Abishek's simulations in Figure 6.14, the third stage is not visible. In the Abishek's simulations, an acceleration of the melting is seen starting at $\mathrm{Fo} \approx 10$ for GEO72 and $\mathrm{Fo} \approx 20$ for GEO48, whereas this phenomenon is not seen in the LBM simulations.

Possible reasons for this underprediction could be insufficient resolution to evaluate the conduction inside the metal foam. The present meshing and numerical model do not allow to vary the resolution independently from the resulting surface, so that this relationship cannot be investigated in detail here. An extended scheme is required for this, an extension following the idea of curved boundary formulations (Bouzidi et al. 2001; Guo et al. 2002b; H. Huang et al. 2006; Li et al. 2013; Li et al. 2014b) is conceivable, but in this case a transient implicit boundary position must be used. Similar problems have been addressed for free surface simulations (Thürey and Rüde 2004; Körner et al. 2005); it remains to be explored whether these ideas can be applied here. Further plausible influences could be due to the fact that the current approach does not consider expansion of liquid paraffin at higher temperatures and the resulting – albeit tiny – flow. Experimental validation of whether the third phase of melting in the metal foam is actually given by the acceleration described by Abishek et al. (2018) remains a task for future research.

However, as the liquid fractions for higher Fo run parallel to each other, the total deviation between the two simulation methods is comparatively small with the relative error at $\mathrm{Fo} = 85$ of 13.08 % and 9.97 % for GEO48 and GEO72, respectively. The total melting times are simulated to 59 min for GEO48 and 72 min for GEO72, whereas without the metal foam it would take 681 min according to (6.26).

6.5 Conclusion

In this paper, an LBM for the simulation of melting and conjugate heat transfer is proposed, validated and applied to three-dimensional melting in composite PCM-metal foam latent heat storages. The model and its implementation in the open source framework OpenLB is successfully validated against the analytical transient solution of the Stefan problem proving superlinear grid convergence.

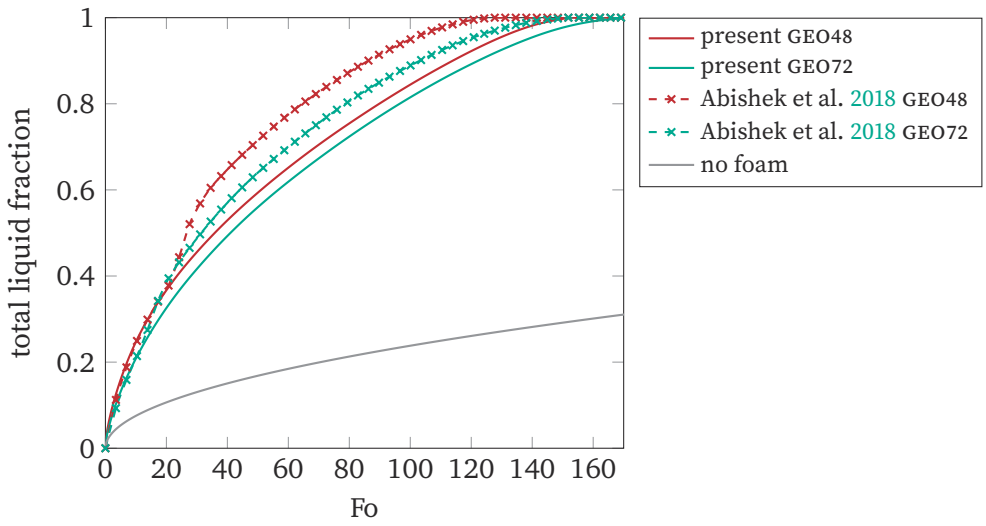

Figure 6.14: *Liquid fraction over Fourier number for the two foam geometries. Comparison between the present* TRT *model and results from Abishek et al. (2018).*

Low interfacial diffusion for a large range of relaxation times and Stefan numbers is found for the TRT scheme with a constant "magic parameter" $\Lambda = \frac{1}{4}$. Close agreement to measurements and simulation results obtained by other methods is shown for the validation case of melting gallium including natural convection in 2D and 3D.

Subsequently, the method is applied to the melting of paraffin in two complex metal foam geometries. A voxel-based parallel meshing is presented, allowing fast and automated preprocessing in a matter of minutes even for a geometry described by 2.52 million triangles and a mesh with about 130 million cells. The present simulation setup is able to recapture the multi-domain heat transfer in 3D, where the thermal conductivity of the foam is more than 1000 times larger than that of the paraffin. The predicted progression of the melting front and the influence of the different foam's specific surface areas are in close agreement to earlier simulations.

So it can be concluded, that the present LBM is a promising candidate for these kind of simulations in the future. However, the shown problem of the correct representation of the foam's specific surface area in the voxel mesh currently limits the merit of a refinement of the mesh and needs further investigation. The actual foam surface could be considered similar to a curved

boundary scheme in the LBM (Bouzidi et al. 2001; Guo et al. 2002b). The present LBM simulations do not show an acceleration of melting in the second stage which was found in the simulations of Abishek et al. (2018) showing four stages of melting. The parameters and conditions influencing this stage, and why it is not seen in the present simulations is out of scope here, and thus left for future study.

7
Conclusion and Outlook

This thesis presents a 3D double distribution function TLBM based on the BGK collision operator and supplemented by the Smagorinsky turbulence model in Chapter 2. Natural convection is taken into account by buoyancy forces calculated with the Boussinesq approximation. The method is implemented in the open source framework OpenLB. After extensive validation of the described model, the applicability of the present method for the determination of flow properties and coupled heat transfer is investigated.

In Chapter 3 second order grid convergence is demonstrated for the present model against the analytical *porous plate problem*. While stable even for coarse discretization with high Re and Ra numbers, very good agreement is also shown for the *natural convection in a square cavity*, a well-known benchmark case, from laminar to turbulent regime with $10^3 \leq \mathrm{Ra} \leq 10^{10}$ and at resolutions of $y^+ \approx 2$.

Subsequently, simulations of an empty cooling body for a refrigerated truck are performed. The flow field and heat transfer within the given refrigerated truck is compared with measurement results, in particular, experimental data for a refrigerated vehicle at $\mathrm{Re} \approx 53\,000$ at four characteristic velocity and 13 temperature positions in the truck. With absolute errors below 0.4 m/s for the velocities and below 1 K for the temperatures very good agreement is shown. Heat transfer through the walls is resolved in the simulations by conjugate heat transfer. This not only allows to predict global heat fluxes close to Nusselt correlations for the given setup, but also the heat flux to be spatially

resolved in the simulation, in contrast to the usual Nusselt correlations, where only global heat flux values are calculated. This is one major advantage of the present method using conjugate heat transfer.

Flow and heat transfer in an annular gap with inner rotating cylinder is investigated as presented in Chapter 4. The particular challenge in the simulation of this *Taylor-Couette flow* is the formation of Taylor vortices, which, due to their rotation perpendicular to the main flow direction, significantly increase the corresponding heat transfer. For this purpose, detailed simulations are performed over a wide rotational speed range from almost creeping flows to the occurrence of Taylor vortices. Note that the turbulent flow domain of a *Taylor-Couette flow* (see e.g. Fardin et al. 2014; Grossmann et al. 2016) is not considered in the present work.

The applied model shows precise reproduction of the *Taylor-Couette flow* field and the resolution of unsteady, wave-shaped Taylor vortices. Good agreement with the previous results for the flow structure and the improvement of heat transfer by Taylor vortices is found. In particular, the present method is compared against measurements by Becker (1957), correlation from Becker and Kaye (1962) and simulations with Ansys CFX with the SST turbulence model. This close agreement with all comparison values leads to a mean total error for the global Nusselt number below 6.9 % for the SST model and 8.2 % for the present LBM-LES approach over the entire rotational speed range investigated. An average simulation with the rotational speed of $\omega_{in} = 151/\text{min}$ ran in the order of one to two core hours for both solvers. Considering that LBM-LES provides time-dependent results at comparable run times indicates its speed advantage, while a detailed performance comparison is difficult due to the different setups.

Special attention is paid to the prediction of the critical Taylor number. While direct numerical simulations (DNS) with LBM predict the critical Taylor number from the experiments almost identically, the LBM-LES slightly overestimates it and the SST model further overestimates the occurrence of Taylor vortices, which can be attributed to the overly dissipative nature of the turbulence models for the transition to turbulent flow conditions.

Subsequent to the method's successful validation, innovative concepts for improved, more sustainable refrigerated vehicles are numerically investigated as presented in Chapter 5. In order to reduce fuel consumption and related emissions, the following two approaches are considered promising:

(a) the inclusion of vacuum insulation panels (VIP) in the walls of the refrig-

erated body

(b) the introduction of a latent heat storage (LHS) to exchange fuel-driven air conditioning (AC)

Both concepts are simulated with the double distribution TLBM, which includes spatial and unsteady conjugate heat transfer. This allows the resolution of turbulent air flow induced by the AC and natural convection, the heat flux inside the insulating walls and the deep frozen cargo in the simulations. New insights into the influence of the concepts on heat transfer in different refrigerated bodies are hence provided.

As a result, the simulations show strongly reduced and homogenized incoming heat flow for the combined PUR and VIP insulation material compared to a pure PUR insulation. The insulation of the cooled structure using VIPs therefore halves the required cooling energy. This also makes it possible to replace the AC system with an LHS mounted near the top of the heat sink and an additional ventilation system with markedly lower overall capacity. Taking into account the temperature homogeneity of frozen products, a slight flow around the chilled goods is considered necessary. The maximum allowable downtime of the AC system is determined in the simulations to be approximately 3.3 min in the case of PUR insulation, 8 min in the case of improved VIP insulation and 11 min in the case of an additional LHS.

The virtual truck prototypes simulated and presented here show superior insulation and refrigeration performance characteristics compared to the reference refrigerated truck. Nevertheless, they are virtual prototypes, so the practical implementation should be pursued with a physical prototype to verify the predictions of the simulation. This is already being done within the framework of the cooperation project *ZF4005102CL5* funded by the *Central Innovation Program for* SMEs, so that corresponding results will be published elsewhere shortly.

In Chapter 6 an LBM for the simulation of melting and conjugate heat transfer based on the transport of total enthalpy is presented. The model yields precise results for validation against the analytical solution of the time-dependent Stefan problem. For the TRT scheme with a constant "magic parameter" $\Lambda = \frac{1}{4}$, low interfacial diffusion is shown for a wide range of relaxation times and Stefan numbers. Furthermore, close qualitative agreement with measurements from Gau and Viskanta (1986) and simulation results from Kumar et al. (2006), Wittig and Nikrityuk (2011), and Abishek et al. (2018) for gallium melting including natural convection in 2D and 3D is demonstrated.

This successful validation allows the application on three-dimensional simulation of melting processes in composite phase change materials (PCM) and metal foam latent heat storages. In this thesis, the model is applied to the melting of paraffin in two complex metal foam geometries. Voxel-based parallel meshing is presented, which allows fast and automated preprocessing of the complex geometry in a few minutes. The simulation successfully captures multi-domain heat transfer in 3D, with the thermal conductivity of the foam being more than 1000 times greater than that of the paraffin. The shape of the melt front and the influence of the specific surface areas of the different metal foams are in close agreement with previous simulations. In their simulations, Abishek et al. (2018) found four stages for the melting process of paraffin, whereas the simulations presented here do not show the acceleration of the phase change which is associated with the second stage. The extent to which this distinction is due to insufficient resolution or inaccurate modeling by the present LBM scheme cannot be conclusively assessed here and requires further investigation.

Future Work

In view of the above conclusions, it is shown in particular that

- TLBM is an robust, accurate and efficient simulation tool for unsteady fluid flow problems,
- the combination of TLBM and LES enables industrial and engineering applications on a large scale,
- TLBM is expandable, e.g. by conjugate heat transfer or melting.

Nevertheless, there is potential in various areas to extend the method and its application or to propose improvements through a better understanding of the specific mathematical modeling.

For example, Dellar (2014) has succeeded in reconstructing correction terms for the fourth moment of the distribution function, which actually cannot be fully represented, using lower moments resulting in improved Galilean invariance. Similar approaches were presented by Geier et al. (2017) and Bauer and Rüde (2018). Dellar's corrections are based on consistent representation of the velocity discrete distribution function as a Hermite series, as shown in Section 2.3. This expansion allows an error analysis of the series truncation before the temporal and spatial discretization is performed, so that these

sources of error can be excluded in the analysis, see this approach also in Silva and Semiao (2014), Coreixas et al. (2019), and De Rosis and K. H. Luo (2019). Based on the regularization of the distribution functions following Latt and Chopard (2006), Malaspinas (2015) was able to propose an extended recursive regularization that significantly increases the stability of the algorithm for Mach numbers up to about 0.5. The consistent representation as a series on one hand, and deeper understanding of the numerical processes on the other hand, together offer great potential and should definitely be pursued further.

Turbulence modeling in the LBM is controversially discussed. A number of works are based on the phenomenological models from the continuum regime, more precisely on models that are also used for closure in the NSE. Examples are the Smagorinsky model (see Section 2.2), the k-ϵ, Vreman or WALE models (Succi et al. 1995; Weickert et al. 2010; M. Liu et al. 2012a). In the LBM, the corresponding relaxation time for the collision is usually modified via the eddy viscosity assumption. In principle, however, the LBM is based on the kinetic theory of gases, i.e. their statistically described convection and collision. This motivates a new class of turbulence modeling for the LBM, which uses the kinetic background of the LBM to introduce closure terms of the filtered or averaged LBE. A number of approaches following this idea are presented by H. Chen et al. (2003), Ansumali et al. (2004), Karlin et al. (2014), and Geier et al. (2015), where the latter two rather represent a stabilization for strongly underresolved simulations than a full-fledged turbulence model in the sense of LES – at least their respective dissipation and filter properties have not been satisfactorily investigated in this context so far. Unfortunately, recent literature on turbulence in kinetic theory is comparatively rare, see Lundgren (1967), M. B. Lewis (1975), and Tsugé and Sagara (1976) for some earlier theoretical works on the topic. That given, it is a particular challenge to find suitable model approaches, while such a closure would represent true added value compared to other NSE solvers.

However, well-established and validated turbulence models from continuum modeling should not be disregarded. In particular, wall-adaptive models have not yet been comprehensively tested in the LBM. This may partly be due to the fact that many of these wall-adaptive models require additional information, such as the anti symmetric part of the stress tensor in the case of WALE, or explicit filtering in the case of scale separating models or the approximate deconvolution method (Bardina et al. 1980; Stolz and Adams 1999). These additional variables can no longer be determined exclusively from the moments of the distribution functions, and are therefore usually approximated using fi-

nite differences. The implementation of such enhancements breaks LBM's locality, which is the main reason for its parallel performance. Nevertheless, wall-adaptive models have shown higher precision than the simple Smagorinsky model and should therefore be further investigated. Their combination with LBM will increase the comparability and competitiveness with other numerical methods.

It will not be possible in the near future to adequately resolve the sometimes very thin turbulent boundary layer in the simulation for industrial applications on full apparatus scale or even on plant scale. A common approach is to provide dedicated models for the boundary layer, which replace the much higher resolution otherwise required near the wall – this is referred to as near wall modeled LES as opposed to near wall resolved LES (Fröhlich 2006). While first approaches for near wall models have been adopted in the LBM (Malaspinas and Sagaut 2014; Haussmann et al. 2019; Pasquali et al. 2020), the difficulty is, that there are many possible boundary treatments for the LBM – "dry" or "wet" boundary cells, complete or partial reconstruction, interpolation, extrapolation, ... (Krüger et al. 2017). Regarding LBM, near wall modeled LES is only in the early stages of exploring the options and understanding their influence on simulation results. With regard to the abundance of proposed near wall models in the FVM context (see e.g. Nayamatullah and X. Liu 2013, for an overview), there is still much to investigate for the LBM; not only which near wall models can be implemented at all, but also which LB boundary schemes are suitable. Another interesting approach would be to perform near wall modeling based on kinetic theory, similar to the approaches for slip boundary conditions for rarefied gases (Lim et al. 2002; Tang et al. 2005, among others).

While the above-mentioned topics relate to the solution of flow problems by means of isothermal LBM, there is still potential for improvement, especially for thermal LBM. Neither the closure of the filtered convection-diffusion equation, nor the near wall modeling for thermal flows have yet reached a comparable maturity in LBM to corresponding model approaches for FVM. In addition, the LBM for the convection-diffusion equation also leads to constellations for which no satisfactory approaches have been found so far – for instance, the explicit setting of heat flows, a common boundary condition in thermal process engineering. Previous approaches for such boundary conditions often use finite differences to determine the temperature on the boundary cell, which in turn is entered into the boundary scheme as a set temperature (D'Orazio and Succi 2003; C.-H. Liu et al. 2010). However, it is known that the heat flux in the LBM can be calculated from the first moment of the distribution's non-

equilibrium parts, analogous to the shear rate (Chai and T. S. Zhao 2014). Although setting the boundary temperature based on finite differences results in proper approximation of the equilibrium parts of the distribution function, the non-equilibrium components are not calculated consistently. A general boundary condition scheme to explicitly set non-equilibrium components in order to define the desired heat flux is not known currently, but offers the potential to implement boundary conditions for the heat flux and wall shear stresses consistently. See Allen and Reis (2016) and Krastins et al. (2020) for an initial attempt in 2D and 3D, respectively.

In the present study of melting in resolved metal foams, it was found that the volume of the discrete bodies in the finer lattice converges to the reference value, while the discrete surface area continues to increase, compare Section 6.4.2. Since this effect is insignificant in most flow problems, little attention has been paid so far. For simulations of conjugate heat transfer, however, the representation of the interface is essential. For this purpose, schemes known from the immersed boundary methods could be investigated in the future, see Krüger et al. (2017) for an overview. These methods employ distance or volumetric approximations to represent the real surface of the bodies in the boundary treatment of the LBM, whereby curved geometries can be simulated with higher accuracy and convergence order, see e.g. in the works by Noble and Torczynski (1998), Bouzidi et al. (2001), Guo et al. (2002b), H. Huang et al. (2006), Li et al. (2013), and Li et al. (2014b). To what extent these methods can be applied to the treatment of conjugated heat transfer is still an open question, since immersed boundary methods are to be understood as boundary conditions that represent a boundary between simulated medium and non-medium; for conjugated heat transfer, by contrast, the transition between two media must be described correctly.

Acknowledgment

This work was supported by the German *Central Innovation Programme for* SMEs by funding the projects "Entwicklung eines innovativen Kühlsystems für Nutzfahrzeuge" (ZF4005102CL5) and "Entwicklung eines passiven Kühlaufbaus für Elektrofahrzeuge" (ZF4005111JA8) and the company *Kress Fahrzeugbau GmbH* by making available the validation measurements of the refrigerated truck.

This work was performed on the computational resources

- ForHLR II at Karlsruhe Institute of Technology, Germany funded by the Ministry of Science, Research and the Arts Baden-Württemberg and "Deutsche Forschungsgemeinschaft" (DFG) and
- Magnus at Pawsey Supercomputing Centre, Perth, Western Australia with funding from the Australian Government and the Government of Western Australia.

The author's stay abroad at the Curtin University in Perth, Australia was kindly supported by the Karlsruhe House of Young Scientists (KHYS), Karlsruhe Institute of Technology, Germany.

List of Puplications

Peer-reviewed publications

Gaedtke, M., Wachter, S., Rädle, M., Nirschl, H., and Krause, M. J. (2018c). "Application of a lattice Boltzmann method combined with a Smagorinsky turbulence model to spatially resolved heat flux inside a refrigerated vehicle." In: *Computers & Mathematics with Applications* 76.10, pp. 2315–2329. DOI: 10.1016/j.camwa.2018.08.018.

Gaedtke, M., Hoffmann, T., Reinhardt, V., Thäter, G., Nirschl, H., and Krause, M. J. (2019a). "Flow and heat transfer simulation with a thermal large eddy lattice Boltzmann method in an annular gap with an inner rotating cylinder." In: *International Journal of Modern Physics C* 30.2-3. DOI: 10.1142/S012918311950013X.

Onorato, C., Gaedtke, M., Kespe, M., Nirschl, H., and Schäfer, A. I. (2019). "Renewable energy powered membrane technology: Computational fluid dynamics evaluation of system performance with variable module size and fluctuating energy." In: *Separation and Purification Technology* 220.February, pp. 206–216. DOI: 10.1016/j.seppur.2019.02.041.

Ross-Jones, J., Gaedtke, M., Sonnick, S., Rädle, M., Nirschl, H., and Krause, M. J. (2019). "Conjugate heat transfer through nano scale porous media to optimize vacuum insulation panels with lattice Boltzmann methods." In: *Computers & Mathematics with Applications* 77.1, pp. 209–221. DOI: 10.1016/j.camwa.2018.09.023.

Gaedtke, M., Abishek, S., Mead-Hunter, R., King, A. J. C., Mullins, B. J., Nirschl, H., and Krause, M. J. (2020a). "Total Enthalpy-Based Lattice Boltzmann Simulations of Melting in Paraffin/Metal Foam Composite Phase Change

Materials." In: *International Journal of Heat and Mass Transfer* 155, p. 119870. DOI: 10.1016/j.ijheatmasstransfer.2020.119870.

Gaedtke, M., Wachter, S., Kunkel, S., Sonnick, S., Rädle, M., Nirschl, H., and Krause, M. J. (2020c). "Numerical study on the application of vacuum insulation panels and a latent heat storage for refrigerated vehicles with a large Eddy lattice Boltzmann method." In: *Heat and Mass Transfer* 56.4, pp. 1189–1201. DOI: 10.1007/s00231-019-02753-4.

Krause, M. J., Kummerländer, A., Avis, S. J., Kusumaatmaja, H., Dapelo, D., Klemens, F., Gaedtke, M., Hafen, N., Mink, A., Trunk, R., Marquardt, J. E., Maier, M.-L., Haussmann, M., and Simonis, S. (2020). "OpenLB – Open source lattice Boltzmann code." In: *Computers & Mathematics with Applications*. DOI: 10.1016/j.camwa.2020.04.033.

Sonnick, S., Erlbeck, L., Gaedtke, M., Wunder, F., Mayer, C., Krause, M. J., Nirschl, H., and Rädle, M. (2020). "Passive room conditioning using phase change materials-Demonstration of a long-term real size experiment." In: *International Journal of Energy Research* March, pp. 1–10. DOI: 10.1002/er.5406.

Conference Talks

Gaedtke, M., Ross-Jones, J., Nirschl, H., Krause, M. J., and Rädle, M. (2017a). "Lattice Boltzmann Simulationen zur Isolationsoptimierung eines innovativen Kühlsystems für Nutzfahrzeuge." In: *Jahrestreffen der ProcessNet Fachgruppe Wärme- und Stoffübertragung*. Bruchsal, Germany.

Gaedtke, M., Ross-Jones, J., Nirschl, H., Krause, M. J., and Rädle, M. (2017b). "Validated Fluid Flow Simulations towards Insulation Optimization for a Refrigerated Vehicle using Lattice Boltzmann Method." In: *14th International Conference for Mesoscopic Methods in Engineering and Science*. Nantes, France.

Gaedtke, M., Hoffmann, T., Reinhardt, V., Thäter, G., and Krause, M. J. (2018a). "Flow and Heat Transfer Simulation with Lattice Boltzmann and Finite Volume Method in an Annular Gap with an Inner Rotating Cylinder." In: *27th International Conference on Discrete Simulation of Fluid Dynamics (DSFD)*. Worcester, USA.

Gaedtke, M., Hoffmann, T., Reinhardt, V., Thäter, G., and Krause, M. J. (2018b). "Strömungssimulation und Wärmeübertragung mit Lattice Boltzmann und Finite Volumen Methode im Ringspalt mit einem inneren rotieren-

den Zylinder." In: *Jahrestreffen der ProcessNet Fachgruppe Computational Fluid Dynamics*. Bremen, Germany.

Gaedtke, M., Nirschl, H., and Krause, M. J. (2019b). "Virtual Reality Visualisierung von Daten aus numerischen Strömungssimulationen." In: *Networking Campus at POWTECH*. Nürnberg, Germany.

Gaedtke, M., Rau, D., Nirschl, H., and Krause, M. J. (2019c). "Development and Investigation of Thermal Subgrid-Scale Models for a Large Eddy Lattice Boltzmann Method." In: *17th European Turbulence Conference*. Turino, Italy.

Gaedtke, M., Abishek, S., Mead-Hunter, R., King, A. J., Mullins, B. J., Nirschl, H., and Krause, M. J. (2020b). "Total enthalpy-based lattice Boltzmann simulations of melting in paraffin/metal foam composite phase change materials." In: *29th International Conference on Discrete Simulation of Fluid Dynamics (DSFD)*. online.

Conference Posters

Gaedtke, M., Rau, D., Nirschl, H., and Krause, M. J. (2019d). "Umsetzung und Untersuchung thermischer Feinstrukturmodelle für die Lattice Boltzmann Methode." In: *Jahrestreffen der ProcessNet Fachgruppe Computational Fluid Dynamics*. Frankfurt, Germany.

Bibliography

Abishek, S., King, A. J. C., Mead-hunter, R., Golkarfard, V., Heikamp, W., and Mullins, B. J. (2017). "Generation and validation of virtual nonwoven , foam and knitted filter (separator / coalescer) geometries for CFD simulations." In: *Separation and Purification Technology* 188, pp. 493–507. DOI: 10.1016/j.seppur.2017.07.052.

Abishek, S., King, A. J., Nadim, N., and Mullins, B. J. (2018). "Effect of microstructure on melting in metal-foam/paraffin composite phase change materials." In: *International Journal of Heat and Mass Transfer* 127, pp. 135–144. DOI: 10.1016/j.ijheatmasstransfer.2018.07.054.

Ahmad, M., Bontemps, A., Sallée, H., and Quenard, D. (2006). "Experimental investigation and computer simulation of thermal behaviour of wallboards containing a phase change material." In: *Energy and Buildings* 38.4, pp. 357–366. DOI: 10.1016/j.enbuild.2005.07.008.

Aidun, C. K. and Clausen, J. R. (2010). "Lattice-Boltzmann Method for Complex Flows." In: *Annual Review of Fluid Mechanics* 42.1, pp. 439–472. DOI: 10.1146/annurev-fluid-121108-145519.

Akdemir, S. (2015). "Numerical Modelling and Experimental Validation of a Cold Store Ambient Factors." In: *Journal of Agricultural Sciences* 21, pp. 606–619.

Al-Alawi, B. M. and Bradley, T. H. (2013). "Review of hybrid, plug-in hybrid, and electric vehicle market modeling Studies." In: *Renewable and Sustainable Energy Reviews* 21, pp. 190–203. DOI: 10.1016/j.rser.2012.12.048.

Allen, R. and Reis, T. (2016). "Moment-based boundary conditions for lattice Boltzmann simulations of natural convection in cavities." In: *Progress in Computational Fluid Dynamics, An International Journal* 16.4, p. 216. DOI: 10.1504/PCFD.2016.077296.

Alshaer, W. G., Nada, S. A., Rady, M. A., Le Bot, C., and Palomo Del Barrio, E. (2015). "Numerical investigations of using carbon foam/PCM/Nano carbon tubes composites in thermal management of electronic equipment." In: *Energy Conversion and Management* 89, pp. 873–884. DOI: 10.1016/j.enconman.2014.10.045.

Ambaw, A., Delele, M. A., Defraeye, T., Ho, Q. T., Opara, L. U., Nicolaï, B. M., and Verboven, P. (2013). "The use of CFD to characterize and design post-harvest storage facilities: Past, present and future." In: *Computers and Electronics in Agriculture* 93, pp. 184–194. DOI: 10.1016/j.compag.2012.05.009.

Anderson, K. R., Lin, J., McNamara, C., and Magri, V. (2015). "CFD Study of Forced Air Cooling and Windage Losses in a High Speed Electric Motor." In: *Journal of Electronics Cooling and Thermal Control* 05.02, pp. 27–44. DOI: 10.4236/jectc.2015.52003.

Anisur, M. R., Mahfuz, M. H., Kibria, M. A., Saidur, R., Metselaar, I. H., and Mahlia, T. M. (2013). "Curbing global warming with phase change materials for energy storage." In: *Renewable and Sustainable Energy Reviews* 18, pp. 23–30. DOI: 10.1016/j.rser.2012.10.014.

Ansumali, S., Karlin, I. V., and Succi, S. (2004). "Kinetic theory of turbulence modeling: Smallness parameter, scaling and microscopic derivation of Smagorinsky model." In: *Physica A: Statistical Mechanics and its Applications* 338.3-4, pp. 379–394. DOI: 10.1016/j.physa.2004.02.013.

Ansys (2006). "CFX Documentation – Solver Modeling Guide." In: Release 17.

Baetens, R., Jelle, B. P., and Gustavsen, A. (2010a). "Phase change materials for building applications: A state-of-the-art review." In: *Energy and Buildings* 42.9, pp. 1361–1368. DOI: 10.1016/j.enbuild.2010.03.026.

Baetens, R., Jelle, B. P., Thue, J. V., Tenpierik, M. J., Grynning, S., Uvsløkk, S., and Gustavsen, A. (2010b). "Vacuum insulation panels for building applications: A review and beyond." In: *Energy and Buildings* 42.2, pp. 147–172. DOI: 10.1016/j.enbuild.2009.09.005.

Barad, M. F., Kocheemoolayil, J. G., and Kiris, C. C. (2017). "Lattice boltzmann and navier-stokes cartesian CFD approaches for airframe noise predictions." In: *23rd AIAA Computational Fluid Dynamics Conference, 2017* June 2017, pp. 1–16. DOI: 10.2514/6.2017-4404.

Bardina, J., Ferziger, J. H., and Reynolds, W. C. (1980). "Improved Subgrid-Scale Models for Large-Eddy Simulation." In: *AIAA Paper*. DOI: 10.2514/6.1980-1357.

Bartoloni, A., Battista, C., Cabasino, S., Paolucci, P. S., Pech, J., Sarno, R., Todesco, G. M., Torelli, M., Tross, W., Vicini, P., Benzi, R., Cabibbo, N., Mas-

saioli, F., and Tripiccione, R. (1993). "LBE Simulations of Rayleigh-Bénard Convection on the Ape100 Parallel Processor." In: *International Journal of Modern Physics C* 04.05, pp. 993–1006. DOI: 10.1142/s012918319300077x.

Bauer, M. and Rüde, U. (2018). *An improved lattice Boltzmann D3Q19 method based on an alternative equilibrium discretization*. URL: http://arxiv.org/abs/1803.04937.

Becker, K. M. and Kaye, J. (1962). "The influence of a radial temperature gradient on the instability of fluid flow in an annulus with an inner rotating cylinder." In: *Journal of Heat Transfer* 84.2, pp. 106–110. DOI: 10.1115/1.3684306.

Becker, K. M. (1957). *An experimental and theoretical study of heat transfer in an annulus with an inner rotating cylinder*. Tech. rep. Massachusetts Institute of Technology.

Bhatnagar, P. L., Gross, E. P., and Krook, M. (1954). "A model for collision processes in gases. I. Small amplitude processes in charged and neutral one-component systems." In: *Physical Review* 94.3, pp. 511–525. DOI: 10.1103/PhysRev.94.511.

Bista, S., Hosseini, S. E., Owens, E., and Phillips, G. (2018). "Performance improvement and energy consumption reduction in refrigeration systems using phase change material (PCM)." In: *Applied Thermal Engineering* 142.April, pp. 723–735. DOI: 10.1016/j.applthermaleng.2018.07.068.

Bouquerel, M., Duforestel, T., Baillis, D., and Rusaouen, G. (2012). "Heat transfer modeling in vacuum insulation panels containing nanoporous silicas - A review." In: *Energy and Buildings* 54, pp. 320–336. DOI: 10.1016/j.enbuild.2012.07.034.

Bouzidi, M., Firdaouss, M., and Lallemand, P. (2001). "Momentum transfer of a Boltzmann-lattice fluid with boundaries." In: *Physics of Fluids* 13.11, pp. 3452–3459. DOI: 10.1063/1.1399290.

Brand, A., Allen, L., Altman, M., Hlava, M., and Scott, J. (2015). "Beyond authorship: Attribution, contribution, collaboration, and credit." In: *Learned Publishing* 28.2, pp. 151–155. DOI: 10.1087/20150211.

Brent, R. P. (1971). "An algorithm with guaranteed convergence for finding a zero of a function." In: *The Computer Journal* 14.4, pp. 422–425. DOI: 10.1093/comjnl/14.4.422.

Cardinale, T., De Fazio, P., and Grandizio, F. (2016). "Numerical and Experimental Computation of Airflow in a Transport Container." In: *International Journal of Heat and Technology* 34.4, pp. 734–742. DOI: 10.18280/ijht.340426.

Chai, Z. and Zhao, T. S. (2013). "Lattice Boltzmann model for the convection-diffusion equation." In: *Physical Review E - Statistical, Nonlinear, and Soft Matter Physics* 87.6, pp. 1–15. DOI: 10.1103/PhysRevE.87.063309.

Chai, Z. and Zhao, T. S. (2014). "Nonequilibrium scheme for computing the flux of the convection-diffusion equation in the framework of the lattice Boltzmann method." In: *Physical Review E - Statistical, Nonlinear, and Soft Matter Physics* 90.1, pp. 1–15. DOI: 10.1103/PhysRevE.90.013305.

Chandra, L., Roelofs, F., and Komen, E. M. J. (2010). *Unsteady RANS and LES A nalyses of Hooper ' s Hydraulics Experiment in a Tight Lattice Bare Rod-bundle*.

Chatterjee, D. and Chakraborty, S. (2005). "An enthalpy-based lattice Boltzmann model for diffusion dominated solid-liquid phase transformation." In: *Physics Letters, Section A: General, Atomic and Solid State Physics* 341.1-4, pp. 320–330. DOI: 10.1016/j.physleta.2005.04.080.

Chen, C., Zhang, H., Gao, X., Xu, T., Fang, Y., and Zhang, Z. (2016). "Numerical and experimental investigation on latent thermal energy storage system with spiral coil tube and paraffin/expanded graphite composite PCM." In: *Energy Conversion and Management* 126, pp. 889–897. DOI: 10.1016/j.enconman.2016.08.068.

Chen, H., Kandasamy, S., Orszag, S., Shock, R., Succi, S., and Yakhot, V. (2003). "Extended Boltzmann kinetic equation for turbulent flows." In: *Science* 301.5633, pp. 633–636. DOI: 10.1126/science.1085048.

Chen, S. (2012). "Simulating Turbulent Buoyant Flow by a Simple LES-Based Thermal Lattice Boltzmann Model." In: *ISRN Thermodynamics* 2012, pp. 1–9. DOI: 10.5402/2012/253972.

Chen, S., G.d Doolen, and Doolen, G. D. (1998). "Lattice Boltzmann method for fluid flows." In: *Annual Review of Fluid Mechanics* 30.1, pp. 329–364. DOI: 10.1146/annurev.fluid.30.1.329.

Chen, X., Xia, X. L., Wang, F. Q., Sun, C., and Liu, R. Q. (2019). "Analysis of a latent heat thermal energy storage unit with metal foam insert in both the HTF and PCM sides." In: *IOP Conference Series: Earth and Environmental Science* 354.1. DOI: 10.1088/1755-1315/354/1/012020.

Coles, D. (1965). "Transition in circular Couette flow." In: *Journal of Fluid Mechanics* 21.3, pp. 385–425. DOI: 10.1017/S0022112065000241.

Coreixas, C., Chopard, B., and Latt, J. (2019). "Comprehensive comparison of collision models in the lattice Boltzmann framework: Theoretical investigations." In: *Physical Review E* 100.3. DOI: 10.1103/PhysRevE.100.033305.

D'Orazio, A. and Succi, S. (2003). "Boundary Conditions for Thermal Lattice Boltzmann Simulations." In: *Computational Science – ICCS 2003*, pp. 977–986. DOI: 10.1007/3-540-44860-8_101.

Dahmen, N., Abeln, J., Eberhard, M., Kolb, T., Leibold, H., Sauer, J., Stapf, D., and Zimmerlin, B. (2017). "The bioliq process for producing synthetic transportation fuels." In: *Wiley Interdisciplinary Reviews: Energy and Environment* 6.3. DOI: 10.1002/wene.236.

Davis, B. A. and Figliozzi, M. A. (2013). "A methodology to evaluate the competitiveness of electric delivery trucks." In: *Transportation Research Part E: Logistics and Transportation Review* 49.1, pp. 8–23. DOI: 10.1016/j.tre.2012.07.003.

De Fabritiis, G., Mancini, A., Mansutti, D., and Succi, S. (1998). "Mesoscopic models of liquid/solid phase transitions." In: *International Journal of Modern Physics C* 9.8, pp. 1405–1415. DOI: 10.1142/S0129183198001278.

De Rosis, A. and Luo, K. H. (2019). "Role of higher-order Hermite polynomials in the central-moments-based lattice Boltzmann framework." In: *Physical Review E* 99.1, pp. 1–8. DOI: 10.1103/PhysRevE.99.013301.

De Vahl Davis, G. (1983). "Natural convection of air in a square cavity: A bench mark numerical solution." In: *International Journal for Numerical Methods in Fluids* 3.3, pp. 249–264. DOI: 10.1002/fld.1650030305.

Deaconu, A. S., Chirile, A. I., and Deaconu, I. D. (2015). "Air-gap heat transfer of a permanent magnet synchronous motor." In: *Revue Roumaine des Sciences Techniques Serie Electrotechnique et Energetique* 60.3, pp. 263–272.

Defraeye, T., Blocken, B., and Carmeliet, J. (2010). "CFD analysis of convective heat transfer at the surfaces of a cube immersed in a turbulent boundary layer." In: *International Journal of Heat and Mass Transfer* 53.1, pp. 297–308. DOI: https://doi.org/10.1016/j.ijheatmasstransfer.2009.09.029.

Delele, M. A., Schenk, A., Tijskens, E., Ramon, H., Nicolaï, B. M., and Verboven, P. (2009). "Optimization of the humidification of cold stores by pressurized water atomizers based on a multiscale CFD model." In: *Journal of Food Engineering* 91.2, pp. 228–239. DOI: https://doi.org/10.1016/j.jfoodeng.2008.08.027.

Dellar, P. J. (2001). "Bulk and shear viscosities in lattice Boltzmann equations." In: *Physical Review E* 64.3, p. 031203. DOI: 10.1103/PhysRevE.64.031203.

Dellar, P. J. (2014). "Lattice Boltzmann algorithms without cubic defects in Galilean invariance on standard lattices." In: *Journal of Computational Physics* 259.2, pp. 270–283. DOI: 10.1016/j.jcp.2013.11.021.

Demirbaş, A. (2006). "Global renewable energy resources." In: *Energy Sources, Part A: Recovery, Utilization and Environmental Effects* 28.8, pp. 779–792. DOI: 10.1080/00908310600718742.

Dharmarathne, S., Tutkun, M., Araya, G., and Castillo, L. (2016). "Structures of scalar transport in a turbulent channel." In: *European Journal of Mechanics, B/Fluids* 55, pp. 259–271. DOI: 10.1016/j.euromechflu.2015.06.010.

DIN 8959 (2000). *Wärmegedämmte Beförderungsmitteln für Lebensmittel – Anforderungen und Prüfung*. Beuth-Verlag. DOI: 10.31030/9010093.

Dinesh, B. V. S. and Bhattacharya, A. (2019). "Effect of foam geometry on heat absorption characteristics of PCM-metal foam composite thermal energy storage systems." In: *International Journal of Heat and Mass Transfer* 134, pp. 866–883. DOI: 10.1016/j.ijheatmasstransfer.2019.01.095.

Dinesh, B. V. S. and Bhattacharya, A. (2020). "Comparison of energy absorption characteristics of PCM-metal foam systems with different pore size distributions." In: *Journal of Energy Storage* 28.December 2019, p. 101190. DOI: 10.1016/j.est.2019.101190.

Dixit, H. N. and Babu, V. (2006). "Simulation of high Rayleigh number natural convection in a square cavity using the lattice Boltzmann method." In: *International Journal of Heat and Mass Transfer* 49, pp. 727–739. DOI: j.ijheatmasstransfer.2005.07.046.

Dong, Y.-H., Sagaut, P., and Marie, S. (2008). "Inertial consistent subgrid model for large-eddy simulation based on the lattice Boltzmann method." In: *Physics of Fluids* 20.3, p. 35104. DOI: 10.1063/1.2842379.

Drissi, S., Ling, T.-c., and Mo, K. H. (2019). "Thermal Efficiency and Durability Performances of Paraffinic Phase Change Materials with Enhanced Thermal Conductivity–A Review." In: *Thermochimica Acta*. DOI: 10.1016/j.tca.2019.01.020.

Dutil, Y., Rousse, D. R., Salah, N. B., Lassue, S., and Zalewski, L. (2011). "A review on phase-change materials: Mathematical modeling and simulations." In: *Renewable and Sustainable Energy Reviews* 15.1, pp. 112–130. DOI: 10.1016/j.rser.2010.06.011.

Eberhardt, H.-f. (2005). "Vom Pulver zur Paneele – Wie entsteht ein VIP?" In: *VIP-Bau: 2. Fachtagung – Erfahrungen aus der Praxis*, pp. 1–9.

Eggels, J. G. and Somers, J. A. (1995). "Numerical simulation of free convective flow using the lattice-Boltzmann scheme." In: *International Journal of Heat and Fluid Flow* 16.5, pp. 357–364. DOI: 10.1016/0142-727X(95)00052-R.

Eidson, T. M. (1985). “Numerical simulation of the turbulent Rayleigh-Bénard problem using subgrid modelling.” In: *Journal of Fluid Mechanics* 158, pp. 245–268. DOI: 10.1017/S0022112085002634.

Elgar, E. C. (1956). “Fluid flow and heat transfer in an annulus with an inner rotating cylinder.” PhD thesis. Massachusetts Institute of Technology.

European Commision (2012). “Energy Roadmap 2050.” In: *Policy* April, pp. 1–9. DOI: 10.2833/10759.

Fan, L. and Khodadadi, J. (2011). “Thermal conductivity enhancement ofphase change materials for thermal energy storage: A review.” In: *Renewable and Sustainable Energy Reviews* 15.1, pp. 24–46. DOI: 10.1016/j.rser.2010.08.007.

Fardin, M. A., Perge, C., and Taberlet, N. (2014). “"the hydrogen atom of fluid dynamics"-introduction to the Taylor-Couette flow for soft matter scientists.” In: *Soft Matter* 10.20, pp. 3523–3535. DOI: 10.1039/c3sm52828f.

Farid, M. M., Khudhair, A. M., Ali, S., and Razack, K. (2004). “A review on phase change energy storage : materials and applications.” In: 45, pp. 1597–1615. DOI: 10.1016/j.enconman.2003.09.015.

Feichtinger, C., Götz, J., Donath, S., Iglberger, K., and Rüde, U. (2009). “WaLBerla: Exploiting Massively Parallel Systems for Lattice Boltzmann Simulations Christian.” In: *Parallel Computing: Numerics, Applications, and Trends*, pp. 241–260. DOI: 10.1007/978-1-84882-409-6.

Fénot, M., Bertin, Y., Dorignac, E., and Lalizel, G. (2011). “A review of heat transfer between concentric rotating cylinders with or without axial flow.” In: *International Journal of Thermal Sciences* 50.7, pp. 1138–1155. DOI: 10.1016/j.ijthermalsci.2011.02.013.

Ferziger, J. and Peric, M. (2008). *Numerische Strömungsmechanik*. 1st ed. Springer-Verlag Berlin Heidelberg, p. 509. DOI: 10.1007/978-3-540-68228-8.

Ferzinger, J. H. and Perić, M. (2002). *Computational Methods for Fluid Dynamics*. Springer Berlin Heidelberg, p. 425.

Fietz, J., Krause, M. J., Schulz, C., Sanders, P., and Heuveline, V. (2012). “Optimized hybrid parallel lattice Boltzmann fluid flow simulations on complex geometries.” In: *Lecture Notes in Computer Science* 7484 LNCS, pp. 818–829. DOI: 10.1007/978-3-642-32820-6_81.

Fröhlich, J. (2006). *Large Eddy Simulation turbulenter Strömungen*. Vol. 1. Springer. DOI: 10.1007/978-3-8351-9051-1.

Fröhlich, J. and Terzi, D. von (2008). “Hybrid LES/RANS methods for the simulation of turbulent flows.” In: *Progress in Aerospace Sciences* 44.5, pp. 349–377. DOI: 10.1016/j.paerosci.2008.05.001.

Gau, C. and Viskanta, R. (1986). "Melting and solidification of a pure metal on a vertical wall." In: *Journal of Heat Transfer* 108.1, pp. 174–181. DOI: 10.1115/1.3246884.

Gazley, G. (1958). "Heat-Transfer Characteristics of the Rotational and Axial Flow Between Concentric Cylinders." In: *Transactions of the ASME* 80, pp. 79–90.

Geier, M., Pasquali, A., and Schönherr, M. (2017). "Parametrization of the cumulant lattice Boltzmann method for fourth order accurate diffusion part I: Derivation and validation." In: *Journal of Computational Physics* 348, pp. 862–888. DOI: 10.1016/j.jcp.2017.05.040.

Geier, M., Schönherr, M., Pasquali, A., and Krafczyk, M. (2015). "The cumulant lattice Boltzmann equation in three dimensions: Theory and validation." In: *Computers and Mathematics with Applications* 70.4, pp. 507–547. DOI: 10.1016/j.camwa.2015.05.001.

Getahun, S., Ambaw, A., Delele, M., Meyer, C. J., and Opara, U. L. (2017). "Analysis of airflow and heat transfer inside fruit packed refrigerated shipping container: Part I - Model development and validation." In: *Journal of Food Engineering* 203, pp. 58–68. DOI: 10.1016/j.jfoodeng.2017.02.010.

Grad, H. (1949). "Note on N-dimensional hermite polynomials." In: *Communications on Pure and Applied Mathematics* 2.4, pp. 325–330. DOI: 10.1002/cpa.3160020402.

Grossmann, S., Lohse, D., and Sun, C. (2016). "High-Reynolds Number Taylor-Couette Turbulence." In: *Annual Review of Fluid Mechanics* 48.2016, pp. 53–80. DOI: 10.1146/annurev-fluid-122414-034353.

Guo, Z., Shi, B., and Wang, N. (2000). "Lattice BGK Model for Incompressible Navier–Stokes Equation." In: *Journal of Computational Physics* 165.1, pp. 288–306. DOI: 10.1006/jcph.2000.6616.

Guo, Z., Shi, B., and Zheng, C. (2002a). "A coupled lattice BGK model for the Boussinesq equations." In: *International Journal for Numerical Methods in Fluids* 39.4, pp. 325–342. DOI: 10.1002/fld.337.

Guo, Z., Zheng, C., and Shi, B. (2002b). "An extrapolation method for boundary conditions in lattice Boltzmann method." In: *Physics of Fluids* 14.6, pp. 2007–2010. DOI: 10.1063/1.1471914.

Guo, Z., Zheng, C., and Shi, B. (2002c). "Discrete lattice effects on the forcing term in the lattice Boltzmann method." In: *Physical Review E - Statistical, Nonlinear, and Soft Matter Physics* 65.4, p. 46308. DOI: 10.1103/PhysRevE.65.046308.

Guo, Z., Zheng, C., Shi, B., and Zhao, T. S. (2007). "Thermal lattice Boltzmann equation for low Mach number flows: Decoupling model." In: *Physical Review E - Statistical, Nonlinear, and Soft Matter Physics* 75.3, pp. 1–15. DOI: 10.1103/PhysRevE.75.036704.

Hager, G. and Wellein, G. (2010). *Introduction to high performance computing for scientists and engineers*, pp. 1–323. DOI: 10.1201/EBK1439811924.

Haller, G. (2005). "An objective definition of a vortex." In: *Journal of Fluid Mechanics* 525, pp. 1–26. DOI: 10.1017/S0022112004002526.

Han, B., Choi, J. H., Dantzig, J. A., and Bischof, J. C. (2006). "A quantitative analysis on latent heat of an aqueous binary mixture." In: *Cryobiology* 52, pp. 146–151. DOI: 10.1016/j.cryobiol.2005.09.007.

Hänel, D. (2004). *Molekulare Gasdynamik*. Springer-Verlag, p. 223. DOI: 10.1007/3-540-35047-0.

Hanjalić, K. (2002). "One-point closure models for buoyancy-driven turbulent flow." In: *Annual Review of Fluid Mechanics* 34.1, pp. 321–347. DOI: 10.1146/annurev.fluid.34.082801.161035.

Hanjalić, K. and Vasić, S. (1993). "Computation of turbulent natural convection in rectangular enclosures with an algebraic flux model." In: *International Journal of Heat and Mass Transfer* 36.14, pp. 3603–3624. DOI: 10.1016/0017-9310(93)90178-9.

Hannan, M. A., Hoque, M. M., Mohamed, A., and Ayob, A. (2017). "Review of energy storage systems for electric vehicle applications: Issues and challenges." In: *Renewable and Sustainable Energy Reviews* 69.November 2016, pp. 771–789. DOI: 10.1016/j.rser.2016.11.171.

Hao, X. H. and Ju, Y. L. (2011). "Simulation and analysis on the flow field of the low temperature mini-type cold store." In: *Heat Mass Transfer*. DOI: 10.1007/s00231-011-0764-1.

Haussmann, M., Barreto, A. C., Kouyi, G. L., Rivière, N., Nirschl, H., and Krause, M. J. (2019). "Large-eddy simulation coupled with wall models for turbulent channel flows at high Reynolds numbers with a lattice Boltzmann method — Application to Coriolis mass flowmeter." In: *Computers & Mathematics with Applications* 78.10, pp. 3285–3302. DOI: 10.1016/j.camwa.2019.04.033.

Haussmann, M., Ries, F., Jeppener-Haltenhoff, J. B., Li, Y., Schmidt, M., Welch, C., Illmann, L., Böhm, B., Nirschl, H., Krause, M. J., and Sadiki, A. (2020). "Evaluation of a Near-Wall-Modeled Large Eddy Lattice Boltzmann Method for the Analysis of Complex Flows Relevant to IC Engines." In: *Computation* 8.2, p. 43. DOI: 10.3390/computation8020043.

He, Y. L., Liu, Q., Li, Q., and Tao, W. Q. (2019). "Lattice Boltzmann methods for single-phase and solid-liquid phase-change heat transfer in porous media: A review." In: *International Journal of Heat and Mass Transfer* 129, pp. 160–197. DOI: 10.1016/j.ijheatmasstransfer.2018.08.135.

Henn, T., Thäter, G., Dörfler, W., Nirschl, H., and Krause, M. J. (2016). "Parallel dilute particulate flow simulations in the human nasal cavity." In: *Computers & Fluids* 124, pp. 197–207. DOI: 10.1016/j.compfluid.2015.08.002.

Heuveline, V. and Krause, M. J. (2011). "OpenLB: Towards an Efficient Parallel Open Source Library for Lattice Boltzmann Fluid Flow Simulations." In: *PARA'08 Workshop on State-of-the-Art in Scientific and Parallel Computing, May 13-16, 2008*. 6126, 6127.

Ho, S. H., Rosario, L., and Rahman, M. M. (2010). "Numerical simulation of temperature and velocity in a refrigerated warehouse." In: *International Journal of Refrigeration* 33.5, pp. 1015–1025. DOI: 10.1016/j.ijrefrig.2010.02.010.

Hoang, H. M., Duret, S., Flick, D., and Laguerre, O. (2015). "Preliminary study of airflow and heat transfer in a cold room filled with apple pallets: Comparison between two modelling approaches and experimental results." In: *Applied Thermal Engineering* 76, pp. 367–381. DOI: 10.1016/j.applthermaleng.2014.11.012.

Holdych, D. J., Noble, D. R., Georgiadis, J. G., and Buckius, R. O. (2004). "Truncation error analysis of lattice Boltzmann methods." In: *Journal of Computational Physics* 193.2, pp. 595–619. DOI: 10.1016/j.jcp.2003.08.012.

Hortmann, M., Perić, M., and Scheuerer, G. (1990). "Finite volume multigrid prediction of laminar natural convection: Bench-mark solutions." In: *International Journal for Numerical Methods in Fluids* 11.2, pp. 189–207. DOI: 10.1002/fld.1650110206.

Hosain, M. L., Fdhila, R. B., and Rönnberg, K. (2017). "Air-gap Flow and Thermal Analysis of Rotating Machines using CFD." In: *Energy Procedia* 105, pp. 5153–5159. DOI: 10.1016/j.egypro.2017.03.1045.

Hou, S., Sterling, J., Chen, S., and Doolen, G. D. (1994). "A lattice Boltzmann subgrid model for high Reynolds number flows." In: *arXiv preprint comp-gas/9401004*, pp. 1–18.

Howey, D. A., Childs, P. R. N., and Holmes, A. S. (2012). "Air-Gap Convection in Rotating Electrical Machines." In: *IEEE Transactions on Industrial Electronics* 59.3, pp. 1367–1375. DOI: 10.1109/TIE.2010.2100337.

Hu, Y., Li, D., Shu, S., and Niu, X. (2017). "Lattice Boltzmann simulation for three-dimensional natural convection with solid-liquid phase change." In:

International Journal of Heat and Mass Transfer 113, pp. 1168–1178. DOI: 10.1016/j.ijheatmasstransfer.2017.05.116.

Huang, H., Lee, T. S., and Shu, C. (2006). "Thermal curved boundary treatment for the thermal lattice Boltzmann equation." In: *International Journal of Modern Physics C* 17.5, pp. 631–643. DOI: 10.1142/S0129183106009059.

Huang, R. and Wu, H. (2015). "Phase interface effects in the total enthalpy-based lattice Boltzmann model for solid-liquid phase change." In: *Journal of Computational Physics* 294, pp. 346–362. DOI: 10.1016/j.jcp.2015.03.064.

Huang, R., Wu, H., and Cheng, P. (2013). "A new lattice Boltzmann model for solid-liquid phase change." In: *International Journal of Heat and Mass Transfer* 59.1, pp. 295–301. DOI: 10.1016/j.ijheatmasstransfer.2012.12.027.

International Energy Agency (1998). *World Energy Outlook 1998*. IEA/OECD.

Jacob, J., Malaspinas, O., and Sagaut, P. (2019). "A new hybrid recursive regularised bhatnagar–gross–krook collision model for lattice boltzmann method-based large eddy simulation." In: *Journal of Turbulence* 19.11, pp. 1051–1076. DOI: 10.1080/14685248.2018.1540879.

Jahanshaloo, L., Pouryazdanpanah, E., and Che Sidik, N. A. (2013). "A review on the application of the lattice boltzmann method for turbulent flow simulation." In: *Numerical Heat Transfer; Part A: Applications* 64.11, pp. 938–953. DOI: 10.1080/10407782.2013.807690.

James, S. J., James, C., and Evans, J. A. (2006). "Modelling of food transportation systems: a review." In: *International Journal of Refrigeration* 29, pp. 947–957. DOI: 10.1016/j.ijrefrig.2006.03.017.

Jeffreys, H. (1928). "Some Cases of Instability in Fluid Motion." In: *Proceedings of the Royal Society of London A: Mathematical, Physical and Engineering Sciences* 118.779, pp. 195–208. DOI: 10.1098/rspa.1928.0045.

Jiaung, W. S., Ho, J. R., Kuo, C. P., and Wen-Shu Jiaung, Jeng-Rong Ho, Chun- (2001). "Lattice Boltzmann method for the heat conduction problem with phase change." In: *Numerical Heat Transfer, Part B: Fundamentals* 39.2, pp. 167–187. DOI: 10.1080/10407790150503495.

Junk, M. and Yang, Z. (2008). "Outflow boundary conditions for the lattice Boltzmann method." In: *Progress in Computational Fluid Dynamics* 8.1-4, pp. 38–48. DOI: 10.1504/PCFD.2008.018077.

Kalnæs, S. E. and Jelle, B. P. (2014). "Vacuum insulation panel products: A state-of-the-art review and future research pathways." In: *Applied Energy* 116.7465, pp. 355–375. DOI: 10.1016/j.apenergy.2013.11.032.

Karlin, I. V., Bösch, F., and Chikatamarla, S. S. (2014). "Gibbs' principle for the lattice-kinetic theory of fluid dynamics." In: *Physical Review E - Statistical,*

Nonlinear, and Soft Matter Physics 90.3, pp. 1–5. DOI: 10.1103/PhysRevE.90.031302.

Kasaeian, A., Bahrami, L., Pourfayaz, F., Khodabandeh, E., and Yan, W. M. (2017). "Experimental studies on the applications of PCMs and nano-PCMs in buildings: A critical review." In: *Energy and Buildings* 154, pp. 96–112. DOI: 10.1016/j.enbuild.2017.08.037.

Katz, V. J. (1979). "The History of Stokes' Theorem." In: *Mathematics Magazine* 52.3, p. 146. DOI: 10.2307/2690275.

Khan, M. A. I., Delbosc, N., Noakes, C. J., and Summers, J. (2015). "Real-time flow simulation of indoor environments using lattice Boltzmann method." In: *Building Simulation*. Vol. 8. 4. Tsinghua University Press, pp. 405–414. DOI: 10.1007/s12273-015-0232-9.

Körner, C., Thies, M., Hofmann, T., Thürey, N., and Rüde, U. (2005). "Lattice Boltzmann model for free surface flow for modeling foaming." In: *Journal of Statistical Physics* 121.1-2, pp. 179–196. DOI: 10.1007/s10955-005-8879-8.

Krafczyk, M., Tölke, J., and Luo, L.-s. (2003). "Large eddy simulation with a multiple-relaxation-time LBE model." In: *International Journal of Modern Physics B* 17, pp. 33–39. DOI: 10.1142/S0217979203017059.

Krastins, I., Kao, A., Pericleous, K., and Reis, T. (2020). "Moment-based boundary conditions for straight on-grid boundaries in three-dimensional lattice Boltzmann simulations." In: *International Journal for Numerical Methods in Fluids* May, fld.4856. DOI: 10.1002/fld.4856.

Krause, M. J., Gengenbach, T., and Heuveline, V. (2011). "Hybrid parallel simulations of fluid flows in complex geometries: Application to the human lungs." In: *Lecture Notes in Computer Science (including subseries Lecture Notes in Artificial Intelligence and Lecture Notes in Bioinformatics)*. Vol. 6586 LNCS, pp. 209–216. DOI: 10.1007/978-3-642-21878-1_26.

Krause, M. J., Thäter, G., and Heuveline, V. (2013). "Adjoint-based fluid flow control and optimisation with lattice Boltzmann methods." In: *Computers & Mathematics with Applications* 65.6, pp. 945–960. DOI: 10.1016/j.camwa.2012.08.007.

Krüger, T., Kusumaatmaja, H., Kuzmin, A., Shardt, O., Silva, G., and Viggen, E. (2017). *The Lattice Boltzmann Method: Principles and Practice*. Springer International Publishing. DOI: 10.1007/978-3-319-44649-3.

Krüger, T., Varnik, F., and Raabe, D. (2010). "Second-order convergence of the deviatoric stress tensor in the standard Bhatnagar-Gross-Krook lattice Boltzmann method." In: *Physical Review E - Statistical, Nonlinear, and Soft Matter Physics* 82.2, pp. 1–4. DOI: 10.1103/PhysRevE.82.025701.

Kumar, V., Durst, F., and Ray, S. (2006). *Modeling moving-boundary problems of solidification and melting adopting an arbitrary lagrangian-eulerian approach*. Vol. 49. 4, pp. 299–331. DOI: 10.1080/10407790500379981.

Kwon, J. S., Jang, C. H., Jung, H., and Song, T. H. (2009). "Effective thermal conductivity of various filling materials for vacuum insulation panels." In: *International Journal of Heat and Mass Transfer* 52.23-24, pp. 5525–5532. DOI: 10.1016/j.ijheatmasstransfer.2009.06.029.

Lallemand, P. and Luo, L. S. (2000). "Theory of the lattice Boltzmann method: Dispersion, dissipation, isotropy, Galilean invariance, and stability." In: *Physical Review E - Statistical Physics, Plasmas, Fluids, and Related Interdisciplinary Topics* 61.6, pp. 6546–6562. DOI: 10.1103/PhysRevE.61.6546.

Latt, J. and Chopard, B. (2006). "Lattice Boltzmann method with regularized pre-collision distribution functions." In: *Mathematics and Computers in Simulation* 72.2-6, pp. 165–168. DOI: 10.1016/j.matcom.2006.05.017.

Latt, J., Chopard, B., Malaspinas, O., Deville, M., and Michler, A. (2008). "Straight velocity boundaries in the lattice Boltzmann method." In: *Physical Review E - Statistical, Nonlinear, and Soft Matter Physics* 77.5, p. 56703. DOI: 10.1103/PhysRevE.77.056703.

Launder, B. E. (1988). "On the computation of convection heat transfer in complex turbulent flows." In: *Journal of Heat Transfer* 110.4.

Le Quéré, P. (1991). "Accurate solutions to the square thermally driven cavity at high Rayleigh number." In: *Computers & Fluids* 20.1, pp. 29–41.

Leonard, A. (1975). *Energy cascade in large-eddy simulations of turbulent fluid flows*. DOI: 10.1016/S0065-2687(08)60464-1.

Lerner, R. G. and Trigg, G. L. (2005). *Encyclopedia of Physics*. 3rd ed. Wiley-VCH Verlag GmbH & Co. KGaA.

Lewis, J. W. (1928). "An Experimental Study of the Motion of a Viscous Liquid Contained between Two Coaxial Cylinders." In: *Proceedings of the Royal Society of London. Series A, Containing Papers of a Mathematical and Physical Character* Vol. 117.No. 777, pp. 388–407.

Lewis, M. B. (1975). "Kinetic theory of turbulent flows." In: *Physics of Fluids* 18.3, pp. 313–319. DOI: 10.1063/1.861139.

Li, L., Chen, C., Mei, R., and Klausner, J. F. (2014a). "Conjugate heat and mass transfer in the lattice Boltzmann equation method." In: *Physical Review E* 89.4, p. 043308. DOI: 10.1103/PhysRevE.89.043308.

Li, L., Mei, R., and Klausner, J. F. (2017). "Lattice Boltzmann models for the convection-diffusion equation: D2Q5 vs D2Q9." In: *International*

Journal of Heat and Mass Transfer 108, Part, pp. 41–62. DOI: 10.1016/j.ijheatmasstransfer.2016.11.092.

Li, L., Mei, R., and Klausner, J. F. (2013). "Boundary conditions for thermal lattice Boltzmann equation method." In: *Journal of Computational Physics* 237, pp. 366–395. DOI: 10.1016/j.jcp.2012.11.027.

Li, L., Mei, R., and Klausner, J. F. (2014b). "Heat transfer evaluation on curved boundaries in thermal lattice boltzmann equation method." In: *Journal of Heat Transfer* 136.1, pp. 1–14. DOI: 10.1115/1.4025046.

Lim, C. Y., Shu, C., Niu, X. D., and Chew, Y. T. (2002). "Application of lattice Boltzmann method to simulate microchannel flows." In: *Physics of Fluids* 14.7, pp. 2299–2308. DOI: 10.1063/1.1483841.

Lin, L. S., Chang, H. W., and Lin, C. A. (2013). "Multi relaxation time lattice Boltzmann simulations of transition in deep 2D lid driven cavity using GPU." In: *Computers & Fluids* 80.1, pp. 381–387. DOI: 10.1016/j.compfluid.2012.01.018.

Liou, T. M. and Wang, C. S. (2018). "Large eddy simulation of rotating turbulent flows and heat transfer by the lattice Boltzmann method." In: *Physics of Fluids* 30.1. DOI: 10.1063/1.5005901.

Liu, C.-H., Lin, K.-H., Mai, H.-C., and Lin, C.-A. (2010). "Thermal boundary conditions for thermal lattice Boltzmann simulations." In: *Computers & Mathematics with Applications* 59.7, pp. 2178–2193. DOI: 10.1016/j.camwa.2009.08.043.

Liu, H., Zou, C., Shi, B., Tian, Z., Zhang, L., and Zheng, C. (2006). "Thermal lattice-BGK model based on large-eddy simulation of turbulent natural convection due to internal heat generation." In: *International Journal of Heat and Mass Transfer* 49.23-24, pp. 4672–4680. DOI: 10.1016/j.ijheatmasstransfer.2006.03.038.

Liu, L., Su, D., Tang, Y., and Fang, G. (2016). "Thermal conductivity enhancement of phase change materials for thermal energy storage: A review." In: *Renewable and Sustainable Energy Reviews* 62, pp. 305–317. DOI: 10.1016/j.rser.2016.04.057.

Liu, M., Chen, X. P., and Premnath, K. N. (2012a). "Comparative study of the large eddy simulations with the lattice Boltzmann method using the wall-adapting local eddy-viscosity and Vreman subgrid scale models." In: *Chinese Physics Letters* 29.10. DOI: 10.1088/0256-307X/29/10/104706.

Liu, M., Saman, W., and Bruno, F. (2012b). "Development of a novel refrigeration system for refrigerated trucks incorporating phase change material." In: *Applied Energy* 92, pp. 336–342. DOI: 10.1016/j.apenergy.2011.10.015.

Liu, Q., Feng, X. B., He, Y. L., Lu, C. W., and Gu, Q. H. (2019). "Three-dimensional multiple-relaxation-time lattice Boltzmann models for single-phase and solid-liquid phase-change heat transfer in porous media at the REV scale." In: *Applied Thermal Engineering* 152.November 2018, pp. 319–337. DOI: 10.1016/j.applthermaleng.2019.02.057.

Löhner, R. (2019). "Towards overcoming the LES crisis." In: *International Journal of Computational Fluid Dynamics* 33.3, pp. 87–97. DOI: 10.1080/10618562.2019.1612052.

Lorenzati, A., Fantucci, S., Capozzoli, A., and Perino, M. (2017). "The Effect of Temperature on Thermal Performance of Fumed Silica Based Vacuum Insulation Panels for Buildings." In: *Energy Procedia* 111.September 2016, pp. 490–499. DOI: 10.1016/j.egypro.2017.03.211.

Lu, J. H., Lei, H. Y., and Dai, C. S. (2019). "An optimal two-relaxation-time lattice Boltzmann equation for solid-liquid phase change: The elimination of unphysical numerical diffusion." In: *International Journal of Thermal Sciences* 135.April 2018, pp. 17–29. DOI: 10.1016/j.ijthermalsci.2018.08.039.

Lundgren, T. S. (1967). "Distribution functions in the statistical theory of turbulence." In: *Physics of Fluids* 10.5, pp. 969–975. DOI: 10.1063/1.1762249.

Mahlia, T. M. I., Saktisahdan, T. J., Jannifar, A., Hasan, M. H., and Matseelar, H. S. C. (2014). "A review of available methods and development on energy storage ; technology update." In: *Renewable and Sustainable Energy Reviews* 33, pp. 532–545. DOI: 10.1016/j.rser.2014.01.068.

Malaspinas, O. and Sagaut, P. (2014). "Wall model for large-eddy simulation based on the lattice Boltzmann method." In: *Journal of Computational Physics* 275, pp. 25–40. DOI: 10.1016/j.jcp.2014.06.020.

Malaspinas, O. (2015). "Increasing stability and accuracy of the lattice Boltzmann scheme: recursivity and regularization." In: pp. 1–31.

Malaspinas, O. and Sagaut, P. (2011). "Advanced large-eddy simulation for lattice Boltzmann methods: The approximate deconvolution model." In: *Physics of Fluids* 23.10. DOI: 10.1063/1.3650422.

Malaspinas, O. and Sagaut, P. (2012). "Consistent subgrid scale modelling for lattice Boltzmann methods." In: *Journal of Fluid Mechanics* 700.April, pp. 514–542. DOI: 10.1017/jfm.2012.155.

Markatos, N. C. (1983). "Laminar and Turbulent Natural Convection in an Enclosed Cavity." In: *International Journal of Heat and Mass Transfer* 27.5, pp. 755–772. DOI: 10.1016/0021-9991(84)90123-2.

Marques, A. C., Davies, G. F., Evans, J. A., Maidment, G. G., and Wood, I. D. (2013). "Theoretical modelling and experimental investigation of a thermal

energy storage refrigerator." In: *Energy* 55, pp. 457–465. DOI: 10.1016/j.energy.2013.03.091.

Menter, F. R. (1994). "Two-equation eddy-viscosity turbulence models for engineering applications." In: *AIAA Journal* 32.8, pp. 1598–1605. DOI: 10.2514/3.12149.

Meuer, H. W. (2008). "The TOP500 project: Looking back over 15 years of supercomputing experience." In: *Informatik-Spektrum* 31.3, pp. 203–222. DOI: 10.1007/s00287-008-0240-6.

Mink, A., Thäter, G., Nirschl, H., and Krause, M. J. (2016). "A 3D Lattice Boltzmann method for light simulation in participating media." In: *Journal of Computational Science* 17, pp. 431–437. DOI: 10.1016/j.jocs.2016.03.014.

Mohamad, A. A. (2011). *Lattice Boltzmann Method: Fundamentals and Engineering Applications with Computer Codes*. Vol. 51. 1. Springer London, pp. 278–279. DOI: 10.1007/978-0-85729-455-5.

Moureh, J., Tapsoba, M., and Flick, D. (2009a). "Airflow in a slot-ventilated enclosure partially filled with porous boxes: Part I - Measurements and simulations in the clear region." In: *Computers & Fluids* 38.2, pp. 194–205. DOI: 10.1016/j.compfluid.2008.02.006.

Moureh, J., Tapsoba, M., and Flick, D. (2009b). "Airflow in a slot-ventilated enclosure partially filled with porous boxes: Part II - Measurements and simulations within porous boxes." In: *Computers & Fluids* 38.2, pp. 206–220. DOI: 10.1016/j.compfluid.2008.02.007.

Mumtaz, M., Khan, A., Saidur, R., and Al-sulaiman, F. A. (2017). "A review for phase change materials (PCMs) in solar absorption refrigeration systems." In: *Renewable and Sustainable Energy Reviews* 76.February, pp. 105–137. DOI: 10.1016/j.rser.2017.03.070.

Nagel, W. E., Kröner, D., and Resch, M. M. (2018). *High Performance Computing in Science and Engineering '18*. Springer.

Nash, S. G. (1990). *A history of scientific English*. Vol. 34. 7. Accociation for Computing Machinery. DOI: 978-0-201-50814-7.

Nathen, P., Haussmann, M., Krause, M. J., and Adams, N. A. (2018). "Adaptive filtering for the simulation of turbulent flows with lattice Boltzmann methods." In: *Computers & Fluids* 172, pp. 510–523. DOI: 10.1016/j.compfluid.2018.03.042.

Nayamatullah, M. and Liu, X. (2013). "L Arge E Ddy S Imulations of S Uspended S Ediment T Ransport." In: April 2016.

Noble, D. R. and Torczynski, J. R. (1998). "A lattice-boltzmann method for partially saturated computational cells." In: *International Journal of Modern Physics C* 9.8, pp. 1189–1201. DOI: 10.1142/S0129183198001084.

Obrecht, C., Kuznik, F., Merlier, L., Roux, J.-J., and Tourancheau, B. (2015). "Towards aeraulic simulations at urban scale using the lattice Boltzmann method." In: *Environmental Fluid Mechanics* 15.4, pp. 753–770.

Oertel, H. (2017). *Prandtl – Führer durch die Strömungslehre*, pp. 119–186. DOI: 10.1007/978-3-658-08627-5_3.

Pan, C., Hilpert, M., and Miller, C. T. (2004). "Lattice-Boltzmann simulation of two-phase flow in porous media." In: *Water Resources Research* 40.1, pp. 1–14. DOI: 10.1029/2003WR002120.

Pasquali, A., Geier, M., and Krafczyk, M. (2020). "Near-wall treatment for the simulation of turbulent flow by the cumulant lattice Boltzmann method." In: *Computers & Mathematics with Applications* 79.1, pp. 195–212. DOI: 10.1016/j.camwa.2017.11.022.

Pellew, A. and Southwell, R. V. (1940). "On maintained convective motion in a fluid heated from below." In: *Proceedings of the Royal Society of London A: Mathematical, Physical and Engineering Sciences* 176.966, pp. 312–343. DOI: 10.1098/rspa.1940.0092.

Peng, Y., Shu, C., and Chew, Y. T. (2003). "Simplified thermal lattice Boltzmann model for incompressible thermal flows." In: *Physical Review E* 68.2, p. 026701. DOI: 10.1103/PhysRevE.68.026701.

Piomelli, U. (1998). "Large-eddy simulation: Present state and future perspectives." In: *36th AIAA Aerospace Sciences Meeting and Exhibit* 3. DOI: 10.2514/6.1998-534.

Pope, S. B. (2000). *Turbulent Flows*. Cambridge University Press. DOI: 10.1017/CBO9780511840531.

Premnath, K. N., Pattison, M. J., and Banerjee, S. (2009). "Dynamic subgrid scale modeling of turbulent flows using lattice-Boltzmann method." In: *Physica A: Statistical Mechanics and its Applications* 388.13, pp. 2640–2658. DOI: 10.1016/j.physa.2009.02.041.

Rayleigh, L. (1916). "On convection currents in a horizontal layer of fluid, when the higher temperature is on the under side." In: *Philosophical Magazine* 32.192, pp. 529–546. DOI: 10.1080/14786441608635602.

Rayleigh, L. (1917). "On the Dynamics of Revolving Fluids." In: *Proceedings of the Royal Society of London A: Mathematical, Physical and Engineering Sciences* 93.648, pp. 148–154. DOI: 10.1098/rspa.1917.0010.

Ren, Q., Meng, F., and Guo, P. (2018). "A comparative study of PCM melting process in a heat pipe-assisted LHTES unit enhanced with nanoparticles and metal foams by immersed boundary-lattice Boltzmann method at pore-scale." In: *International Journal of Heat and Mass Transfer* 121, pp. 1214–1228. DOI: 10.1016/j.ijheatmasstransfer.2018.01.046.

Rodi, W. (1993). *Turbulence models and their application in hydraulics*. 3rd. Routledge. DOI: 10.1016/0045-7825(81)90171-7.

Romanazzi, P. and Howey, D. A. (2015). "Air-gap convection in a switched reluctance machine." In: *2015 10th International Conference on Ecological Vehicles and Renewable Energies, EVER 2015*. DOI: 10.1109/EVER.2015.7112962.

Sagaut, P. (2010). "Toward advanced subgrid models for Lattice-Boltzmann-based Large-eddy simulation: Theoretical formulations." In: *Computers & Mathematics with Applications* 59.7, pp. 2194–2199. DOI: 10.1016/j.camwa.2009.08.051.

Sajjadi, H., Gorji, M., Hosseiniza Deh, S. F., Kefayati, G. R., and Ganji, D. D. (2011). "Numerical analysis of turbulent natural convection in square cavity using large-eddy simulation in lattice Boltzmann method." In: *Iranian Journal of Science and Technology, Transaction B: Engineering* 35.M2, pp. 133–142.

Salim, S. M. and Ong, K. C. (2013). "Performance of RANS, URANS and LES in the Prediction of Airflow and Pollutant Dispersion." In: *Lecture Notes in Electrical Engineering*. Vol. 170 LNEE, pp. 263–274. DOI: 10.1007/978-94-007-4786-9_21.

Sarbu, I. (2018). "A Comprehensive Review of Thermal Energy Storage." In: DOI: 10.3390/su10010191.

Sayadi, T. and Moin, P. (2012). "Large eddy simulation of controlled transition to turbulence." In: *Physics of Fluids* 24, p. 114103. DOI: 10.1063/1.4767537.

Schlichting, H. and Gersten, K. (2016). *Boundary-Layer Theory*. Vol. 3, pp. 1–799. DOI: 10.1007/978-3-662-52919-5.

Schlichting, H., Gersten, K., Krause, E., and Oertel, H. (1955). *Boundary-layer theory*. Vol. 7. Springer.

Schwarz, M. and Seidel, H. P. (2010). "Fast Parallel Surface and Solid Voxelization on GPUs." In: *ACM Transactions on Graphics* 29.6, pp. 1–10. DOI: 10.1145/1882261.1866201.

Shan, X. (1997). "Simulation of Rayleigh-Bénard convection using a lattice Boltzmann method." In: *Physical Review E - Statistical Physics, Plasmas, Fluids, and Related Interdisciplinary Topics* 55.3, pp. 2780–2788. DOI: 10.1103/PhysRevE.55.2780.

Shan, X., Yuan, X. F., and Chen, H. (2006). "Kinetic theory representation of hydrodynamics: A way beyond the Navier-Stokes equation." In: *Journal of Fluid Mechanics* 550, pp. 413–441. DOI: 10.1017/S0022112005008153.

Shang, B., Hu, J., Hu, R., Cheng, J., and Luo, X. (2018). "Modularized thermal storage unit of metal foam/paraffin composite." In: *International Journal of Heat and Mass Transfer* 125, pp. 596–603. DOI: 10.1016/j.ijheatmasstransfer.2018.04.117.

Shi, B. and Guo, Z. (2003). "Thermal Lattice Bgk Simulation of Turbulent Natural Convection Due To Internal Heat Generation." In: *International Journal of Modern Physics B* 17.2, pp. 173–177. DOI: 10.1142/S0217979203017291.

Silva, G. and Semiao, V. (2014). "Truncation errors and the rotational invariance of three-dimensional lattice models in the lattice Boltzmann method." In: *Journal of Computational Physics* 269, pp. 259–279. DOI: 10.1016/j.jcp.2014.03.027.

Silvis, M. H., Remmerswaal, R. A., and Verstappen, R. (2017). "Physical consistency of subgrid-scale models for large-eddy simulation of incompressible turbulent flows." In: *Physics of Fluids* 29.1. DOI: 10.1063/1.4974093.

Simmler, H. and Brunner, S. (2005). "Vacuum insulation panels for building application Basic properties , aging mechanisms and service life." In: 37, pp. 1122–1131. DOI: 10.1016/j.enbuild.2005.06.015.

Singh, H., Geisler, M., and Menzel, F. (2015). "Experimental investigations into thermal transport phenomena in vacuum insulation panels (VIPs) using fumed silica cores." In: *Energy and Buildings* 107, pp. 76–83. DOI: 10.1016/j.enbuild.2015.08.004.

Singh, R., Sadeghi, S., and Shabani, B. (2019). "Thermal conductivity enhancement of phase change materials for low-temperature thermal energy storage applications." In: *Energies* 12.1. DOI: 10.3390/en12010075.

Slotnick, J., Khodadoust, A., Alonso, J., and Darmofal, D. (2014). "CFD Vision 2030 Study: A Path to Revolutionary Computational Aerosciences." In: *Nnasa/Cr-2014-218178* March 2014.

Smagorinsky, J. (1963). "General Circulation Experiments With the Primitive Equations." In: *Monthly Weather Review* 91.3, pp. 99–164. DOI: 10.1175/1520-0493(1963)091<0099:gcewtp>2.3.co;2.

Smale, N. J., Moureh, J., and Cortella, G. (2006). "A review of numerical models of airflow in refrigerated food applications." In: *International Journal of Refrigeration* 29, pp. 911–930. DOI: 10.1016/j.ijrefrig.2006.03.019.

Solomon, A. (1966). "Some Remarks on the Stefan Problem." In: *Mathematics of Computation* 20.95, p. 347. DOI: 10.2307/2003588.

Sonnick, S., Meier, M., Ross-Jones, J., Erlbeck, L., Medina, I., Nirschl, H., and Rädle, M. (2019). "Correlation of pore size distribution with thermal conductivity of precipitated silica and experimental determination of the coupling effect." In: *Applied Thermal Engineering* 150.January, pp. 1037–1045. DOI: 10.1016/j.applthermaleng.2019.01.074.

Spoletini, E. (2016). "Economic analysis and technical issues of low temperature PCM thermal storage combined with a condensing micro-CHP." In: *Energy Procedia* 101.September, pp. 1151–1158. DOI: 10.1016/j.egypro.2016.11.156.

Stephan, P., Schaber, K., Stephan, K., and Mayinger, F. (2013). *Thermodynamik*. DOI: 10.1007/978-3-642-30098-1.

Stolz, S. and Adams, N. A. (1999). "An approximate deconvolution procedure for large-eddy simulation." In: *Physics of Fluids* 11.7, pp. 1699–1701. DOI: 10.1063/1.869867.

Succi, S. (2001a). *The Lattice Boltzmann Equation – for Fluid Dynamics and Beyond*. 1st ed. Oxford University Press.

Succi, S. (2001b). *The Lattice Boltzmann Equation: For Fluid Dynamics and Beyond*. Oxford University Press, p. 288. DOI: ISBN0198503989.

Succi, S., Amati, G., and Benzi, R. (1995). "Challenges in lattice Boltzmann computing." In: *Journal of Statistical Physics* 81.1-2, pp. 5–16. DOI: 10.1007/BF02179964.

Tang, G. H., Tao, W. Q., and He, Y. L. (2005). "Lattice Boltzmann method for gaseous microflows using kinetic theory boundary conditions." In: *Physics of Fluids* 17.5, pp. 1–4. DOI: 10.1063/1.1897010.

Tapsoba, M., Moureh, J., and Flick, D. (2007). "Airflow patterns in a slot-ventilated enclosure partially loaded with empty slotted boxes." In: *International Journal of Heat and Fluid Flow* 28.5, pp. 963–977. DOI: https://doi.org/10.1016/j.ijheatfluidflow.2007.03.008.

Tassou, S. A., De-Lille, G., and Ge, Y. T. (2009). "Food transport refrigeration - Approaches to reduce energy consumption and environmental impacts of road transport." In: *Applied Thermal Engineering* 29.8-9, pp. 1467–1477. DOI: 10.1016/j.applthermaleng.2008.06.027.

Taylor, G. I. (1923). "Stability of a Viscous Liquid Contained between Two Rotating Cylinders." In: *Philosophical Transactions Royal Society of London* Vol. 223.No. 605-615, pp. 289–343. DOI: doi:10.1098/rsta.1923.0008.

Taylor, G. I. (1936). "Fluid Friction between Rotating Cylinders. I. Torque Measurements." In: *Proceedings of the Royal Society of London A: Mathematical,*

Physical and Engineering Sciences 157.892, pp. 546–564. DOI: 10.1098/rspa.1936.0215.

Teixeira, C. M. (1998). "Incorporating Turbulence Models into the Lattice-Boltzmann Method." In: *International Journal of Modern Physics C* 09.08, pp. 1159–1175. DOI: 10.1142/S0129183198001060.

Thapa, S., Chukwu, S., Khaliq, A., and Weiss, L. (2014). "Fabrication and analysis of small-scale thermal energy storage with conductivity enhancement." In: *Energy Conversion and Management* 79, pp. 161–170. DOI: 10.1016/j.enconman.2013.12.019.

Thürey, N. and Rüde, U. (2004). "Free Surface Lattice-Boltzmann fluid simulations with and without level sets." In: *Vision, Modeling and Visualization 2004, VMV 2004 - Proceedings*, pp. 199–207.

Tiftikci, A. and Kocar, C. (2016). "Investigation of Thermal Turbulent Flow Characteristics of Wire-wrapped Fuel Pin Bundle of Sodium Cooled Fast Reactor in Lattice-Boltzmann Framework." In: *25th International Conference Nuclear Energy for New Europe (NENE)*.

Treeck, C. van, Rank, E., Krafczyk, M., Tölke, J., and Nachtwey, B. (2006). "Extension of a hybrid thermal LBE scheme for large-eddy simulations of turbulent convective flows." In: *Computers & Fluids* 35.8-9, pp. 863–871. DOI: 10.1016/j.compfluid.2005.03.006.

Trunk, R., Henn, T., Dörfler, W., Nirschl, H., and Krause, M. J. (2016). "Inertial dilute particulate fluid flow simulations with an Euler–Euler lattice Boltzmann method." In: *Journal of Computational Science* 17, pp. 438–445. DOI: 10.1016/j.jocs.2016.03.013.

Tso, C. P., Yu, S. C. M., Poh, H. J., and Jolly, P. G. (2002). "Experimental study on the heat and mass transfer characteristics in a refrigerated truck." In: *International Journal of Refrigeration* 25.3, pp. 340–350. DOI: 10.1016/S0140-7007(01)00015-9.

Tsugé, S. and Sagara, K. (1976). "Kinetic theory of turbulent compressible flows and comparison with classical theory." In: *Physics of Fluids* 19.10, pp. 1478–1485. DOI: 10.1063/1.861350.

Van der Zwaan, B., Keppo, I., and Johnsson, F. (2013). "How to decarbonize the transport sector?" In: *Energy Policy* 61, pp. 562–573. DOI: 10.1016/j.enpol.2013.05.118.

VDI-Gesellschaft (2013). *VDI-Wärmeatlas*. 11., bearb. Springer Vieweg, p. 1512.

Verma, P., Varun, and Singal, S. K. (2008). "Review of mathematical modeling on latent heat thermal energy storage systems using phase-change mate-

rial." In: *Renewable and Sustainable Energy Reviews* 12.4, pp. 999–1031. DOI: 10.1016/j.rser.2006.11.002.

Wakili, K. G., Bundi, R., and Binder, B. (2004). "Effective thermal conductivity of vacuum insulation panels." In: *Building Research & Information* 32.4, pp. 293–299. DOI: 10.1080/0961321042000189644.

Wang, J., Wang, M., and Li, Z. (2007). "A lattice Boltzmann algorithm for fluid–solid conjugate heat transfer." In: *International Journal of Thermal Sciences* 46.3, pp. 228–234. DOI: 10.1016/j.ijthermalsci.2006.04.012.

Wang, M., Kang, Q., and Pan, N. (2009). "Thermal conductivity enhancement of carbon fiber composites." In: *Applied Thermal Engineering* 29.2-3, pp. 418–421. DOI: 10.1016/j.applthermaleng.2008.03.004.

Wang, M. and Pan, N. (2008). "Modeling and prediction of the effective thermal conductivity of random open-cell porous foams." In: *International Journal of Heat and Mass Transfer* 51.5-6, pp. 1325–1331. DOI: 10.1016/j.ijheatmasstransfer.2007.11.031.

Wegger, E., Jelle, B. P., Sveipe, E., Grynning, S., Gustavsen, A., Baetens, R., and Thue, J. V. (2011). "Aging effects on thermal properties and service life of vacuum insulation panels." In: *Journal of Building Physics* 35.2, pp. 128–167. DOI: 10.1177/1744259111398635.

Weickert, M., Teike, G., Schmidt, O., and Sommerfeld, M. (2010). "Investigation of the LES WALE turbulence model within the lattice Boltzmann framework." In: *Computers & Mathematics with Applications* 59.7, pp. 2200–2214. DOI: 10.1016/j.camwa.2009.08.060.

White, F. M. (2003). "Fluid Mechanics." In: *Boston: McGraw-Hill Book Company*, p. 467.

Willems, W. and Skottke, T. (2008). "Lineare Wärmebrücken in vakuumgedämmten Konstruktionen." In: *Bauphysik* 30.6, pp. 373–379. DOI: 10.1002/bapi.200810048.

Wittig, K. and Nikrityuk, P. A. (2011). "Three-dimensionality of fluid flow in the benchmark experiment for a pure metal melting on a vertical wall." In: *IOP Conference Series: Materials Science and Engineering* 27.1. DOI: 10.1088/1757-899X/27/1/012054.

Wolf-Gladrow, D. a. (2000). *Lattice-Gas Cellular Automata and Lattice Boltzmann Models - An Introduction*. 1725. Springer Science & Business Media, p. 308. DOI: 978-3-540-66973-9.

Wu, H., Wang, J., and Tao, Z. (2011). "Passive heat transfer in a turbulent channel flow simulation using large eddy simulation based on the lattice Boltz-

mann method framework." In: *International Journal of Heat and Fluid Flow* 32.6, pp. 1111–1119. DOI: 10.1016/j.ijheatfluidflow.2011.09.001.

Xian, W. and Takayuki, A. (2011). "Multi-GPU performance of incompressible flow computation by lattice Boltzmann method on GPU cluster." In: *Parallel Computing* 37.9, pp. 521–535. DOI: 10.1016/j.parco.2011.02.007.

Xiao, X., Zhang, P., and Li, M. (2014). "Effective thermal conductivity of open-cell metal foams impregnated with pure paraffin for latent heat storage." In: *International Journal of Thermal Sciences* 81.1, pp. 94–105. DOI: 10.1016/j.ijthermalsci.2014.03.006.

Xu, A., Shi, L., and Zhao, T. S. (2017). "Accelerated lattice Boltzmann simulation using GPU and OpenACC with data management." In: *International Journal of Heat and Mass Transfer* 109, pp. 577–588. DOI: 10.1016/j.ijheatmasstransfer.2017.02.032.

Xu, Y., Li, M. J., Zheng, Z. J., and Xue, X. D. (2018). "Melting performance enhancement of phase change material by a limited amount of metal foam: Configurational optimization and economic assessment." In: *Applied Energy* 212.October 2017, pp. 868–880. DOI: 10.1016/j.apenergy.2017.12.082.

Yang, B., Raza, A., Bai, F., Zhang, T., and Wang, Z. (2019). "Microstructural evolution within mushy zone during paraffin's melting and solidification." In: *International Journal of Heat and Mass Transfer* 141, pp. 769–778. DOI: 10.1016/j.ijheatmasstransfer.2019.07.019.

Yang, X., Yu, J., Guo, Z., Jin, L., and He, Y.-l. (2019). "Role of porous metal foam on the heat transfer enhancement for a thermal energy storage tube." In: *Applied Energy* 239.October 2018, pp. 142–156. DOI: 10.1016/j.apenergy.2019.01.075.

Yoshida, H. and Nagaoka, M. (2010). "Multiple-relaxation-time lattice Boltzmann model for the convection and anisotropic diffusion equation." In: *Journal of Computational Physics* 229.20, pp. 7774–7795.

Yuan, X., Rösler, M., Gritzki, R., and Felsmann, C. (2017). "Lattice-Boltzmann-Methoden zur Berechnung von Raumluftströmungen." In: *GI - Gebäudetechnik in Wissenschaft & Praxis* 138.03, pp. 256–262.

Zalba, B., Marín, J. M., Cabeza, L. F., and Mehling, H. (2003). "Review on thermal energy storage with phase change: materials, heat transfer analysis and applications." In: *Applied Thermal Engineering* 23.3, pp. 251–283. DOI: https://doi.org/10.1016/S1359-4311(02)00192-8.

Zhao, C. Y. (2012). "Review on thermal transport in high porosity cellular metal foams with open cells." In: *International Journal of Heat and Mass Transfer* 55.13-14, pp. 3618–3632. DOI: 10.1016/j.ijheatmasstransfer.2012.03.017.

Zheng, L., Shi, B., Guo, Z., and Zheng, C. (2010). "Lattice Boltzmann equation for axisymmetric thermal flows." In: *Computers & Fluids* 39.6, pp. 945–952. DOI: 10.1016/j.compfluid.2010.01.006.

Zhou, Y., Zhang, R., Staroselsky, I., and Chen, H. (2004). "Numerical simulation of laminar and turbulent buoyancy-driven flows using a lattice Boltzmann based algorithm." In: *International Journal of Heat and Mass Transfer* 47.22, pp. 4869–4879. DOI: 10.1016/j.ijheatmasstransfer.2004.05.020.

Zhu, W., Wang, M., and Chen, H. (2017). "2D and 3D lattice Boltzmann simulation for natural convection melting." In: *International Journal of Thermal Sciences* 117, pp. 239–250. DOI: 10.1016/j.ijthermalsci.2017.03.025.

Appendix

A List of Figures

B List of Tables

C Verification of the Contribution From the Co-Authors

Chapter 3

Title Application of a Lattice Boltzmann Method combined with a Smagorinsky Turbulence Model to Spatially Resolved Heat Flux inside a Refrigerated Vehicle

Journal Computers & Mathematics with Applications (76), 2018

Authors Maximilian Gaedtke, Simon Wachter, Matthias Rädle, Hermann Nirschl, Mathias J. Krause

Position The content of this paper has been included in Chapter 3.

Contributions (following the contributor roles taxonomy (Brand et al. 2015))

Maximilian Gaedtke Conceptualization, methodology, software, validation, formal analysis, investigation, data curation, writing – original draft, visualization, project administration

Simon Wachter Software, validation, data curation, writing - review & editing

Matthias Rädle Project administration, funding acquisition

Hermann Nirschl Resources, supervision

Mathias J. Krause Resources, software, supervision, writing - review & editing, project administration, funding acquisition

Chapter 4

Title Flow and Heat Transfer Simulation with a Thermal Large Eddy Lattice Boltzmann Method in an Annular Gap with an Inner Rotating Cylinder

Journal International Journal of Modern Physics C (30), 2019

Authors Maximilian Gaedtke, Tabitha Hoffmann, Volkmar Reinhardt, Gudrun Thäter, Hermann Nirschl, Mathias J. Krause

Position The content of this paper has been included in Chapter 4.

Contributions (following the contributor roles taxonomy (Brand et al. 2015))

Maximilian Gaedtke Conceptualization, methodology, software, validation, investigation, data curation, writing – original draft, visualization

Tabitha Hoffmann Software, validation, data curation, writing - review & editing

Volkmar Reinhardt Resources, supervision, project administration

Gudrun Thäter Supervision, project administration

Hermann Nirschl Resources, supervision

Mathias J. Krause Resources, software, supervision, writing - review & editing

Chapter 5

Title Numerical Study on the Application of Vacuum Insulation Panels and a Latent Heat Storage for Refrigerated Vehicles with a Large Eddy Lattice Boltzmann Method

Journal Heat and Mass Transfer (56), 2020

Authors Maximilian Gaedtke, Simon Wachter, Sven Kunkel, Sebastian Sonnick, Matthias Radle, Hermann Nirschl, Mathias J. Krause

Position The content of this paper has been included in Chapter 5.

Contributions (following the contributor roles taxonomy (Brand et al. 2015))

Maximilian Gaedtke Conceptualization, methodology, software, validation, formal analysis, investigation, data curation, writing – original draft, visualization, project administration, funding acquisition

Simon Wachter Software, validation, data curation, writing - review & editing

Sven Kunkel Resources

Sebastian Sonnick Resources

Matthias Rädle Project administration, funding acquisition

Hermann Nirschl Resources, supervision

Mathias J. Krause Resources, software, supervision, writing - review & editing, project administration, funding acquisition

Chapter 6

Title Total Enthalpy-Based Lattice Boltzmann Simulations of Melting in Paraffin/Metal Foam Composite Phase Change Materials

Journal International Journal of Heat and Mass Transfer (155), 2020

Authors Maximilian Gaedtke, S. Abishek, Ryan Mead-Hunter, Andrew J. C. King, Benjamin J. Mullins, Hermann Nirschl, Mathias J. Krause

Position The content of this paper has been included in Chapter 6.

Contributions (following the contributor roles taxonomy (Brand et al. 2015))

Maximilian Gaedtke conceptualization, methodology, software, validation, investigation, writing – original draft, visualization, funding acquisition

S. Abishek Resources, data curation, writing - review & editing

Ryan Mead-Hunter Writing - review & editing

Andrew J. C. King Resources

Benjamin J. Mullins Conceptualization, writing - review & editing, resources, supervision, project administration, funding acquisition

Hermann Nirschl Supervision

Mathias J. Krause Conceptualization, software, supervision, funding acquisition

D List of Application Cases

The following commit hashes refer to the master branch of the repository hosted at gitlab.com/openlb/olb. Supplemental material, such as geometries given by STL files, is attached on CD.

1. Porous plate problem 2D

   Description: see Section 3.3.1.1
   Commit hash: `3ea8d1b5f`
   Case folder: `examples/thermal/porousPlate2d`
   Released since: Version 1.2

2. Porous plate problem 3D

   Description: see Section 3.3.1.1
   Commit hash: `3ea8d1b5f`
   Case folder: `examples/thermal/porousPlate3d`
   Released since: Version 1.2

3. Natural convection in a square cavity 2D

   Description: see Section 3.3.1.2
   Commit hash: `3ea8d1b5f`
   Case folder: `examples/thermal/squareCavity2d`
   Released since: Version 1.2

4. Natural convection in a square cavity 3D

   Description: see Section 3.3.1.2
   Commit hash: `3ea8d1b5f`
   Case folder: `examples/thermal/squareCavity3d`
   Released since: Version 1.2

5. Refrigerated truck: open door measurement set-up 3D

   Description: see Section 3.3.2.1
   Commit hash: `269ef5ef6, e3e6932e9`
   Case folder: `apps/max/thermal3dTestISO,`
   `apps/max/thermal3dTestOhneVIP,`
   `apps/max/thermal3dValidierung`

6. Taylor-Couette flow 3D

Description: see Section 4.3.5
Commit hash: `269ef5ef6, e3e6932e9`
Case folder: `apps/max/concenctricCylinders`

7. Refrigerated truck: VIP insulation 3D

   Description: see Section 5.3
   Commit hash: `d55693a07`
   Case folder: `apps/max/thermal3dtestVIP, apps/max/thermal3dMitVIP`

8. Refrigerated truck: leakage at rear door 3D

   Description: see Section 5.3
   Commit hash: `269ef5ef6, e3e6932e9`
   Case folder: `apps/max/thermal3dMitLeckage`

9. Refrigerated truck: LHS integration 3D

   Description: see Section 5.3
   Commit hash: `269ef5ef6, e3e6932e9`
   Case folder: `apps/max/thermal3dMitPCM`

10. Refrigerated truck: cargo temperature 3D

    Description: see Section 5.3
    Commit hash: `269ef5ef6, e3e6932e9`
    Case folder: `apps/max/thermal3dMitLadung, apps/max/thermal3dMitLadungUndVIP`

11. Stefan problem 2D

    Description: see Section 6.3.1
    Commit hash: `4d1b0d025`
    Case folder: `examples/thermal/stefanMelting2d`
    Released since: Version 1.4

12. Stefan problem 3D

    Description: see Section 6.3.1
    Commit hash: `6205e26f5`
    Case folder: `apps/max/totalEnthalpy1dMeltingHuang3d`

13. Melting of gallium 2D

    Description: see Section 6.3.2

Commit hash: `4d1b0d025`
Case folder: `examples/thermal/galliumMelting2d`
Released since: Version 1.4

14. Melting of gallium 3D

    Description: see Section 6.3.2
    Commit hash: `cad891a8b`
    Case folder: `apps/max/totalEnthalpy2dMelting3dGallium`

15. Melting of paraffin in metal foam 3D

    Description: see Section 6.4.1
    Commit hash: `053dd8ab7`
    Case folder: `apps/max/totalEnthalpyMelting3dFoam`